

Severin Huemer-Kals, BSc.

## **Complex Eigenvalue Analysis of Friction Induced Low-Frequency Vibrations in Vehicle Disc Brake Systems**

Linearized, Quasi-Static Simulation for Creep Groan and Moan?

Master thesis

Aspired academic degree: Diplom-Ingenieur / Master of Science

Master's programme: Mechanical Engineering

Graz University of Technology

Faculty of Mechanical Engineering and Economic Sciences

Institute of Automotive Engineering

Member of Frank Stronach Institute

Head of Institute: Univ.-Prof. Dipl.-Ing. Dr.techn. Peter Fischer

Supervising tutor: Dipl.-Ing. Manuel Pürscher, BSc.

Graz, 29<sup>th</sup> May 2018



---

# Acknowledgement

First and foremost, I would like to thank my supervisor, colleague and dear friend Dipl.-Ing. Manuel Pürscher for his dedicated support during the work on this thesis. In addition to all the highly professional advice, his constant encouragement, motivation and his untroubled mind influenced me and the outcome of this work in the most positive way.

Another thank you has to be said to my colleagues at the FTG, especially towards my predecessor Dipl.-Ing. Andreas Sattlecker. His work significantly simplified the beginning of my own activities on the issues presented here.

Furthermore, I would like to thank Univ.-Prof. Dipl.-Ing. Dr.techn. Peter Fischer one more time. Ten years of support, trust and common work are of exceptional value for me and my professional career. Thank you for all these great possibilities, discussions and projects.

As this master thesis is only the cherry on top of the whole thing, I would also like to use some lines to thank my fellow students. I doubt that anyone could undergo such a challenging education without the support and help of one's friends – at least it would not be much fun. I would like to explicitly thank my apartment colleagues: for all the great times, bad jokes, for the long nights we were working and the long nights we were not working.

One more huge thank you should be said to my family. Despite all the difficulties, I can always count on them and their encouragement. My mother Elfriede, my father Karl as well as my sisters Veronika and Kornelia usually believe more in me than I do myself. Thank you for all your great support!

Finally, I am quite sure that I have not only developed in terms of technical and engineering skills throughout this master's program. Definitely, life taught me lessons in almost any subject during these 6 years and I am very grateful that I was always able to share whatever came along my path. As this should still stay a one-pager, I don't want to mention anyone explicitly, you will probably know if you are meant: Thank you for listening, thinking, talking, understanding, laughing, dancing, singing, climbing mountains, helping, discussing and, most of it all, being.



---

# Statutory Declaration

Ich erkläre an Eides statt, dass ich die vorliegende Arbeit selbstständig verfasst, andere als die angegebenen Quellen/Hilfsmittel nicht benutzt, und die den benutzten Quellen wörtlich und inhaltlich entnommenen Stellen als solche kenntlich gemacht habe.

Graz, am .....  
(Unterschrift)

I declare that I have authored this thesis independently, that I have not used other than the declared sources / resources, and that I have explicitly marked all material which has been quoted either literally or by content from the used sources.

.....  
(date) (signature)



---

# Abstract

Demands regarding the NVH (Noise, Vibration, Harshness) behavior of vehicles have recently seen a major increase. Often, expensive warranty claims result for automotive OEMs (Original Equipment Manufacturers). Therefore, vibro-acoustic phenomena of vehicle disk brake systems such as brake squeal, moan or creep groan have experienced a rise in interest over the last few years. Due to rather complex relationships leading to these non-linear, friction-induced oscillation phenomena, an engineer's options are often limited to corrective actions based on prototype tests of the complete vehicle or reduced physical models.

Simulations can be the tool of choice for early development stages as they lead to better understanding of the causes and effects, enabling effective reduction of occurring sound and vibration. The simulation tool Complex Eigenvalue Analysis (CEA) is broadly used in industrial brake squeal applications. One big advantage of this linearized, quasi-static approach is its efficient computation procedure: Huge parameter ranges can be computed rather fast, even for full axle and brake models. As the demand for suitable simulation tools for low-frequency phenomena rises, the application of Complex Eigenvalue Analysis for the prediction of creep groan or moan would be appealing. Therefore, this possibility is analyzed in this work.

After an introduction about disk brake systems, elastomer bushings and non-linear oscillations, phenomenological descriptions of creep groan, moan and squeal are reviewed in a short manner. Different explanation models and possible causes are presented. In the following, the theoretical and mathematical foundation of the CEA is analyzed. Based on this, application limits are stated: Computation of moan oscillations should be possible, whereas the prediction of creep groan oscillations cannot be covered by this procedure in the context of stick-slip oscillations.

Subsequently, a Finite Element model of a full vehicle's front corner with double wishbone suspension and fixed caliper brake is evaluated. A breakdown of the system matrices' structure and relevance is done. In the following, a classical brake squeal CEA procedure is applied on several different variants with changes of elastomer bushings' stiffness and damping, rotational influences and rim design.

The resulting relevant modes reveal detailed information about the displacement and frequency content of creep groan and moan oscillations. Obtained results underline the importance of modeling parameters such as non-linear bushing stiffness and damping. A validation of the simulative outcome based on corresponding experimental tests and literature findings leads to a general recommendation for upcoming transient and quasi-static simulations.



---

# Kurzfassung

Die Anforderungen der Kunden an das Verhalten von Fahrzeugen in Bezug auf Geräusch- und Vibrationskomfort sind in den vergangenen Jahren wesentlich gestiegen und führen immer wieder zu teuren Gewährleistungsfällen für die Autohersteller. Aus diesem Grund rücken vibro-akustische Phänomene an Scheibenbremsen wie z.B. Quietschen, Muhen oder Knarzen stärker in den Fokus. Aufgrund der komplexen Zusammenhänge, die zu diesen nichtlinearen, reiberregten Schwingungen führen, ist Abhilfe hierbei oft auf korrigierende Maßnahmen basierend auf Prototypentests des Gesamtfahrzeuges oder reduzierter physikalischer Modelle beschränkt.

Simulationen können hier bereits in der frühen Entwicklungsphase zum Verständnis der physikalischen Ursachen und zur besseren Behandelbarkeit führen. Derzeit existiert mit der komplexen Eigenwertanalyse (KEA) ein Simulationswerkzeug, welches in der Prädiktion von höherfrequentem Bremsenquietschen industrielle Anwendung findet. Ein großer Vorteil dieser linearen, quasi-statischen Methode ist die effiziente Berechnung, selbst von umfassenden Viertelfahrzeugmodellen. Mit zunehmendem Fokus auf niederfrequente Phänomene wächst auch hier der Bedarf an Werkzeugen: Diese Arbeit untersucht die Anwendung der KEA für Knarzen und Muhen.

Nach einem kurzen Überblick über Scheibenbremssysteme, Fahrwerkslager und nichtlineare Schwingungen wird dazu zunächst das Systemverhalten von Knarzen, Muhen und Quietschen erörtert. Verschiedene Erklärungsmodelle und mögliche Ursachen werden diskutiert, es folgt eine Analyse der mathematischen Grundlagen. Daraufhin werden Grenzen der Anwendung aufgezeigt: Während die Prädiktion von Muhen als möglich eingestuft wird, ergeben sich für die charakteristischen Haft-Gleit-Schwingungen bei Knarzen deutliche Einschränkungen.

In weiterer Folge wird ein Finite Elemente Modell eines Viertelfahrzeuges mit Festsattelbremse und Doppelquerlenkeraufhängung analysiert. Nach einer Evaluierung von Struktur und Einfluss der Systemmatrizen wird die klassische Vorgehensweise bzgl. Quietschen für niederfrequente Schwingungen an mehreren Modellvarianten durchgeführt. Insbesondere die Einflüsse von Elastomerlagern, verschiedenen Felgengedesigns oder rotatorischen Termen können somit ermittelt werden.

Resultierende instabile und relevante Moden zeigen deutlich die wesentlichen Verschiebungen und Frequenzinhalte von Knarz- und Muhschwingungen auf. Des Weiteren wurden die hohen Einflüsse von Modellparametern, wie z.B. (nicht-linearer) Steifigkeit und Dämpfung der Fahrwerkslager, dargelegt. Eine Validierung, unter anderem anhand von zugehörigen Prüfstandsversuchen, führt schließlich zu Empfehlungen für weiterführende transiente oder auch quasi-statische Simulationen.



# Contents

<b>Abbreviations</b>	<b>xi</b>
<b>Symbols</b>	<b>xiii</b>
<b>1 Introduction</b>	<b>1</b>
1.1 Motivation . . . . .	1
1.2 Scientific Approach and Structure . . . . .	2
<b>2 State of the Art</b>	<b>3</b>
2.1 Passenger Vehicle Brake Systems . . . . .	3
2.1.1 Basic Requirements . . . . .	3
2.1.2 Structure of a Conventional Passenger Vehicle Disk Brake System . . . . .	4
2.1.2.1 Brake Disk . . . . .	7
2.1.2.2 Brake Caliper . . . . .	8
2.1.2.3 Brake Pads . . . . .	9
2.1.3 Current Trends and Future Concepts . . . . .	10
2.2 Elastomer Bushings . . . . .	12
2.2.1 Joint Function of Elastomer Bushings . . . . .	13
2.2.2 Oscillation Reduction via Elastomer Bushings . . . . .	13
2.2.2.1 Oscillation Damping and Dynamic Stiffness Behavior . . . . .	13
2.2.2.2 Oscillation Isolation . . . . .	14
2.2.3 Elastokinematic Behavior . . . . .	16
2.2.3.1 Elastokinematic Behavior for Vertical Load Changes . . . . .	17
2.2.3.2 Elastokinematic Behavior for Lateral Load Changes . . . . .	17
2.2.3.3 Elastokinematic Behavior for Longitudinal Load Changes . . . . .	18
2.2.3.4 Practical Approach for Elastokinematic Design . . . . .	19
2.2.4 Design Examples . . . . .	20
2.3 Nonlinear Oscillation Phenomena . . . . .	21
2.3.1 Super- and Subharmonics . . . . .	22
2.3.2 Limit Cycles . . . . .	25
2.3.3 Bifurcations . . . . .	26
2.3.4 Hartman–Grobman Theorem and Linearized Stability Analysis . . . . .	28
2.4 Disk Brake Noise, Vibration and Harshness . . . . .	29
2.4.1 Phenomenology . . . . .	29
2.4.1.1 Creep Groan . . . . .	30
2.4.1.2 Moan . . . . .	32
2.4.1.3 Squeal . . . . .	33
2.4.2 Explanation Models . . . . .	34
2.5 Complex Eigenvalue Analysis for Disk Brake Squeal . . . . .	35
2.5.1 Step 1: Static, Non-Linear Contact Analysis . . . . .	37
2.5.2 Step 2: Linear Static Analysis . . . . .	39
2.5.3 Step 3: Real Eigenvalue Analysis . . . . .	40

2.5.4	Step 4: Complex Eigenvalue Analysis . . . . .	42
2.5.5	Application Limits of CEA . . . . .	43
<b>3</b>	<b>Methodology</b>	<b>45</b>
3.1	CEA Application on a Full-Scale Corner Model . . . . .	45
3.1.1	Model Variants and Parameters . . . . .	45
3.1.2	Elastomer Bushing Behavior . . . . .	49
3.1.2.1	Elastomer Bushing Stiffness Modeling . . . . .	50
3.1.2.2	Elastomer Bushing Damping Modeling . . . . .	54
3.1.3	Simulation Procedure . . . . .	60
3.2	Investigation of the CEA System Matrices . . . . .	61
<b>4</b>	<b>Results</b>	<b>67</b>
4.1	Displacement Results . . . . .	67
4.1.1	Unstable Mode #1 . . . . .	67
4.1.2	Unstable Mode #2 . . . . .	69
4.1.3	Unstable Mode #3 . . . . .	69
4.1.4	Unstable Mode #4 . . . . .	70
4.1.5	Unstable Mode #5 . . . . .	72
4.1.6	Unstable Mode #6 . . . . .	72
4.1.7	Relevant Mode #7 . . . . .	72
4.2	Stability and Eigenfrequency Results . . . . .	76
4.2.1	Unstable Mode #1 . . . . .	77
4.2.2	Unstable Mode #3 . . . . .	80
4.2.3	Unstable Mode #4 . . . . .	82
4.2.4	Unstable Mode #6 . . . . .	85
4.2.5	Relevant Mode #7 . . . . .	86
<b>5</b>	<b>Validation and Discussion</b>	<b>89</b>
5.1	Phenomenological Validation . . . . .	89
5.1.1	Creep Groan Related Unstable Modes . . . . .	89
5.1.1.1	Unstable Mode #1 . . . . .	91
5.1.1.2	Unstable Mode #3 . . . . .	91
5.1.1.3	Unstable Mode #4 . . . . .	94
5.1.2	Moan Related Unstable and Relevant Modes . . . . .	94
5.1.2.1	Unstable Mode #6 . . . . .	94
5.1.2.2	Relevant Mode #7 . . . . .	95
5.2	Discussion of the Results . . . . .	96
5.2.1	Creep Groan Related Unstable Modes . . . . .	96
5.2.2	Moan Related Unstable and Relevant Modes . . . . .	98
5.3	Shortcomings and Further Potential of the Method . . . . .	99
5.4	Recommendations for Transient Creep Groan Simulation . . . . .	100
<b>6</b>	<b>Conclusions</b>	<b>103</b>
	<b>List of Figures</b>	<b>I</b>
	<b>List of Tables</b>	<b>V</b>
	<b>Bibliography</b>	<b>VII</b>

## Abbreviations

ABS	Antilock Brake System
AMS	Aluminum Matrix Compound
ACC	Adaptive Cruise Control
CEA	Complex Eigenvalue Analysis
CMS	Component Mode Synthesis
DOF	Degree Of Freedom
EPB	Electric Parking Brake
ESC	Electronic Stability Control
FE	Finite Element
FFT	Fast Fourier Transformation
HECU	Hydraulic-Electronic Control Unit
HMI	Human Machine Interface
ISO	International Organization for Standardization
KEA	Komplexe Eigenwertanalyse
MPC	Multi-Point Constraint
NAO	Non Asbestos Organics
NVH	Noise, Vibration and Harshness
ODE	Ordinary Differential Equation
OEM	Original Equipment Manufacturer
POD	Proper Orthogonal Decomposition
PSD	Power Spectral Density
REA	Real Eigenvalue Analysis
TCS	Traction Control System

---

var.	variant
Squeal-M.	Squeal-Model
Corr. Geom.	Corrected Geometry
Non-lin. Stiff.	Non-linear Stiffness
Best-M.	Best-Model
Best-M. LD	Best-Model Low Damping
Best-M. no ROT	Best-Model no Rotational Matrices
Best-M. Moan-A	Best-Model Moan rim A
Best-M. Moan-B	Best-Model Moan rim B



# Symbols

## Matrices

$\Phi$	modal matrix
$A$	system matrix
$\tilde{D}$	sum of modal damping matrices
$D_{Ct}, \tilde{D}_{Ct}$	damping matrix due to Coulomb friction, modal damping matrix due to Coulomb friction
$\tilde{D}_{eqv}$	modal equivalent viscous damping matrix
$D_G, \tilde{D}_G$	gyroscopic matrix, modal gyroscopic matrix
$D_V, \tilde{D}_V$	viscous damping matrix, modal viscous damping matrix
$H, \tilde{H}$	structural damping matrix, modal structural damping matrix
$I$	unit matrix
$J$	Jacobian matrix
$\tilde{K}$	sum of modal stiffness matrices
$K_C, \tilde{K}_C$	convective stiffness matrix, modal convective stiffness matrix
$K_{Ct}, \tilde{K}_{Ct}$	asymmetric stiffness matrix due to friction terms, modal asymmetric stiffness matrix due to friction terms
$K_{el}, \tilde{K}_{el}$	elastic stiffness matrix, modal elastic stiffness matrix
$K_G, \tilde{K}_G$	geometric stiffness matrix, modal geometric stiffness
$M, \tilde{M}$	mass matrix, modal mass matrix

## Parameters and Variables

$\alpha$	angular dimension
$\beta$	phase lag of the excitation force slip angle

$\gamma$	phase lag between excitation force and displacement / loss angle
$\delta$	real part of eigenvalue
$\delta_{i,j}$	elastokinematic steering angle
$\varepsilon$	Van der Pol parameter
$\eta$	frequency ratio
$\theta$	angular displacement
$\dot{\theta}$	angular speed
$\kappa$	Hopf parameter
$\mu$	coefficient of sliding friction
$\mu_0$	coefficient of sticking friction
$\xi_i$	equivalent viscous damping ratio
$\Psi$	phase lag of displacements
$\omega$	rotational eigenfrequency – imaginary part of eigenvalue rotational frequency
$\omega_0$	undamped eigenfrequency
$\omega_{\text{real}}$	rotational eigenfrequency of real modes
$\Omega_i$	rotational speed of wheel and brake disk / excitation rotational frequency
$\Omega_{\text{ref}}$	reference rotational speed
$c$	static, elastic stiffness
$c_1, c_2, \dots$	static stiffnesses of spring elements in local element coordinates
$\bar{c}_{(4),(5)}$	parameter-dependent axial bushing stiffnesses (4), (5)
$\bar{c}_{\text{lin},(4),(5)}$	linear part of parameter-dependent bushing stiffnesses (4), (5)
$\bar{c}_{\text{nonlin},(4),(5)}$	non-linear part of parameter-dependent bushing stiffnesses (4), (5)
$c_{\text{dyn}}$	dynamic stiffness, complex stiffness
$C_i$	constant factor $i$
$d$	viscous damping coefficient
$d_1, d_2, d_3$	viscous damping coefficients in local element coordinates 1, 2, 3
$D$	Lehr damping factor
$e$	Euler's number
$E_{\text{brake}}$	Energy dissipated in the brake
$E_{\text{drag}}$	Energy dissipated by air drag
$E_{\text{roll}}$	Energy dissipated by rolling resistance
$f_{d,\text{ref}}$	reference frequency for bushing damping evaluation
$f_{H,\text{ref}}$	reference frequency for equivalent viscous damping
$f_{r,\text{lim}}$	frequency limit for real mode computation
$F$	force
$F_{\text{damp}}$	transient damping force
$\Delta F$	maximum transient force change
$F(i\omega)$	frequency response function

$F^+, F^-$	conjugate-complex frequency response functions
$g_{\text{damp}}$	structural damping coefficient
$G(s)$	transfer function
$i$	imaginary unit
$m$	mass
$m_{\text{veh}}$	vehicle mass
$M$	moment
$M_{\text{yaw}}$	yaw moment
$p$	excitation force
$p^+, p^-$	conjugate-complex excitation force amplitudes
$p_B$	brake pressure
$P_{\text{brake}}$	Power of the brake system
$r$	radial displacement
$\dot{r}$	radial speed
$s$	complex number frequency parameter
$t$	time
$T$	cycle time
$V_2, V_T$	amplification function due to displacement excitation / transmissibility function
$v_{\text{lin},i}$	reference speed for friction linearization
$v_{\text{ref}}$	vehicle reference speed
$v_{\text{veh}}$	vehicle speed
$W_{\text{damp}}$	damping work, dissipated energy per oscillation cycle
$x$	(horizontal) displacement
$\dot{x}$	speed
$\ddot{x}$	acceleration
$x^+, x^-$	conjugate-complex displacement amplitudes
$\Delta x$	maximum transient displacement change
$y$	(vertical) displacement
$\dot{y}$	(vertical) speed

## Vectors

$\vec{\phi}_i$	real eigenvector
$\vec{\phi}_{c,i}$	complex eigenvector
$\vec{f}_N$	contact normal force
$\vec{f}_R$	Coulomb friction force
$\vec{q}$	modal displacement
$\dot{\vec{q}}$	modal speed
$\ddot{\vec{q}}$	modal acceleration
$\vec{v}_{\text{rel}}$	relative local speed vector between pads and disk
$\vec{x}$	Cartesian displacement

## *Symbols*

---

$\vec{x}_0$	Cartesian static rest position
$\Delta\vec{x}$	Cartesian displacement deviation
$\Delta\dot{\vec{x}}$	Cartesian speed deviation
$\Delta\ddot{\vec{x}}$	Cartesian acceleration deviation

---

# 1 Introduction

## 1.1 Motivation

How a passenger senses a vehicle's comfort and overall quality can be essentially influenced by its Noise, Vibration and Harshness<sup>1</sup> behavior. Here, brake systems play an important role – warranty claims caused by uncomfortable noise or vibration are a common issue Original Equipment Manufacturers<sup>2</sup> have to deal with, [41]. Brake squeal, a friction-induced vibration phenomenon, has already been investigated for many years. Current efforts aiming at a higher share of hybrid and Battery Electric Vehicles<sup>3</sup> – which naturally produce very low noise emissions in the drivetrain – in combination with still growing customer demands in terms of comfort have led to an increased interest in low-frequency phenomena such as creep groan or moan. In order to minimize design costs, it is desirable to foresee brake-related NVH problems and perform correcting actions already at an early stage of the development process. Especially in the context of highly diverse vehicle fleets, simulative tools play an important role for this so-called front-loading of the development process.

At the moment, two simulative methods are mainly used for the evaluation of a vehicle disk brake system's NVH performance:

- Time domain approaches
- Complex Eigenvalue Analysis (CEA)

Time domain approaches, whether implicit or explicit, have currently been applied mainly on reduced order models for gaining knowledge about the underlying mechanical and tribological mechanisms, see e.g. [44]. Application on large-scale vehicle corner models for the NVH evaluation at many different parameter points is not common due to high computation times. However, the inclusion of non-linear effects enables these approaches to deliver rather accurate results when compared with test bench experiments, see e.g. [56].

By contrast, the linearized CEA is able to process a high number of variants with varying parameters efficiently. By including important effects of the frictional contact between brake disk and brake pads, the stability behavior can be analyzed with this quasi-static approach. In industrial applications, this tool is applied on full-scale

---

<sup>1</sup>NVH

<sup>2</sup>OEM

<sup>3</sup>BEV

Finite Element<sup>4</sup> models of vehicle suspension and brake systems in order to evaluate their vulnerability for the tonal mid- to high-frequency brake squeal. Although well-established, this method sometimes still leads to wrong and rather over-critical results, as only the tendency for excitation can be computed: The reached real-life amplitudes, strongly depending on damping characteristics, cannot be estimated. [11], [14], [58]

In the course of a multi-year project, another publication treating the application of CEA on low-frequency brake phenomena has been created by the author apart from this work, see [38]. Therefore, the reader will often find similar, but also more detailed contents here: In addition to already published results of CEA simulations of a vehicle's front corner, a more sophisticated evaluation of moan-related eigenmodes, detailed evaluation of the system matrices and a recommendation regarding the build-up of a reduced-order, transient model are shown. What is more, high-quality validation with results from corresponding experimental tests on a drum-driven suspension and brake test rig are included.

## 1.2 Scientific Approach and Structure

At first, basics about disk brake systems, elastomer bushings and nonlinear oscillation are presented together with a review of brake-related NVH phenomena in chapter 2. Especially the low-frequency range with creep groan and moan is treated in detail. Furthermore, an analysis of the brake squeal CEA procedure is given similar to the author's work presented in [38]: It prepares the reader for the interpretation of simulative results.

In chapter 3, a full vehicle's front corner in double wishbone design with fixed caliper brake was investigated by means of CEA. Several variants were computed in order to explore the influence of certain parameters such as bushing stiffness and damping. In comparison to [38], moan simulation gained increased focus.

In chapter 4, CEA results regarding displacement pattern, frequency and stability are presented extensively. Here, a novel, multi-dimensional stability diagram developed for [38] is explained and used.

Extensive validation with both test bench results of the same axle configuration and results found in various literature works is given in chapter 5. After a detailed discussion, recommendations for further improvement of the method and ideas for the build-up of a reduced-order model suitable for transient simulation are stated.

Lastly, chapter 6 states main outcomes of the performed research as well as the conclusions that can be drawn from this work.

---

<sup>4</sup>FE

---

## 2 State of the Art

### 2.1 Passenger Vehicle Brake Systems

In this first chapter, basic requirements on brake systems followed by the structure of common brake systems of passenger vehicles are presented, mainly based on [10]. Emphasis is laid on disk brake systems due to their almost unchallenged usage at the front axle.

What is more, current trends in automotive and brake industry and their possible consequences for brake NVH are shown, mainly based on panel discussions and presentations performed at the 35<sup>th</sup> annual of *SAE Brake Colloquium & Exhibition*, see [5], [21], [31], [36], [48].

#### 2.1.1 Basic Requirements

Basically, a brake system has to perform the following three functions, [10]:

- retarding brake: decelerate the vehicle (until standstill at a certain position)
- holding brake: prevent acceleration of the vehicle during downward drive
- parking brake: avoid movement of a parked vehicle

These basic tasks lead to demanding requirements for the whole system as well as single components. As the brake system is highly safety-relevant in terms of accident avoidance, its functionality has to be maintained in a robust manner even under harsh environment conditions. Certainly, a definite deceleration or a maximal braking distance at a certain brake pedal force – related to the braking power of the vehicle – needs to be maintained, which is also regulated by legal requirements.

For a full stop, a frictional brake system needs to dissipate the kinetic energy of the vehicle reduced by minor dissipation due to rolling resistance and air drag, see eq. 2.1.

$$E_{\text{brake}} = \frac{m_{\text{veh}} \cdot v_{\text{veh}}^2}{2} - E_{\text{roll}} - E_{\text{drag}} \quad (2.1)$$

Stated in [10], tests of passenger vehicles from the years 2010 and 2011 revealed a mean braking distance from 100 km/h to standstill of approximately 37 m. Hence,

a mean deceleration of 1.06 g results – for a vehicle with a mass of 1500 kg and neglected losses due to rolling resistance and air drag, an energy of 578.7 kJ has to be dissipated by the brake system within 2.66 s. According to eq. 2.2, a mean braking power of 217.6 kW results. Bearing in mind that passenger vehicles often reach higher speeds, one can see that the linearly speed-dependent brake power can reach multiples of the engine power.

$$P_{\text{brake}} = \frac{dE_{\text{brake}}}{dt} \approx \frac{\Delta E_{\text{brake}}}{\Delta t} \approx \frac{578.7}{2.66} \text{ kW} = 217.6 \text{ kW} \quad (2.2)$$

As driving stability can be highly influenced in a negative manner by blocking wheels, some laws demand a certain blocking sequence: E.g., the rear wheels need to block after the front wheels for a deceleration between 0.15 g and 0.8 g in Europe. Details can be found within [10].

In addition, parts need to perform during an adequate service life in a reliable, wear-compensating manner.

For good handling, retarding and holding brake need to be easy to modulate. Ergonomic control elements also play an important role for a simple and safe usage of the brake. The factor comfort is also included within the wide area of NVH issues related to vehicle brakes, see chapter 2.4.

Eventually, environmental influences, e.g. in terms of particle emissions or hydraulic fluid components, lead to (increasing) demands and regulations. See also section 2.1.3.

Over the last century, these basic functions and requirements led to reliable, powerful and comfortable brake systems based on the principle of frictional dissipation. Whereas the drum brake as a basic concept with radial brake force application was practically unrivaled during the first half of the 20<sup>th</sup> century, its drawbacks regarding heat flow, fading, NVH and high brake force changes with varying coefficient of friction led to a replacement by (more temperature-resistant) disk brakes - first at front axles, by now also at rear axles, [10]. Therefore, the basic structure of conventional, hydraulically activated disk brakes is explained in the following chapter.

### 2.1.2 Structure of a Conventional Passenger Vehicle Disk Brake System

A conventional, vacuum-boosted, hydraulically activated disk brake system can be divided by function. The resulting four main sub-groups, based on [10] and depicted in fig. 2.1, are:

- Ⓐ Human Machine Interface<sup>1</sup>

---

<sup>1</sup>HMI

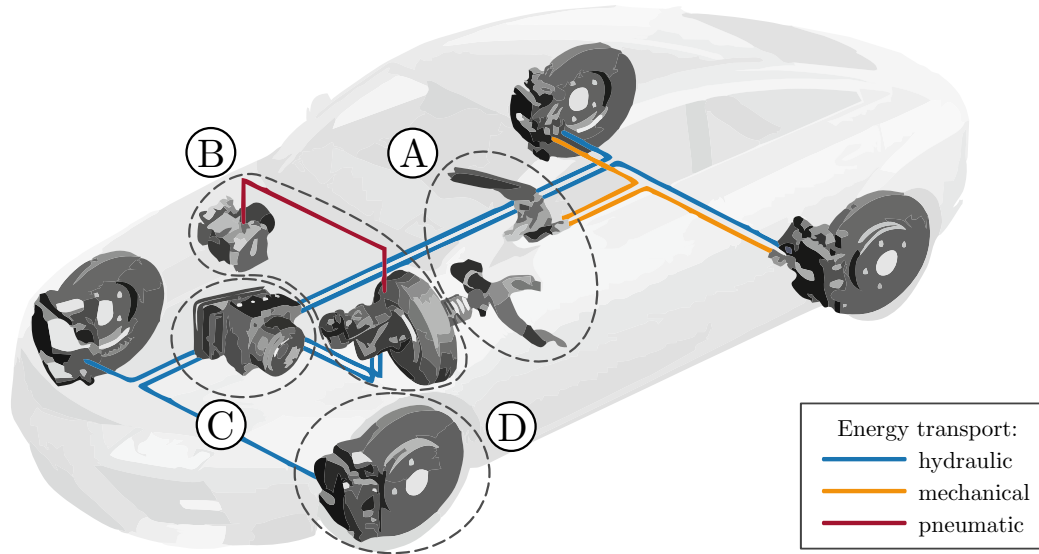


Figure 2.1: Functional groups of a vacuum-boosted, hydraulically activated passenger vehicle brake system, adapted from [10]

- (B) actuation with transmission elements
- (C) brake force transmission and modulation
- (D) brake force generation

As the functional group of brake force generation is of main relevance for brake NVH behavior, components of the other groups shall be mentioned only sketchily here.

(A) The HMI contains all parts the human driver directly interacts with. Typically, these include a usually pendulously mounted brake pedal for the service brake and a hand lever for the parking brake. As presented in chapter 2.1.3, the share of cars with electric park brakes is increasing: Here, the hand lever is replaced by a button for electronic control of the parking brake.

(B) The actuation force of the brake pedal is increased by a certain auxiliary force provided via a vacuum (or sometimes hydraulically) powered brake booster. Especially for Otto engines, the necessary depression is available anyway, however, with (nowadays widely spread) fuel injected Diesel and Otto engines an additional vacuum pump is necessary. For further functionality such as Electronic Brake Assist or Adaptive Cruise Control<sup>2</sup>, active brake boosters with an integrated magnetic actuation are used.

In the following, this increased force is applied mechanically to the tandem mas-

<sup>2</sup>ACC

ter cylinder, which converts the mechanical force into a hydraulic pressure within the brake fluid. Two pistons create the pressure within the two legally-required, separate brake circuits. In a non-activated position, the main pressure chambers are connected to a brake fluid reservoir via sniff ports, or, when electronic control functions such as Antilock Brake System<sup>3</sup> or Electronic Stability Control<sup>4</sup> are implemented, via central valves or a special plunger design. The reservoir fulfills important functions such as brake fluid volume compensation for worn pad linings or different environmental conditions (air pressure, temperature), reduction of foam development and the prevention of air inflow. [10]

Ⓒ A modulation of the pressures produced in the tandem master cylinder is necessary for several reasons: Firstly, dynamic axle load shifts due to braking create a demand for variable brake proportioning between front and rear axle. For high load shifts, less tire vertical force emerges at the rear axles, making braked rear wheels block more easily. Therefore, a certain reduction of the brake force proportion of the rear axle is required. This can be ensured either by a classical mechanical-hydraulic brake pressure modulation or by electrical-hydraulic brake pressure modulation.

Usually, a so called Hydraulic-Electronic Control Unit<sup>5</sup> is used. It contains a twin-circle piston pump for the separate brake circuits, inlet, outlet and nonreturn valves as well as the electronic control unit, which processes sensor signals and controls the actuators. Electronic functions such as ABS, ESC or Traction Control System<sup>6</sup> can be performed by this unit.

The modulated brake pressures are transmitted via the brake fluid, which has also the task of providing lubrication to pistons, valves and seals. Transmission is taken in double-wound hard-soldered steel pipes. For flexible connections, hose lines consisting of an inner hose, a meshwork to withstand the pressure and an outer hose as protection against environmental influences such as saltwater, oil or fuels, are used. Typically, pressures up to 160 bar can be reached during operation. [10]

Ⓓ The functional group of the brake force generation represents the last chain link of the brake system. Components are basically:

- brake disk
- brake caliper
- brake pads

Basic principle is the axial push of the brake pads by the caliper's piston(s) towards the ring-shaped side surface of the rotor or brake disk, which is connected to the wheel. The resulting tangential force due to friction is transferred to the chassis via pads, caliper, wheel carrier and control arms. Among other things, typical properties

---

<sup>3</sup>ABS

<sup>4</sup>ESC

<sup>5</sup>HECU

<sup>6</sup>TCS

of disk brake systems are (see also [10]):

- high thermal load capacity
- smooth response
- uniform wear of the pad linings
- simple and automatic wear adjustment
- favorable disengaging behavior
- low remaining moment for disengaged brake pads

### 2.1.2.1 Brake Disk

With approximately 90 %, the brake disk needs to take most of the dissipated heat energy produced in the frictional contact with the pad linings, [10]. Very high temperatures up to 700 °C can be reached. Certainly, the thermal state can influence the structural behavior and the Young's modulus of the disk material, which is considered also within NVH related simulation, see e.g. [14]. What is more, temperature changes can lead to coning, warping or even to waved deformations of the rotor. Problems regarding NVH behavior or non-uniform pad lining wear are the consequence.

Brake rotors can be distinguished in massive and ventilated disks. The main advantage of a ventilated disk is its optimized convective flow of heat. In this case, the air stream is guided by inner cooling channels. Often these are not only designed for an optimized flow but also for a certain eigenfrequency behavior of the disk in terms of brake squeal avoidance.

Due to several reasons, lightweight brake disk designs are desirable. The size and therefore also the weight of the disk directly control the size of brake caliper and pads. With increasing brake power, e.g. due to an increase in engine power, larger and often heavier brake parts are the result. This rise of mass and rotational inertia directly influences the vehicle's overall mass and therefore its climbing resistance. Furthermore, the disks contribute to the unsprung mass at every single wheel, dimensioning of the damper is directly affected too. Therefore, material (mix) as well as geometric design can play an important role in brake disk design. [10]

Usually, rotors are made of lamellar-graphite cast iron (e.g. EN-GJL-150 ... 250) which also provides a certain level of material damping. Here, specific alloy additions are used for optimization of thermal conductivity, corrosion resistance or wear. For highest demands, sophisticated carbo-ceramic (C/SiC) designs are available, delivering high wear resistance combined with low weight. Of minor importance are brake disks based on aluminum, so-called Aluminum Matrix Compounds<sup>7</sup>, which could also provide high weight reduction potential. [10]

---

<sup>7</sup>AMC

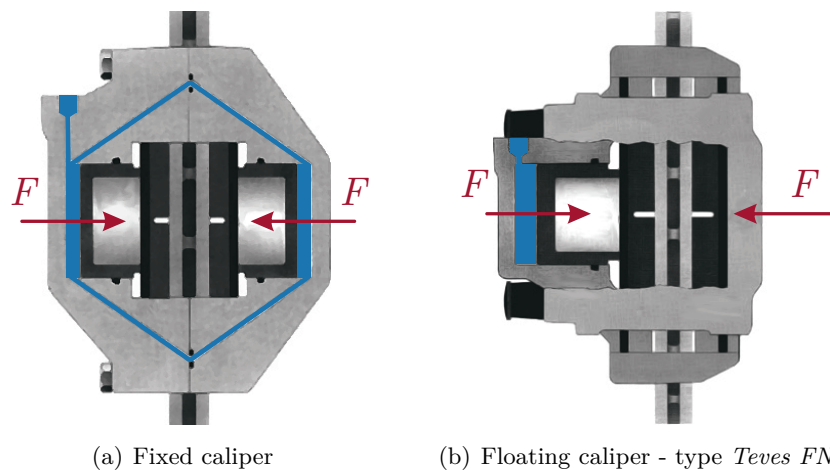


Figure 2.2: Schematic sketches of basic brake caliper designs, adapted from [10]

In terms of geometric design, low inertia can be reached by a compound brake disk. Especially in the high-performance sector, designs consisting of a ring (friction material) connected to a pot-shaped inner part (lighter material, e.g. aluminum) are used. The connection can be provided either via rivets/pins or without any additional parts by a form fit. An example for a compound brake disk is contained in the evaluated model explained within chapter 3.1, see also fig. 3.1. [10]

### 2.1.2.2 Brake Caliper

According to fig. 2.2 the basic design can be distinguished in fixed and floating calipers. In [10], floating calipers are separated further in different sub-groups.

As one can see in fig. 2.2 (a), a fixed caliper brake is characterized by the caliper's axial attachment and pistons on both sides of the disk. Especially for front axle brake systems of high-performance cars, this rather stiff design is used. The caliper itself can consist of two separate parts, with additional sealing effort for the inner hydraulic brake fluid connections, or of one singular part (monobloc design) with reduced weight and better NVH behavior. An example of an aluminum monobloc caliper can be found in the model presented within chapter 3.1. [10]

By contrast, a floating caliper's piston is positioned only on one side of the brake disk - due to design space reasons, this is typically the vehicle-facing side, fig. 2.2 (b). Additionally, the caliper itself is guided axially on pins, enabling a push of both pads towards the rotor. The tangential forces arising at the frictional surface of the pad linings are supported directly at the frame. Often, the principle of pull-push support is used here for uniform lining wear and enhanced NVH behavior.

Calipers are usually made of nodular cast iron, or, for reduced weight, of aluminum.

For the mostly hollow pistons, grey iron, steel, aluminum or plastics are used. [10]

Another important part of the caliper assembly are the usually square shaped piston seals which enable ‘Roll Back’ and ‘Knock Back’: A pull action on the piston carried out by the elastically deformed seal in disengaging or engaging direction respectively. By the design of seal and groove, this characteristic and therefore the remaining brake moment for a disengaged brake can be manipulated. [10]

### 2.1.2.3 Brake Pads

Brake pads basically consist of a back plate and a friction lining, which comes in contact with the brake disk. Furthermore, damping shims for the reduction of brake squeal noise are often mounted on the outer side of the back plate.

The back plate is usually made of steel stamped out of a coil. Amongst other things, the fit to the frame/caliper and its changes due to thermal expansion are an important development issue, as it affects the remaining torque. [16]

The friction lining itself is usually a sintered composite of different components. Depending on factors such as brake power, desired NVH behavior or production of brake dust, different concepts are used for different target markets:

- semimetallic linings
- low steel linings
- Non Asbestos Organics<sup>8</sup> linings
- metal-free linings
- hybrid linings

*Semimetallic linings* or *semimets* were the first approach towards a replacement of asbestos: Here, more than 50 % of the lining is metal/iron. Biggest drawback of this formulation is high wear for higher speeds and vehicle masses due to low thermal stability of the contained steel wool/iron powder. However, low wheel dust and a favorable NVH comfort due to their low coefficient of friction  $\mu \leq 0.4$  led (again) to increased usage in the USA. [10]

*Low steel linings* or *low mets* originally tried to replace asbestos by different organic and mineral fiber components. In the following, their share was reduced – also for health reasons due to possibly carcinogen fibers. Instead, different other additives such as lubricants, abrasives or metals were used. These linings, also called *corrective liners*, show high friction coefficients and are mainly applied in Europe. Main weakness is their NVH comfort, especially in terms of the low-frequency phenomenon creep groan explained within chapter 2.4.1.1. [10]

---

<sup>8</sup>NAO

*NAO linings* represent the Japanese lining philosophy: Here, neither steel wool or iron powder nor any hard abrasives are used. Therefore, the resulting coefficient of friction is rather low in the range of  $\mu = 0.3 - 0.4$ . Again, this leads to low wheel dust and good NVH behavior for vehicles below 3.5 t gross vehicle weight. Specifically in terms of creep groan, these linings deliver an excellent performance. In addition to the Japanese market, NAOs are common in the USA. [10]

*Metalfree linings* go even further and omit other non-ferrous metals such as copper or brass. Especially copper has been in public discussion in the USA, as increased shares of copper were measured in run-off water near San Francisco, California, see [54]. At least local laws regarding copper shares of brake pads were the result, restricting the copper content in a first stage in 2021, [8]. In general, metalfree linings suffer from low thermal conductivity and reduced strength due to the missing metals, therefore applications are still rare. [10]

*Hybrid linings* try to combine comfort characteristics of NAOs with the high performance of low steel linings. Especially for the treatment of creep groan issues, these rather new formulations try to deliver a solution. However, this relatively new mixture concept still has difficulties with opposing trends: Tests have shown increased groan tendency for former groan-free NAO linings when a low amount of steel wool or hard abrasives were added. [10]

Connection between lining and back plate can be achieved by the lining's underlayer and/or mechanical fixations such as e.g. 'combed' plates. The underlayer with a thickness of approx. 2 – 4 mm has a different chemical composition than the lining in contact with the disk: A higher percentage of the binding agent leads to increased strength and therefore a good mechanical connection to the steel plate. Furthermore, an adhesive layer of a few  $\mu\text{m}$  thickness connects the composite's underlayer with the steel back plate. [10]

### 2.1.3 Current Trends and Future Concepts

Several major and minor trends can currently be observed within the automotive industry. Keywords such as battery electric vehicles, autonomous driving or vehicle emissions and related scandals are part of daily media reports. Even though a definite prediction is impossible, certain developments and their impacts on brake system design and structure can already be seen.

According to [21], vacuum-less brake boosters as well as Electric Parking Brakes<sup>9</sup> will most probably gain importance and market propagation. For the EPB, an increase of reliability and safety as well as additional comfort functions drive development and implementation. Regarding alternatively powered boosters, hybrid/electric drivetrains as well as fuel injected engines do not feature direct vacuum sources -

---

<sup>9</sup>EPB

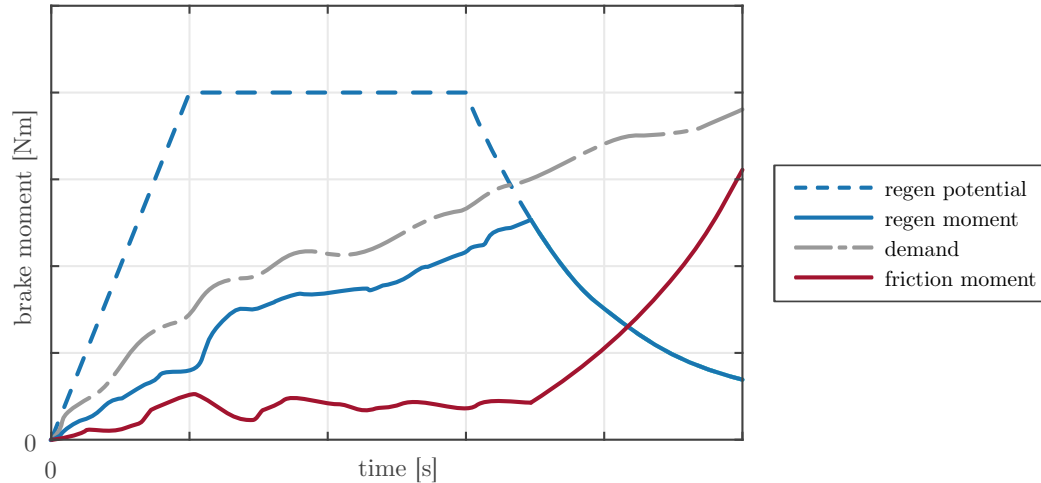


Figure 2.3: Schematic depiction of brake torque blending, adapted from [5]

therefore, electric brake boosters seem beneficial in terms of efficiency and costs, see [10].

Moreover, hybrid and battery electric vehicles have the ability to regenerate kinetic energy by using the electric drivetrain in generator mode. Several aspects and demands arise from this colloquially-called *regen mode*:

Firstly, the braking action needs to be performed in a smooth manner. Therefore, brake moments of the frictional (disk) brake system and of the electric motor/generator system have to be controlled and blended according to the regenerative potential and the driver's demand, see fig. 2.3. This makes a high controllability of the the auxiliary brake force generation necessary, which can be found as another advantage of electric brake boosters.

Secondly, usages of the frictional brake will be limited to braking actions with higher decelerations: According to [31], approx. only one out of eight brake actions is performed by the disk brake system. [36] estimates the possible deceleration in purely regenerative mode as 0.05 g for mild hybrid vehicles and 0.2 – 0.3 g for full hybrids. Hence, the self-cleaning function of the brake rotor is reduced significantly and corrosion problems during the disk's increased life span are likely. Currently, no solution to this problem is known to the author. According to [21], even a return of the encapsulated drum brakes - although unlikely - could be possible. What is more, this reduced usage of the frictional brake could lead to its downsizing, whereas of course overall safety criteria need to be met, [48].

Thirdly, operational points critical for low-frequency noise and vibration will be approached more often - both due to blending functions and because of the consistently acting drive torque of vehicles with automatic gearboxes or electric drivetrains. This can lead to higher importance of the low-frequency NVH issues creep

groan or moan, which are treated in this work.

Further lining developments certainly represent an additional aspect of high influence towards future NVH behavior. Especially (almost) copper free formulations and hybrid lining formulations can be of high relevance, [54]. Moreover, legislation for the reduction of brake particle emissions could probably introduce significant limitations in terms of lining composition.

Eventually, concepts such as Brake-by-Wire or the combination of wheel and rotor, although seeming rather futuristic, are discussed as long-term solutions. Regarding NVH, this could also enable approaches on behalf of active feedback control. [21], [48]

## 2.2 Elastomer Bushings

As the following chapters will show, the behavior of elastomer bushings can affect the dynamic properties of a passenger car's axle system significantly. Usually, these components are not the focus of the brake engineer. Therefore, this chapter tries to give the reader an overview about basic demands and features.

Being classical parts of vehicle chassis and suspension design, requirements on elastomer bushings relate to the following three main parameters:

- driving dynamics
- driving comfort
- driving safety

Historically, the introduction of elastomer bushings for suspension links was mainly driven by the demand for comfort. Firstly applied in the thirties of the 20<sup>th</sup> century, they were initially intended to isolate and dampen (structure-borne) noise, vibration and harshness induced by the road surface, [32]. Development over many years expanded and improved their functionality.

Nowadays, elastomer bushings fulfill three basic tasks, see [32] and [50]. Firstly, they are often used instead of ball joints, i.e. they enable angular changes between the two connected components. Secondly, they fulfill the demand for comfort by introducing additional (longitudinal) compliance, oscillation damping and isolation within the axle system – sometimes also in terms of an active component. Thirdly, they (partly) define and influence the vehicle's dynamic steering and tracking behavior under different loads.

In the following, these three main tasks are investigated in detail.

### 2.2.1 Joint Function of Elastomer Bushings

Using rubber bushings instead of ball joints implies several advantages. On the one hand, costs can often be lowered. On the other hand, breakaway forces – usually a consequence of the transition from stick to slip in the ball/pan contact – can be avoided. Furthermore, the inclusion of elasticity and damping in rotational directions can have desirable, positive effects. [50]

Nevertheless, the inevitably introduced rotational stiffness and damping can also be unwanted in some situations. E.g. if large rotational displacements are applied, the function as a joint can be limited due to high intersection forces. [50]

### 2.2.2 Oscillation Reduction via Elastomer Bushings

In order to increase comfort, a reduction of oscillation amplitudes is necessary. For reaching this goal, two fundamental concepts can be applied: damping and isolation.

#### 2.2.2.1 Oscillation Damping and Dynamic Stiffness Behavior

Oscillation damping means a direct decrease of vibration amplitudes by the transition of motion energy to heat energy. Here, inner friction within the bushing provokes this process. Due to its mathematical simplicity, engineers often assume this process to be purely speed-dependent with the damping force relating to a (mostly) constant viscous damping coefficient. [50]

However, real elastomer damping is typically a highly complicated mechanism depending on the material's visco-elastic behavior, pre-load, temperature or oscillation frequency as well as the displacement amplitude itself. According to [50], similar statements can be given for elastomer stiffness characteristics: Strong dependencies on excitation frequency, amplitude or temperature can be found here. For an explanation of dynamic stiffness and related terms, see chapter 3.1.2.2.

Generally speaking, increasing excitation frequency leads to a rise of dynamic stiffness and damping within the elastomer. This is due to a dynamic hardening process for increasing frequencies, leading to higher inner friction with the result of stronger damping. Furthermore, higher excitation amplitudes usually result in a decrease of dynamic stiffness, see [32] and [50].

In fig. 2.4, measured stiffness and loss angle characteristics are shown over frequency for an elastomer bushing used in a double wishbone front axle setup. The stated stiffness rise for increasing frequency or decreasing excitation amplitude is clearly observable. Regarding the damping-related loss angle, higher frequencies as well as higher amplitudes lead to a rise for the presented measurement data. This frequency-varying behavior can be influenced strongly by elastomer filler media, especially carbon black is of high relevance. [50]

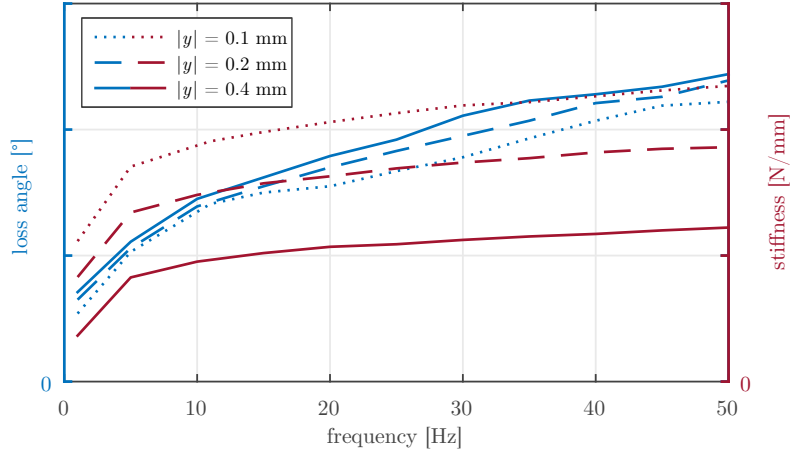


Figure 2.4: Measured dynamic stiffness and loss angle characteristics of a control arm's elastomer bushing in radial direction over frequency for different excitation amplitudes  $|y|$

Naturally, static elastomer bushing stiffness is often required in a non-linear manner too: As bushing displacements need to be limited for high chassis forces, a non-linear increase is often necessary.

### 2.2.2.2 Oscillation Isolation

Oscillation isolation describes a different effect: Here, vibration amplitudes at a critical position within the system (e.g. at the connection points on the chassis) are reduced by tuning the eigenbehavior of the adjacent system components.

For better understanding, a displacement-excited single mass oscillator according to fig. 2.5 (a) is investigated, see [18] and [50]. Here, we also include oscillation damping by a viscous element with a viscous damping coefficient  $d$ .

Starting from the equation of motion in eq. 2.3, a division by the spring stiffness  $c$  combined with the introduction of the damping factor according to Lehr  $D$  and the undamped eigenfrequency  $\omega_0 = \sqrt{\frac{c}{m}}$  leads to eq. 2.4.

$$m \ddot{x}(t) + d \dot{x}(t) + cx(t) = d \dot{y}(t) + cy(t) \quad (2.3)$$

$$\frac{1}{\omega_0^2} \ddot{x}(t) + \frac{2D}{\omega_0} \dot{x}(t) + x(t) = \frac{2D}{\omega_0} \dot{y}(t) + y(t) \quad (2.4)$$

By a rather simple transformation to the Laplace domain, the transfer function between excitation  $y(s)$  and reaction  $x(s)$  can be found according to eq. 2.5.

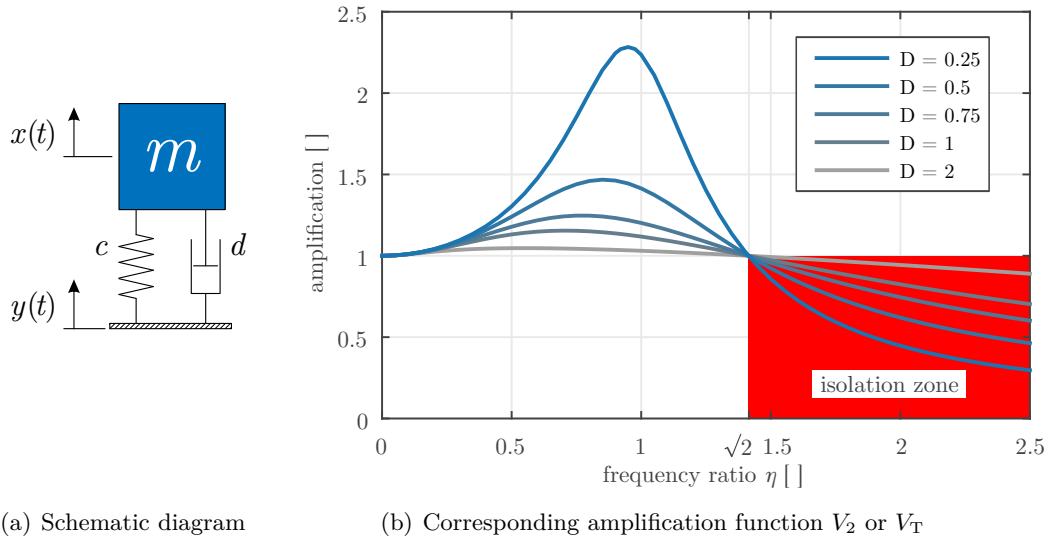


Figure 2.5: Displacement-excited single mass oscillator

$$G(s) = \frac{x(s)}{y(s)} = \frac{1 + \frac{2D}{\omega_0} s}{1 + \frac{2D}{\omega_0} s + \frac{1}{\omega_0^2} s^2} \quad (2.5)$$

As the complex number frequency parameter  $s$  relates to the imaginary unit and the rotational eigenfrequency of the resulting oscillation with  $s = i\omega$ , a transition to frequency domain is trivial. After introducing the frequency ratio  $\eta$  according to eq. 2.6, the frequency response function in eq. 2.7 results.

$$\eta = \frac{\omega}{\omega_0} \quad (2.6)$$

$$G(\omega) = \frac{1 + 2D\eta \cdot i}{1 - \eta^2 + 2D\eta \cdot i} \quad (2.7)$$

Now, calculation of the absolute value delivers the amplification function  $V_2$  or  $V_T$  (for transmissibility), see eq. 2.8 and [18].

$$V_2 = V_T = \frac{|x(i\omega)|}{|y(i\omega)|} = \sqrt{\frac{1 + 4D^2\eta^2}{(1 - \eta^2)^2 + 4D^2\eta^2}} \quad (2.8)$$

When plotted depending on the frequency ratio  $\eta$ , as in fig. 2.5 (b), the isolation zone is found for frequency ratios  $\eta > \sqrt{2}$ . By associating the chassis displacement with  $x(t)$  and the bushing displacement with  $y(t)$ , one can see that rather high

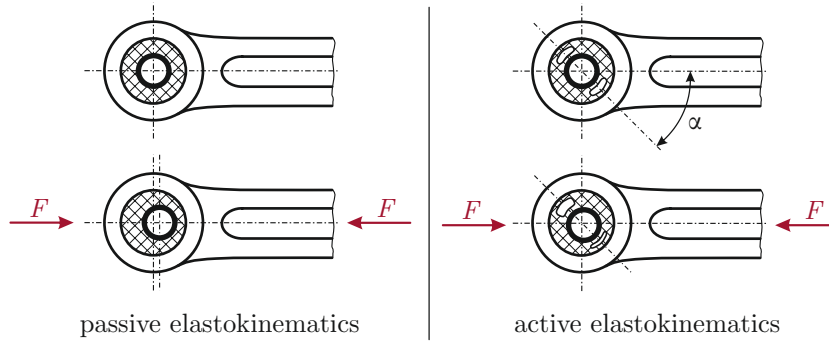


Figure 2.6: Examples for passive and active elastokinematic effects, based on [35]

elasticity within the bushing is necessary to ensure vibration isolation also for lower frequency excitation, as this means a lower eigenfrequency  $\omega_0$  and therefore an increase of the frequency ratio  $\eta$ . Practically, elastomer stiffness is chosen approx. 1:10 compared to the local chassis stiffness, [50].

Regarding damping, fig. 2.5 (b) also reveals an interesting negative side-effect in the isolation area: With higher damping, higher bushing forces occur; therefore, less isolation is provided. However, the operation near working points of  $\eta \approx 1$  cannot be prevented. This – and the fact that in the range below  $\eta = \sqrt{2}$  damping leads to a reduction of the response amplitude – makes a certain amount of damping necessary for a well-balanced overall performance of the elastomer bushing. [50]

### 2.2.3 Elastokinematic Behavior

This chapter contains basic considerations about the third main task of an elastomer bushing, relating to a vehicle’s elastokinematic design. Again, this is done in order to inform the reader about the area of conflict in which brake NVH related elastomer bushings have to be designed.

*Elastokinematics* describe a vehicle’s kinematic behavior due to the deformation of elastic suspension components, see [32]. Here, passive aspects of inevitable compliances need to be distinguished from ‘active’ compliances produced by design: In this case, ‘active’ does not refer to a behavior in terms of feedback control but to a design leading to directed displacements under load, [35]. An example can be seen in fig. 2.6.

In addition to the elastomer bushings in focus, metal parts such as wishbones or the kinematic chassis mounting points perform significant deflections too. Therefore, they cannot be neglected for elastokinematic design. Furthermore, aging effects of the rubber material during the vehicle’s life cycle have to be considered: A hardening effect can occur for elastomers. By contrast, metals basically keep their elasticity. Details can be found within [50].

For elastokinematic optimization, different load directions require different measures. On one hand, high compliance in the range of  $\pm 20$  mm is aspired in longitudinal direction in order to reduce the influence of occurring low-frequency longitudinal shocks. Rubber bushings of low stiffness make up for the better part of this compliance, significantly increasing comfort characteristics. On the other hand, the demand for exact and safe cornering leads to low compliance in lateral direction, see [32].

By modifying or changing axle concept, position and dimension of levers or elasticities within the suspension system, parameters such as camber angle, roll center, vehicle pitch or tracking are influenced by the developers. According to the driving situation, different elastokinematic behavior should result. This often leads to opposing demands, compromise is necessary. [32]

In the following, toe-angle changes are explained for several different driving and load situations. Generally, a stable understeering behavior is desired for different load changes.

### 2.2.3.1 Elastokinematic Behavior for Vertical Load Changes

Especially for changes of vertical loads induced by vehicle roll movement, kinematic understeering behavior is requested. Hence, the subsequent toe-angle changes should result according to table 2.1.

Table 2.1: Toe-angle tendency for increasing vertical load

<b>front axle</b>	outer wheel	toe-out
	inner wheel	toe-out
<b>rear axle</b>	outer wheel	toe-in
	inner wheel	toe-in

These measures lead to an increase in driving stability, however, certain drawbacks in terms of straight-ahead run are inevitable. [19]

### 2.2.3.2 Elastokinematic Behavior for Lateral Load Changes

For occurring lateral loads, understeering behavior is desired. Therefore, elastokinematics should lead to the effects stated within table 2.2.

With a setting like this, slip angles increase at the rear axle and decrease at the front axle, leading to the desired stable understeering behavior. Due to higher forces during cornering, outer wheels are more important. See fig. 2.7 for a detailed depiction of the resulting elastokinematic steering angles  $\delta_{i,j}$ . [19]

Table 2.2: Toe-angle tendency for increasing lateral load

<b>front axle</b>	outer wheel	toe-out
	inner wheel	toe-in
<b>rear axle</b>	outer wheel	toe-in
	inner wheel	toe-out

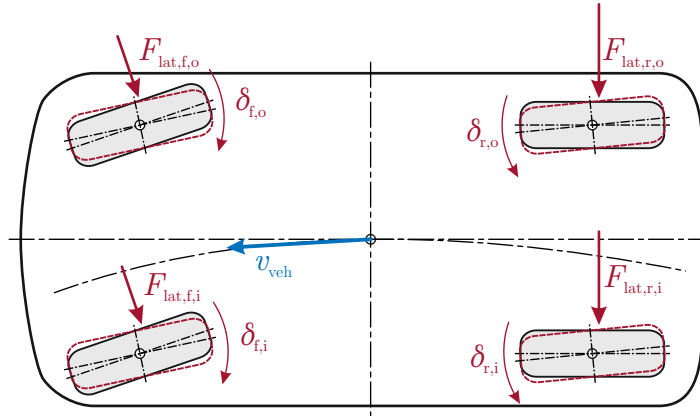


Figure 2.7: Desired changes of toe angles for optimal behavior under lateral load

### 2.2.3.3 Elastokinematic Behavior for Longitudinal Load Changes

For the occurrence of longitudinal loads, target conflicts arise due to different demands of several driving conditions – see the overview within table 2.3.

Table 2.3: Toe-angle tendency for different longitudinal loads

		acceleration or braking	$\mu$ -split braking	braking & cornering
<b>front axle</b>	outer wheel	toe-in	toe-in	toe-out
	inner wheel	toe-in	toe-in	toe-out
<b>rear axle</b>	outer wheel	toe-in	toe-out	toe-in
	inner wheel	toe-in	toe-out	toe-in

For straightforward acceleration and deceleration, higher driving stability is desired. This could be reached by a toe-in of front as well as rear axle. [19]

In case of braking on a track with higher coefficients of friction on either left or

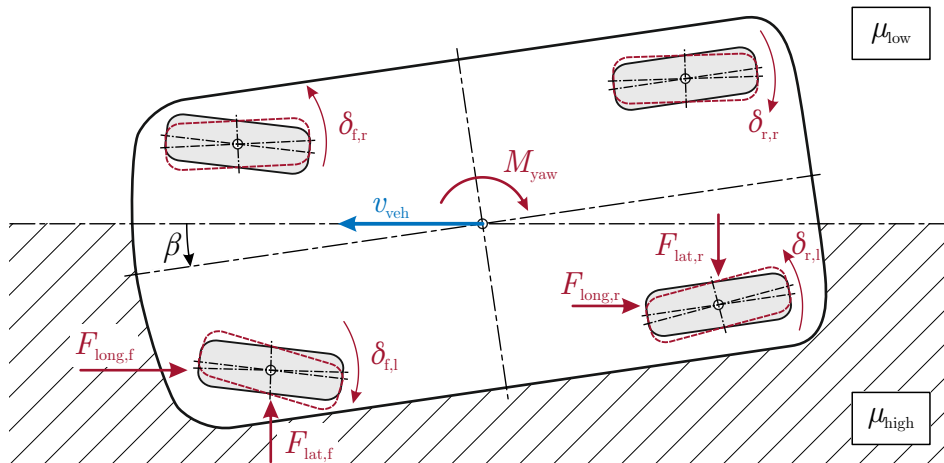


Figure 2.8: Desired changes of toe angles for optimal behavior under  $\mu$ -split braking, based on [32]

right side, a so-called  $\mu$ -split braking, a correcting yaw torque created by toe-in at the front axle and toe-out at the rear axle is desired. A depiction of elastokinematic steering angles  $\delta_{i,j}$  and resulting forces/moments can be found in fig. 2.8. As one can see, a well-designed elastokinematic behavior provokes the moment  $M_{\text{yaw}}$  which counteracts the undesired slip angle  $\beta$ . [19]

If the vehicle is decelerated during cornering, brake forces should lead to toe-out at the front axle and toe-in at the rear axle, again in order to create a stabilizing yaw torque. [19]

#### 2.2.3.4 Practical Approach for Elastokinematic Design

A simple single solution fulfilling all differing demands at once seems rather impossible. Therefore, vehicles are usually designed for

- small toe-out at the front axle and
- small toe-in at the rear axle

under cornering as well as under braking and cornering. Hence, the risk of oversteering behavior caused by axle load shifts due to braking is reduced and neutral behavior is ensured over a wide range of lateral accelerations. If possible, driven rear axles are dimensioned for toe-in under acceleration, see details within [19] and [32].

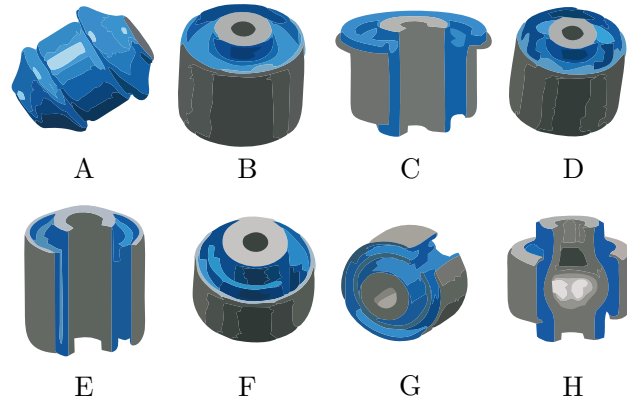


Figure 2.9: Examples for conventional elastomer bushing design, adapted from [32]

### 2.2.4 Design Examples

Based on the demands resulting from the three main tasks – joint function, oscillation reduction and elastokinematic behavior – different designs of elastomer bushings have been developed. Examples are:

- conventional bushings
- hydraulic bushings
- engaging and disengaging mounts
- active bushings

In general, elastomer bushings can be loaded with tension/compression forces or with shear forces. As the demands explained in the previous chapters have shown, the design of directional stiffness and damping is an important factor. For suspension systems, basically two different variants of elastomer bushings are currently used: conventional and hydraulic elastomer bushings.

Due to their cost effective design, conventional elastomer bushings are still widely used in many applications such as e.g. control arms. As one can see in fig. 2.9, an elastomer rubber part is typically positioned between two rotationally symmetric metal parts. Connection can be provided both by vulcanizing or mechanically via friction or the geometric shape. For directional behavior, ‘kidney’ designs similar to fig. 2.6 are common. [50]

For hydraulic elastomer bushings, displacements lead to a designed oil flow between two closed reservoirs within the bushing. With a principal design like this, two different effects can be reached: On the one hand, higher damping can be applied, on the other hand, harmonic absorption through the acceleration of the fluid’s mass is possible. This enables fine tuning of the bushing’s dynamic stiffness and damping characteristics, leading to an effective treatment of a system’s eigenfrequencies. Ap-

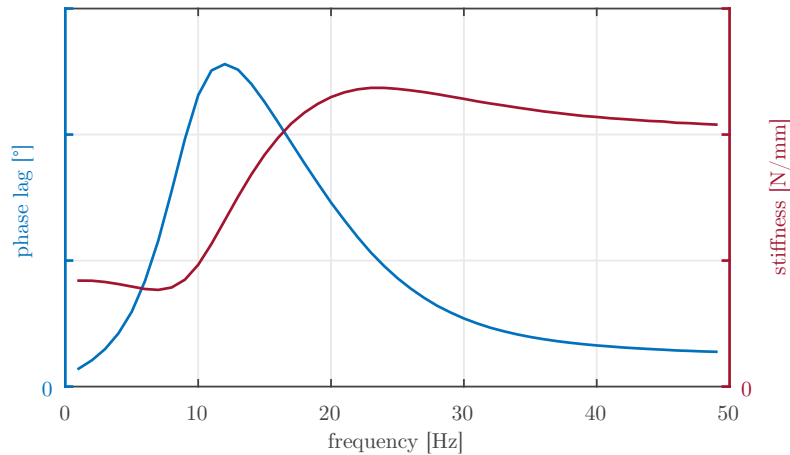


Figure 2.10: Measured dynamic stiffness and loss angle characteristics over frequency of a control arm’s hydraulic elastomer bushing in radial, horizontal direction for an excitation amplitude of  $|y| = 0.5$  mm

plications are especially longitudinal wheel vibrations but also the different field of propulsion system support, see [46] and [50].

A typical dynamic stiffness and loss angle characteristic of a hydraulic bushing tuned for highest loss angles at an excitation frequency of approx. 12 Hz is shown in fig. 2.10. For higher frequencies, an increase in stiffness is noticeable. This usually represents an unwanted effect due to the resulting comfort loss, see also [32] for details.

A corrective measure against this drawback especially taken for engine support bushings is the application of engaging and disengaging bushings: By changing the hydraulic system’s properties, e.g. for high oscillation isolation during engine idle and high damping during driving operation for a reduction of road-induced vibrations, the bushing’s frequency tuning can be modified. Hence, different stiffnesses or other requirements can be satisfied, see [32]. Especially for the support of diesel engines, engaging and disengaging mounts have high advantages and are widely used. Active bushings provide further potential regarding a faster and more sophisticated tuning of stiffness, damping or mass parameters by means of an active closed-loop or open-loop control system. However, actual applications in the field of suspension system bushings are unknown to the author. [50]

## 2.3 Nonlinear Oscillation Phenomena

According to [22], sources for non-linear behavior within a mechanical system can be classified in different groups as listed in table 2.4. Especially nonlinear action due to design and friction can be relevant for brake NVH behavior of a passenger

car's front axle: This shall be explained in the following paragraphs.

Table 2.4: Sources of non-linear behavior and examples, based on [22]

<b>type of nonlinearity</b>	<b>example</b>
geometrical nonlinearities	kinematics of a math. pendulum
physical nonlinearities	non-linear stress-strain relation
structural or designed nonlinearities	designed limit stops
constraints	impacts with rigid walls
nonlinearity of friction*	stick-slip transition

(\*) A clear classification of non-linear effects is difficult: E.g., nonlinearity of friction can certainly be seen as a physical effect too.

As shown in the previous chapter, elastomer bushings need to fulfill several different tasks. Therefore, a defined nonlinear stiffness or damping behavior is often a necessary premise, see e.g. the static stiffness behavior in fig. 3.4. Similarly, damping characteristics of elastomer bushings have also been shown to be highly depending on the frequency of the excitation, see e.g. fig. 2.4 or fig. 2.10. Again, this means a dependence on state variables such as displacement or velocity.

Moreover, frictional contacts manifest highly nonlinear behavior: Even the simplest possible explanation model, the Coulomb friction, contributes for different coefficients of sticking or sliding friction  $\mu_0$  and  $\mu$ . Another aspect of contact problems are small clearances between adjacent, loaded components: Again, nonlinear characteristics are introduced into the model, see [44].

These nonlinearities show clear influence regarding oscillation characteristics. Several different nonlinear effects can be found for the brake NVH phenomena creep groan, moan or squeal as explained in chapter 2.4.1. Some of these relevant nonlinear vibration anomalies will be investigated subsequently.

### 2.3.1 Super- and Subharmonics

Super- and subharmonic oscillations are a common phenomenon found within non-linear vibrations, especially for non-linear stiffness behavior. As already stated, elastomer bushings typically convey such characteristics due to the demands regarding comfort and safety.

In contrast to the typically sine-shaped displacement-over-time graph for a linear oscillation, gradually stiffening behavior leads to 'sharper' peaks in the displacement, velocity and acceleration charts. These peaks also relate to additional frequency content: Whole-numbered multiples are called superharmonics whereas whole-numbered fractions are termed subharmonics.

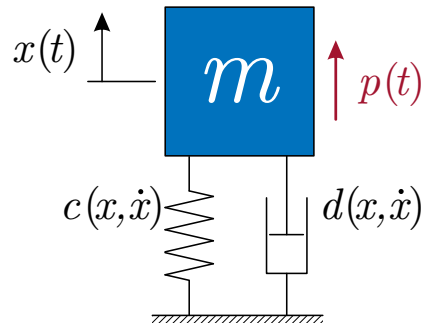


Figure 2.11: Schematic diagram of a force-excited single mass oscillator

Subsequently, three example simulations based on a force-excited single mass oscillator according to fig. 2.11 are shown to demonstrate this behavior. The corresponding equation of motion with a general non-linear elastic stiffness  $c$  and viscous damping  $d$  can be found in eq. 2.9.

$$m \ddot{x} + d(x, \dot{x}) \dot{x} + c(x, \dot{x}) x = p(t) \quad (2.9)$$

Table 2.5 shows the parameters used for the three different explicit numeric simulations performed with MATLAB. Variant I utilizes a linear stiffness behavior as depicted by a dashed line in fig. 2.12 (a). Variants II and III use non-linear stiffness behavior with 10 times higher stiffness for amplitudes bigger than 0.8 m, drawn with a solid line in the respective figure. Furthermore, variants I and II correspond to a free, undamped oscillation. Within the linear stiffness range, the undamped eigenfrequency results as in eq. 2.10.

$$\omega_0 = \sqrt{\frac{m}{c_0}} = \sqrt{\frac{1}{39.478} \frac{1}{\text{rad}}} \equiv f_0 = 1 \text{ Hz} \quad (2.10)$$

In order to find super- or subharmonic frequency content, a Fast Fourier Transformation<sup>10</sup> was performed on the respective time-dependent displacement signals of 20 s length with a sample rate of 0.001 s. The respective Power Spectral Densities<sup>11</sup> can be found within figures 2.12 (b), (c) and (d).

As one can see, var. I shows only one peak at the undamped system's eigenfrequency. The introduction of a non-linear system leads already to several superharmonic peaks for  $3 \cdot f_0$ ,  $6 \cdot f_0$  and so on. If viscous damping and a cosine excitation with a frequency of 1 Hz are added to the system, significantly more peaks can be found within the spectrum.

---

<sup>10</sup>FFT

<sup>11</sup>PSD

Table 2.5: Parameters and initial conditions for super- and subharmonic oscillation simulations of a force-excited single mass oscillator

parameter	var. I*	var. II*	var. III
mass $m$	1 kg	1 kg	1 kg
stiffness for zero displacement $c_0$	$39.478 \frac{\text{N}}{\text{m}}$	$39.478 \frac{\text{N}}{\text{m}}$	$39.478 \frac{\text{N}}{\text{m}}$
viscous damping $d$	–	–	$0.3 \frac{\text{Ns}}{\text{m}}$
excitation amplitude $ p $	–	–	100 N
excitation frequency $\Omega$	–	–	1 Hz
stiffness characteristics	linear	nonlinear	nonlinear
initial displacement $x_0$	1 m	1 m	1 m
initial velocity $\dot{x}_0$	$0 \frac{\text{m}}{\text{s}}$	$0 \frac{\text{m}}{\text{s}}$	$0 \frac{\text{m}}{\text{s}}$

(\*) Undamped natural oscillation was assumed.

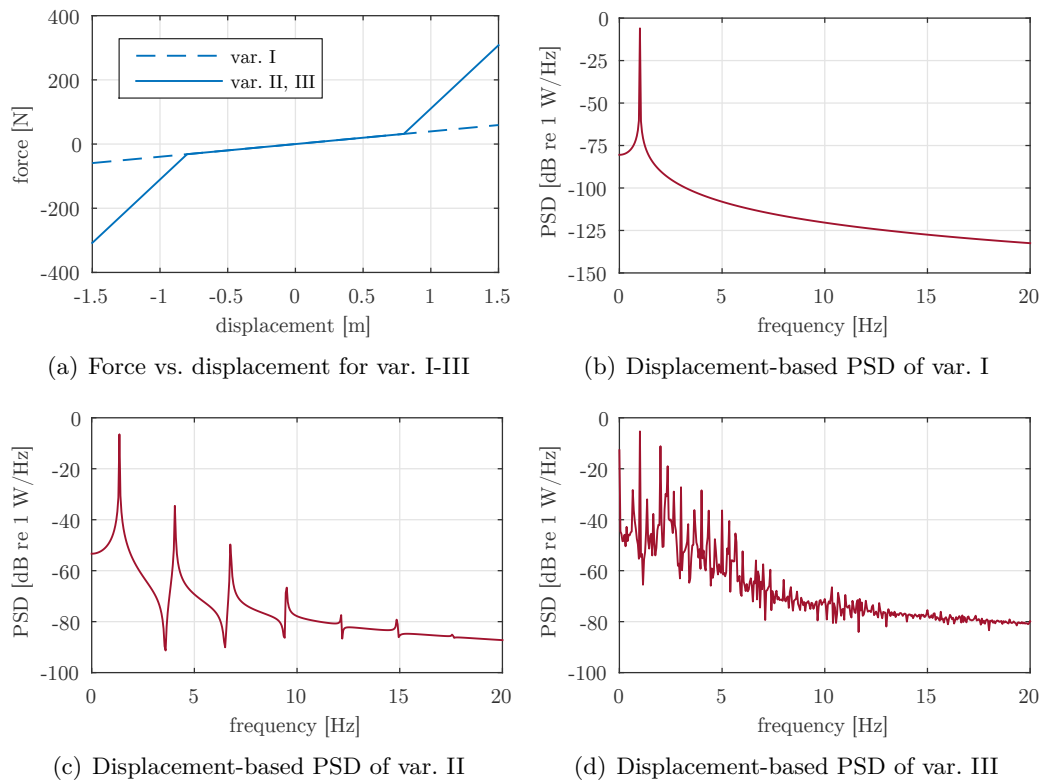


Figure 2.12: Explanatory diagrams of performed simulations of a non-linear force-excited single mass oscillator

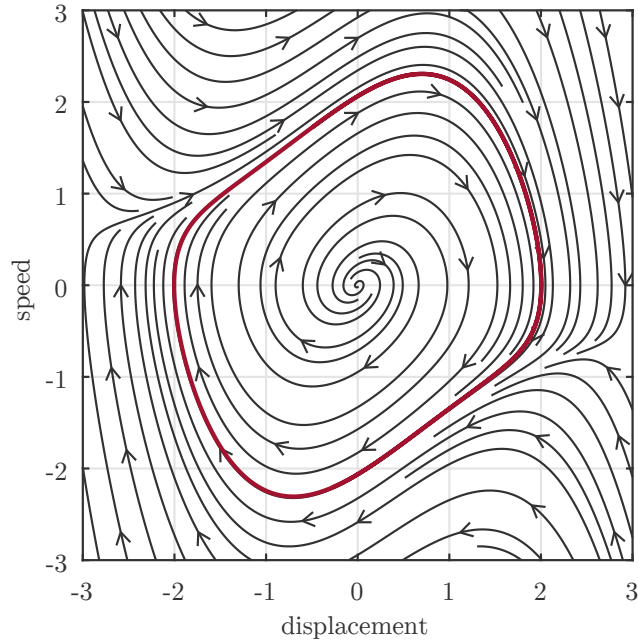


Figure 2.13: Phase diagram of the Van der Pol oscillator for  $\varepsilon = 0.6$

### 2.3.2 Limit Cycles

The term limit cycle relates to self-excited oscillations and describes a behavior which can be simply explained by the one-dimensional *Van der Pol* oscillator. Its equation of motion can be found in eq. 2.11.

$$\ddot{x} - \varepsilon(1 - x^2)\dot{x} + x = 0 \quad (2.11)$$

As one can see, this equation contains only one parameter. For  $\varepsilon = 0.6$ , a phase diagram is shown in fig. 2.13.

Streamlines, which are tangent to the gradient for any point within the plot, are drawn in order to display the principal behavior of the Van der Pol oscillator. Here, the red colored limit cycle divides the plot into two sub-areas: For initial conditions within this separator, amplitudes of speed and displacement increase whereas outside of it amplitudes fall. Both changes persist until limit cycle oscillation is reached.

Explanations for this behavior can be found in the equation of motion, eq. 2.11. Depending on the square of the displacement  $x$ , the coefficient of the speed dependent damping can change its sign. On one hand, small displacements  $x$  lead to a negative damping term, which means excitation of the system. Naturally, this includes that additional energy is brought into the system. On the other hand, larger

displacements lead to positive damping and a decrease of amplitudes. Therefore, any initial condition apart from a fixed point will eventually lead to an oscillation along the system's limit cycle.

These concepts are especially important for self-excited systems such as friction-induced oscillations in brake systems. Details can be found within chapter 2.4.

### 2.3.3 Bifurcations

Another common circumstance related to non-linear oscillations is the occurrence of bifurcations. According to [43], a bifurcation means a qualitative change of a system's structural behavior. This is the case, if the quantity and/or stability of fixed points or resulting oscillations changes for different system parameters.

This shall be explained by the example of the so-called *Hopf bifurcation*: For an exemplary system described in polar coordinates  $\{r, \theta\}$  as within eq. 2.12 and eq. 2.13, significantly different results can be found depending on parameter  $\kappa$ . As one can see e.g. within [28], this basic bifurcation type has also practical relevance in terms of friction-induced oscillations of brake systems: The behavior of brake squeal can be explained by this bifurcation type.

$$\dot{r} = \kappa r - r^3 \tag{2.12}$$

$$\dot{\theta} = 1 \tag{2.13}$$

For  $\kappa$  values smaller than zero, a stable fixed point with  $r = 0$  can be found, see the streamlines within the  $\{x, y\}$  phase plot in fig. 2.14 (a). An example solution for the initial condition  $\{x_0 = 0, y_0 = 0.5\}$  and a simulation time  $t_{\text{sim}} = 100$  s was performed in MATLAB and is depicted by the blue line.

Similarly, fig. 2.14 (b) shows the same streamlines and exemplary simulation for the bifurcation point  $\kappa = 0$ . Here, the former stable fixed point morphs into an unstable limit cycle oscillation. With higher positive parameters  $\kappa$ , the limits cycle's radius  $r$  increases according to  $r^2 = \kappa$ . An example with  $\kappa = 0.4$  can be seen in fig. 2.14 (c).

Introduction of the Hopf parameter  $\kappa$  as another dimension leads to the very demonstrative three-dimensional bifurcation diagram in fig. 2.14 (d), which clearly shows the different solutions and their dependence on the Hopf parameter  $\kappa$ , see also [20].

Certainly, the investigated system is of a rather simple structure: More complex systems often show many different bifurcations or even chaotic behavior.

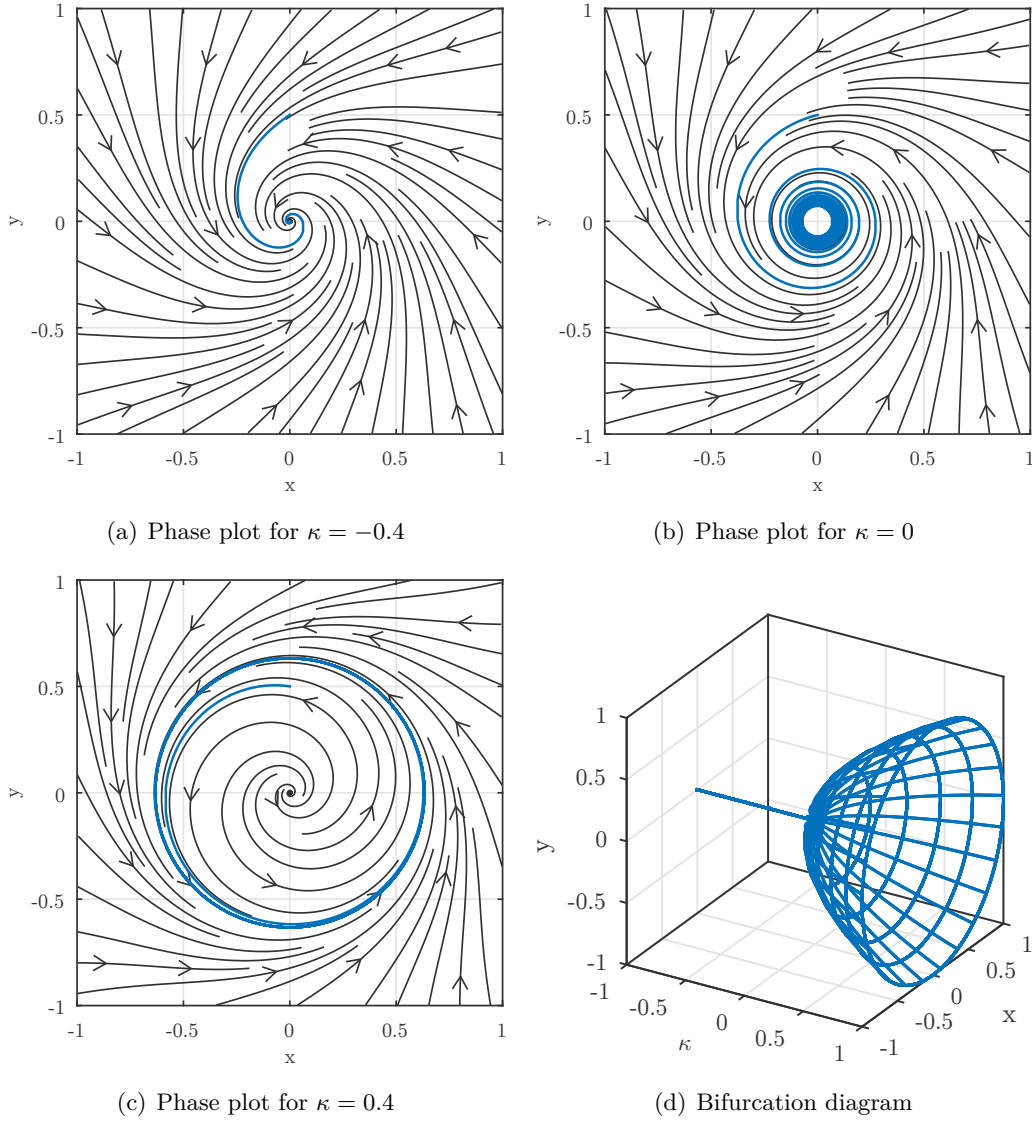


Figure 2.14: Characteristic plots of a Hopf bifurcation according to eq. 2.12 and eq. 2.13, based on [20]

### 2.3.4 Hartman–Grobman Theorem and Linearized Stability Analysis

According to the theorem of Hartman and Grobman, a nonlinear system's stability near a fixed point is identical with the according linearized system's stability about this fixed point. This holds only if the investigated fixed points are hyperbolic, which means that the corresponding eigenvalue has a real part different to zero. For non-hyperbolic fixed points, no conclusions in terms of stability can be drawn by an investigation of the linearized structure. [20], [30], [37]

As explained within [33], stability analyses are commonly performed for linearized systems, which is also related to limits of computational power. Based on the formerly presented example of the Hopf bifurcation within eq. 2.12 and eq. 2.13, which is elaborately explained within [20], the basic procedure for linearization shall be explained in the following.

By transforming the above mentioned system equations from polar coordinates  $\{r, \theta\}$  to Cartesian coordinates  $\{x, y\}$ , eq. 2.14 and eq. 2.15 result. The system's fixed point is found in  $\{x_0 = 0, y_0 = 0\}$  by setting both Cartesian velocities to zero.

$$\dot{x} = (\kappa - (x^2 + y^2)) \cdot x - y \quad (2.14)$$

$$\dot{y} = (\kappa - (x^2 + y^2)) \cdot y + x \quad (2.15)$$

Linearization of the system about its fixed point is executed by bringing the equations of motion into a form according to eq. 2.16.

$$\begin{aligned} \dot{\vec{x}} &= \mathbf{A} \cdot \vec{x} \\ &= \mathbf{J}|_{\vec{x}=\vec{x}_0} \cdot \vec{x} \\ &= \frac{\partial \dot{\vec{x}}}{\partial \vec{x}} \Big|_{\vec{x}=\vec{x}_0} \cdot \vec{x} \quad \text{with} \quad \vec{x} = \begin{bmatrix} x \\ y \end{bmatrix} \end{aligned} \quad (2.16)$$

The linearized system matrix  $\mathbf{A}$  for this special example can be found within eq. 2.17. By setting its determinant including an eigenvalue term to zero, the characteristic equation can be found according to eq. 2.18: Its solution leads to the two eigenvalues  $\lambda_{1,2}$ .

$$\mathbf{A} = \left[ \begin{array}{cc} \kappa - (3x^2 + y^2) & -1 - 2xy \\ 1 - 2xy & \kappa - (x^2 + 3y^2) \end{array} \right]_{\vec{x}=\vec{x}_0} = \begin{bmatrix} \kappa & -1 \\ 1 & \kappa \end{bmatrix} \quad (2.17)$$

$$0 \stackrel{!}{=} \det(\mathbf{A} - \lambda \mathbf{I}) = (\kappa - \lambda)^2 + 1 \quad \rightarrow \quad \lambda_{1,2} = \kappa \pm i \quad (2.18)$$

For a linearized system, these eigenvalues relate to the solution of the differential equations according to an exponential approach, see eq. 2.19 and 2.20. As the

real part of both eigenvalues  $\Re\{\lambda_{1,2}\}$  is always the Hopf parameter  $\kappa$ , these are hyperbolic for all values with  $\kappa \neq 0$ . Then, the Hartman-Grobman theorem can be applied.

$$x(t) = C_1 e^{\lambda_1 t} + C_2 e^{\lambda_2 t} \quad (2.19)$$

$$y(t) = C_3 e^{\lambda_1 t} + C_4 e^{\lambda_2 t} \quad (2.20)$$

For  $\kappa < 0$ , the linearized system's stability about  $\vec{x}_0$  results stable/damped whereas for  $\kappa > 0$ , unstable/excited behavior results. At  $\kappa = 0$ , Hartman-Grobman does not apply as the eigenvalue is non-hyperbolic here, the system's stability cannot be evaluated based on the linearized system.

A comparison with the phase plots of the non-linear system in fig. 2.14 (a) and (c) confirms the stability results of the linearized system in an infinitesimal neighbourhood of the fixed point  $\{x_0 = 0, y_0 = 0\}$ . Nevertheless, conclusions about the system's stability at clearly different displacements  $\{x, y\}$  cannot be drawn at all, see also [47]. This also includes the amplitude of an occurring limit cycle like in this example. Furthermore, in a non-linear oscillation, the linearized single harmonic solution is gradually complemented by higher harmonic contents with increasing distances to the fixed point, see [47].

Eventually, stability evaluation based on a linearized system is rather common in practical engineering applications: Hartman-Grobman's theorem is also the foundation of the investigated method of the Complex Eigenvalue Analysis.

## 2.4 Disk Brake Noise, Vibration and Harshness

### 2.4.1 Phenomenology

Several noise and vibration phenomena can be caused by the disk brake in combination with the suspension system of a passenger car. In fig. 2.15, an overview of possible brake-related vibration phenomena and their characteristic frequency range is depicted based on several literature resources and the author's personal perception.

As only self-excited, low-frequency noise and vibration were considered for this study, the focus is set on the phenomena creep groan and moan. Due to its probed behavior and established simulation methods, disk brake squeal is reviewed in a short manner too.

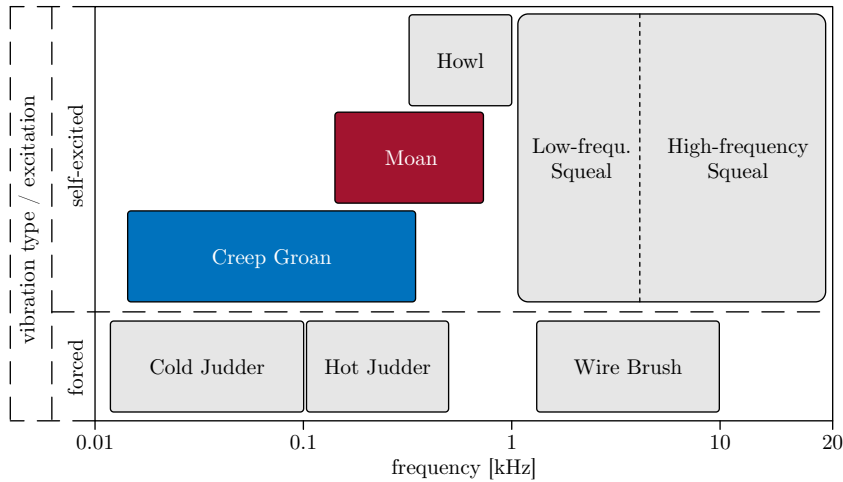


Figure 2.15: Classification of different disk brake NVH phenomena, adapted from [3], [7], [15], [56], [58]

#### 2.4.1.1 Creep Groan

With frequencies typically below 500 Hz, creep groan is considered as a self-excited brake noise phenomenon in the low-frequency range, [15], [52]. Today, most experts agree on the strongly non-linear stick-slip effect as causation for this NVH problem. [4], [38], [39], [44], [60]

Accordingly, creep groan oscillations consist of several, clearly distinguishable phases, as can be seen in [4], [9], [38], [44]:

At first, brake pads stick globally (this means: throughout their whole surface) on the brake disk. As a certain torque is provided to the brake disk, a wind-up action happens. This process can occur in different situations, e.g. for standstill in cars with automatic transmission or at inclined roads. Furthermore, passengers entering a car with engaged (rear) parking brake can also supply the necessary torque for originating creep groan vibrations, [10].

If brake pressure and the resulting tangential friction force become too low to resist the drive torque, e.g. when slowly releasing the brake pedal for set off, global slip between the pads and the disk occurs. Then, the friction force decreases abruptly according to the sliding coefficient of friction. Very similar to force excitation in form of a jump function, this stick-slip transition excites damped, natural oscillations especially of lower eigenfrequency, see [44]. When the pads stick on the disk again, the process starts anew with a wind-up action.

In the frequency spectrum, many super-harmonics with rather high peaks are characteristic, see e.g. [17], [51], [52]. This leads to a rather inharmonic signature of creep groan time signals, [52]. See also the frequency spectrum of pad accelerations measured during creep groan tests on a drum-driven suspension and brake test rig

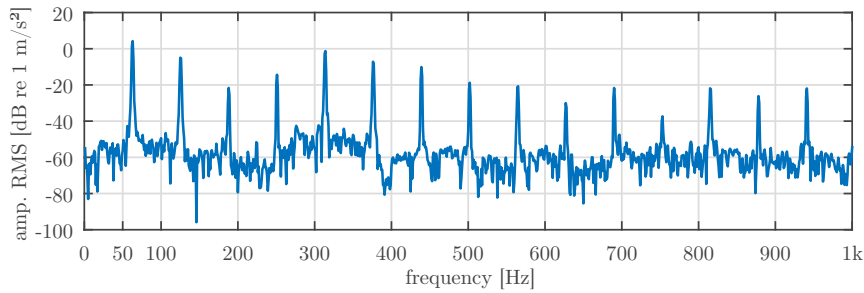


Figure 2.16: Characteristic frequency plot of pad acceleration in vehicle's x-direction during 63 Hz creep groan measured on a drum-driven suspension and brake test rig, adapted from [38]

according to fig. 2.16.

Regarding Operating Deflection Shape<sup>12</sup>, different statements can be found for different suspension configurations:

*MacPherson front axles:*

- [60] describes a creep groan ODS for 96 Hz basic frequency. A first order bending mode of the strut combined with a forward/backward movement of wheel carrier and lower control arm were found by this research group. Moreover, an upward/downward oscillation of the caliper can be seen, which could relate to rotational displacements of the caliper about the wheel axis. In addition, ODS of related higher harmonics with 190 Hz and 288 Hz are explained too.
- [39] shows a longitudinal movement of lower control arm and knuckle. However, the basic creep groan frequency is stated at approx. 18 Hz. The careful reader can identify first order bending of the strut in a depiction shown within this work.
- [27] explains a rotation of the wheel carrier and the brake caliper in combination with a first order bending mode of the strut at 100 Hz.

*Double wishbone front axles:*

- [25] shows ODS for two specific modes contained in a creep groan signal. At 25 Hz, mainly longitudinal movement of upper control arm, wheel carrier and floating caliper was found. At 41 Hz, the named parts performed a rotation about a lateral axis near the wheel axis.

---

<sup>12</sup>ODS

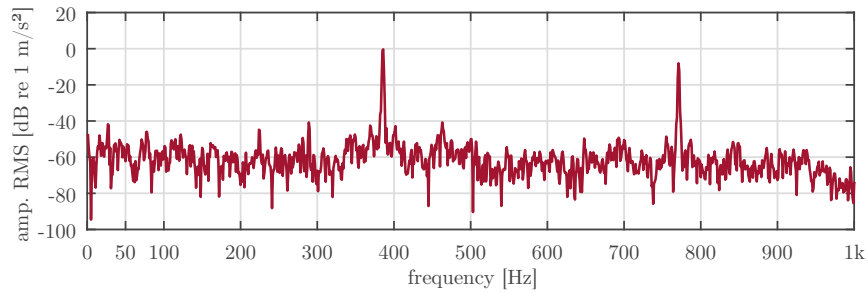


Figure 2.17: Characteristic frequency plot of pad acceleration in vehicle's x-direction during 386 Hz moan measured on a drum-driven suspension and brake test rig, adapted from [38]

#### 2.4.1.2 Moan

Similar to creep groan, brake moan is a low-frequency brake NVH phenomenon with frequencies below 1000 Hz. Actual frequency ranges found in literature were e.g. 100 – 500 Hz in [15], 500 – 1000 Hz in [28] or simply approx. 500 Hz in [45]. Based on the author's experience, most significant moan frequencies range from 350 – 600 Hz. Results of studies within [40], [42] and [45] support this statement. According to [6], frequency range alone is insufficient for describing a NVH phenomenon. Especially as many sources do not clearly distinguish frequencies of audible noise and measured component acceleration frequencies, it is more reliable and meaningful to distinguish excitation mechanisms.

For brake moan, different opinions still exist on this issue. In many early works like [17] or [59], but even in current studies, e.g. [40], moan is treated similar to creep groan and the stick-slip effect is claimed responsible for the occurrence of moan. On the other hand, [6] and [44] speak of moan as a sort of low-frequency brake squeal, caused by mode coupling. Within [38], the author's research group examined relative velocities between brake disk and pads during moan action, which additionally supports modal coupling as causation. Clearly, no near-zero relative speeds were found as the brake disk showed significantly higher speeds than the pads. Therefore, stick-slip in a global meaning – i.e. either only stick or only slip contact for every point of the whole lining surface – was considered unlikely. Similar statements were also made by [6].

Regarding their frequency spectrum, moan signals typically contain a distinct peak at the main frequency with super-harmonic parts of lower amplitude, see e.g. [6], [42] or a characteristic plot adapted from [38] within fig. 2.17. In the author's perception, the resulting sound can be described as rather tonal.

For ODS, different axle settings have to be distinguished again:

*Twist-beam rear axles:*

- [6] describes moan as a combination of caliper rotations about the vertical axis, the wheel axis and the vehicle's roll axis. Similar movements have been found in brake squeal measurements. In addition, oscillation coupling of left and right brake via the twist-beam was detected. By simulation, a bending mode, a torsion mode as well as an 'opening' mode of the twist-beam were found in the respective frequency range.

*Double wishbone front axles:*

- [45] found a characteristic torsional rim mode by the application of laser vibrometry. Additionally, simulation results showed strong displacement of both control arms, especially the upper control arm exhibited a characteristic 'opening' bending.

### 2.4.1.3 Squeal

In contrast to creep groan or moan, brake squeal has been in the focus of researchers earlier and more intensively, as indicated by the high number of associated studies. Basically, low-frequency squeal in the range of 1 – 3 kHz and high-frequency squeal in the range of 3 – 16 kHz can be distinguished, [15].

Similar to moan, stick-slip was made responsible for squeal in the early stages of research. Today, many experts agree on mode coupling in the context of a Hopf bifurcation as the origin of this NVH phenomenon, see e.g. [28]. According to this theory, two eigenmodes of the system – which relate to different sub components of the complete disk brake and suspension system – coalesce due to the friction forces between disk and pads. Typically, these modes are a disk mode with high out-of-plane displacements within the contact zone and a 90° phase-shifted pad eigenmode with high displacements in tangential direction. For coupling, both modes need to be of a similar eigenfrequency – therefore, separation of modes is a common countermeasure during the design process. Naturally, damping e.g. via additional damping shims can reduce limit cycle amplitudes and prevent the occurrence of audible noise. [2], [44], [58]

In the frequency spectrum, squeal vibrations show a distinct peak at their dominant frequency in the low kHz range, harmonics are possible but usually of lower oscillation energy, [58].

As explained above, a disk and a pad mode are necessary for squeal-related modal coupling. Therefore, these parts are typically the main focus of squeal-related ODS analyses, see e.g. [58]. Moreover, components of high influence are usually parts rather 'near' to the brake force generation such as e.g. the knuckle or the caliper, which is used for optimization in [14]. In the author's opinion, suspension components like strut or the control arms have less influence on this phenomenon.

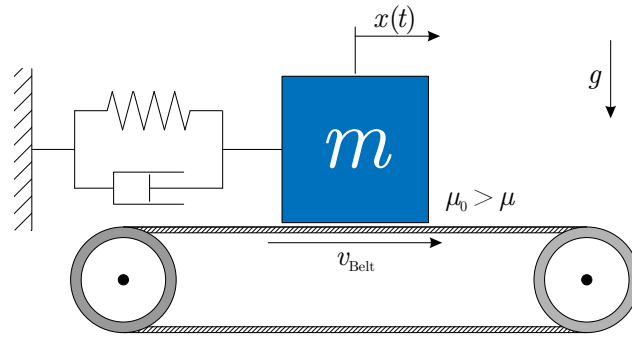


Figure 2.18: 1D mass-on-belt model for physical instabilities, adapted from [44]

### 2.4.2 Explanation Models

All three named phenomena represent a form of self-excited, friction-induced vibration. Typically, these arise due to the existence of a certain type of instability. Based on [44], the following categories can be found:

- physical instability
- dynamic instability
- geometric instability

In chapter 2.4.1, two different excitation mechanisms for self-excited brake NVH phenomena were stated: Stick-slip effect and modal coupling.

On the one hand, the *stick-slip effect* arises due to a difference between static coefficient of friction and sliding coefficient of friction:  $\mu_0 > \mu$ . Result can be an abrupt change of friction forces which leads to the excitation of oscillations. Certainly, these contain characteristic stick as well as slip phases. This effect represents a physical instability and is highly dependent on parameters like brake pressure or relative speed, [6]. Moreover, instabilities caused by speed-dependent friction coefficients are also classified as physical instabilities. [44]

The classical 1D mass-on-belt model is one of the simplest and most common models able to perform stick-slip oscillations, see fig. 2.18. Here, a mass pressed on a belt moving with constant speed exhibits self-excited oscillations about its static displacement caused by a (necessary) difference in static and sliding coefficient of friction. [44]

On the other hand, *modal coupling* acts as a dynamic instability. Here, two modes of similar eigenfrequency coalesce, see also chapter 2.4.1.3. A stability analysis according to the example within chapter 2.3.4 explains the basic stability tendencies of the two eigenmodes: With increasing coupling, one of the eigenvalues becomes more stable (decreasing real part) whereas the other one becomes more and more unstable (increasing real part). As the coefficient of friction determines tangential

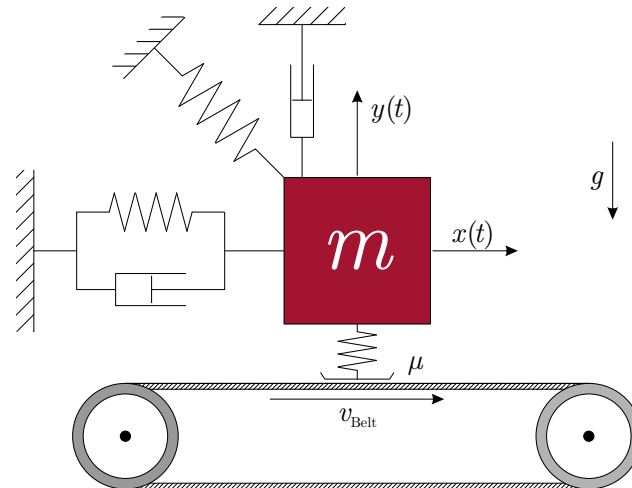


Figure 2.19: 2D mass-on-belt model for dynamic instabilities, adapted from [44]

coupling between disk and pad linings in a disk brake system, modal coupling is typically favored by higher coefficients of friction. [12], [44]

For a dynamic instability like this, the most simple model must already possess two Degrees Of Freedom<sup>13</sup> in order to oscillate in two different modes, see fig. 2.19. Nevertheless, static and sliding coefficient of friction can be identical here as they are not necessary for the occurrence of an instability. If  $\mu_0 > \mu$  anyway and damping is very low, the stick-slip effect limits growth of oscillation amplitudes when the belt speed is reached. Hence, oscillations containing discrete stick and slip phases can be reached even with an excitation different from the stick-slip effect. [44]

The third explanation model, geometric instability or the so-called sprag-slip effect, is related to a variation of normal force with other corresponding brake-NVH phenomena like e.g. dynamic groan. As this is not of relevance for this work, it is not considered further.

## 2.5 Complex Eigenvalue Analysis for Disk Brake Squeal

Based on [28], [49] and very similar to the author's work in [38], the mathematical background and important equations of the CEA in terms of its application for disk brake squeal are presented here. All statements are based on the procedure of the FE-solver PERMAS, as it was used for performed simulations presented in the following chapters.

The main idea of CEA is based on the *Hartman-Grobman theorem* stated in section 2.3.4: A stability analysis of the linearized brake system with its non-linear friction

<sup>13</sup>DOF

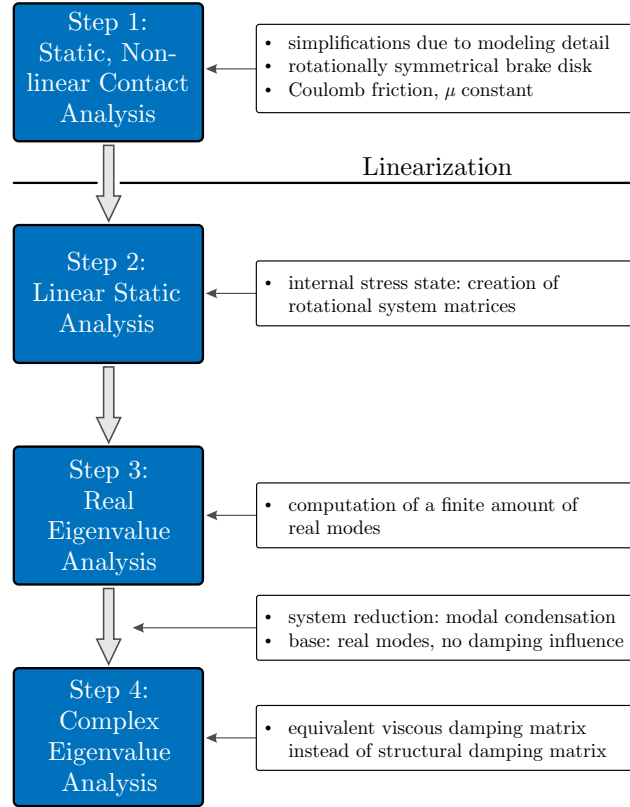


Figure 2.20: CEA for disk brake squeal: procedure and essential simplifications, adapted from [38]

behavior is performed in a fixed point of the system. As long as the investigated fixed points are hyperbolic (non-zero real part), stability near these fixed points is identical for both linearized and non-linear system.

Basically, this leads to the solution of an equation with the main structure according to eq. 2.21. In order to build up this equation, several intermediate steps and simplifications are necessary – see an overview within fig. 2.20. This process basically shifts the difficulty of the task from numerical solution to the build-up of the modal model. [57]

$$\begin{aligned}
 \vec{0} = & \widetilde{\mathbf{M}} \cdot \ddot{\vec{q}} + \\
 & \left[ \widetilde{\mathbf{D}}_V + \widetilde{\mathbf{D}}_{Ct}(\Omega) + \widetilde{\mathbf{D}}_G(\Omega) + \widetilde{\mathbf{D}}_{eqv} \right] \cdot \dot{\vec{q}} + \\
 & \left[ \widetilde{\mathbf{K}}_{el} + \widetilde{\mathbf{K}}_{Ct} + \widetilde{\mathbf{K}}_G(\Omega) + \widetilde{\mathbf{K}}_C(\Omega) \right] \cdot \vec{q}
 \end{aligned} \tag{2.21}$$

First of all, the fixed point itself needs to be found: This is done by a static analysis of the non-linear system. Naturally, high error can be created already at this early

stage by insufficient modeling e.g. of elastomer bushings' stiffness and damping characteristics. Assumptions regarding the contact state further falsify the result.

In a next step, the system needs to be linearized. Here, probably the biggest and most crucial simplifications of this approach are taken: Highly non-linear friction behavior, typically based on the simple Coulomb friction model, is treated linearly based on a Taylor series approximation. This strongly distorts the contact's characteristics: Normal separation is not possible anymore, tangential forces are represented by additional stiffness and damping terms.

For a decrease of computational costs, a model reduction based on undamped real modes is typically performed subsequently. Eventually, the Ordinary Differential Equation<sup>14</sup> within eq. 2.21 results: Here, a complex approach is taken. In contrast to the simpler Real Eigenvalue Analysis<sup>15</sup>, modes – the eigenvectors of a system – and the eigenvalues themselves can both contain complex numbers here. This enables the inclusion of damping effects, which typically play an important role for stability.

Another crucial factor for stability is the existence of asymmetric stiffness terms caused by the frictional contact – see e.g. [55]. These terms can lead to the negatively damped eigenvalues sought, meaning an instability with possibly high limit cycle amplitudes due to modal coupling. Therefore, the so-called equivalent viscous damping ratio is evaluated: Negative values indicate a negatively damped – and therefore excited – eigenmode.

Within industrial application of the CEA, such as a standard brake squeal investigation, this crucial factor is also used as optimization parameter, see [14]. However, this practice has the big disadvantage of over- and under-prediction due to the CEA's validity only near the fixed point. As already stated in section 2.3.4, no conclusions can be drawn about the actual amplitudes and the resulting noise. Still, this method allows for efficient computation and simple treatment of different variants and parameter changes due to its linearized principle.

In the following, all necessary steps for a CEA according to fig. 2.20 are described thoroughly based on [28], [49], which can be found in similar manner in the author's work in [38].

### 2.5.1 Step 1: Static, Non-Linear Contact Analysis

Firstly, the contact state is evaluated in a static, non-linear simulation. *Simplifications due to modeling detail* are already introduced in this step. Especially parts of lower squeal-influence such as the spring with damper assembly or elastomer bushing stiffnesses are usually represented in a strongly simplified manner. Nevertheless,

---

<sup>14</sup>ODE

<sup>15</sup>REA

the influence of such parts can be significant as can be seen in chapter 4 or in [38]. Subsequent to this first step, the *linearization of bushing stiffnesses* is executed.

The respective brake pressure within the caliper's fluid channels as well as inertia forces caused by the rotating brake disk, which is simplified to be *rotationally symmetrical*, are applied on the system. In addition, a reference relative speed between brake disk and pad linings needs to be defined in order to determine the contact state – stick, slip or separation – in every node of contact. Result is the static rest position, or, using the terminology of chapter 2.3.4, the fixed point,  $\vec{x}_0$ . In the following, all computations are only calculated for small deviations  $\Delta\vec{x}(t)$  about this static rest position, see eq. 2.22.

$$\Delta\vec{x}(t) = \vec{x}(t) - \vec{x}_0 \quad (2.22)$$

Subsequently, essential matrices based on the contact state are created:

- For normal contact forces, which depend on  $\Delta\vec{x}(t)$ , Multi Point Constraints<sup>16</sup> couple the contact partners in each participating node by directly ‘locking’ the respective DOFs.
- For tangential contact forces, a friction force based on the rather simple *Coulomb friction* is calculated. Due to the reference speed given, all contact nodes are assumed to slip – a tangential friction force according to eq. 2.23 results. As one can see, this vector quantity depends on displacement deviations  $\Delta\vec{x}(t)$  in  $\vec{f}_N$  as well as on speed deviations  $\Delta\dot{\vec{x}}$ .

$$\vec{f}_R = -\mu \|\vec{f}_N(\Delta\vec{x})\| \frac{\vec{v}_{\text{rel}}}{\|\vec{v}_{\text{rel}}\|} \quad (2.23)$$

Therefore, a *linear, first-order Taylor series approximation* can be applied on both normal contact force and tangential friction force as within eq. 2.24 and eq. 2.25. Details are stated in [28], [34].

$$\vec{f}_N(\Delta\vec{x}) \cong \left. \frac{\partial \vec{f}_N(\Delta\vec{x})}{\partial \Delta\vec{x}} \right|_{\Delta\vec{x}=\vec{0}} \cdot \Delta\vec{x} \quad (2.24)$$

$$\vec{f}_R(\Delta\vec{x}, \Delta\dot{\vec{x}}) \cong \left. \frac{\partial \vec{f}_R(\Delta\vec{x}, \Delta\dot{\vec{x}})}{\partial \Delta\vec{x}} \right|_{\Delta\vec{x}=\Delta\dot{\vec{x}}=\vec{0}} \cdot \Delta\vec{x} + \left. \frac{\partial \vec{f}_R(\Delta\vec{x}, \Delta\dot{\vec{x}})}{\partial \Delta\dot{\vec{x}}} \right|_{\Delta\vec{x}=\Delta\dot{\vec{x}}=\vec{0}} \cdot \Delta\dot{\vec{x}} \quad (2.25)$$

Both approximations contain partial differentials, which contribute to special contact-based matrices built for CEA. The partial differential with respect to speed deviations  $\Delta\dot{\vec{x}}$  in eq. 2.25 affects the speed-dependent rotational damping matrix  $\mathbf{D}_{\text{Ct}}(\Omega)$

---

<sup>16</sup>MPCs

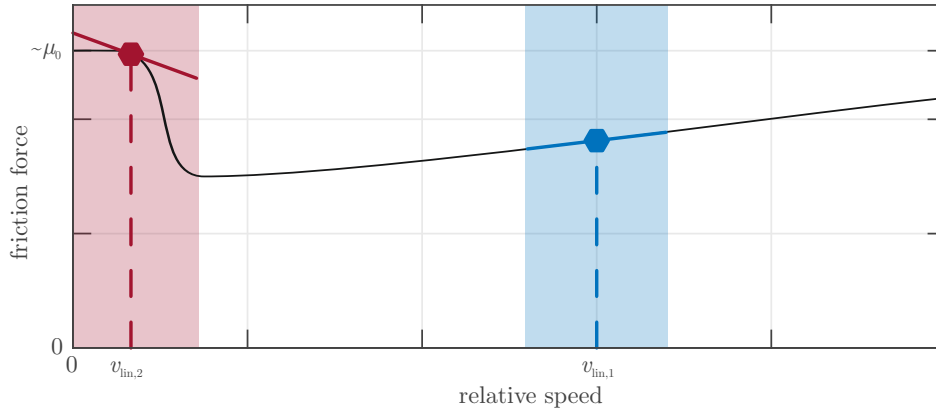


Figure 2.21: Influence of relative speed on the quality of friction force linearization, adapted from [38]

– describing viscous damping due to friction in radial disk direction. By contrast, partial differentials with respect to displacement deviations  $\Delta \vec{x}$  of eq. 2.24 and eq. 2.25 both affect the asymmetric, circulatory contact stiffness matrix  $\mathbf{K}_{\text{Ct}}$ . As already stated before, these terms are highly connected with the occurrence of unstable modes: For a positive semi-definite damping matrix, instabilities can only result when asymmetric stiffness terms exist.

Currently, influences due to a possible speed-dependency of the coefficient of friction can not be implemented by the used FE-solver, [49]. Nevertheless, improvement is possible by considering one or more additional Taylor terms, as already implemented by other software packages.

A rather simple depiction of the performed friction force linearization is given in fig. 2.21. For this schematic representation, uni-directional relative speed is assumed in combination with a classical Stribeck friction curve. On the one hand, linearization at  $v_{\text{lin},1}$  should lead to appropriate results, as friction forces can be approximated well by a linear speed-dependency. For the special case of Coulomb friction, which does not contain a speed dependency at all, linearization delivers an optimal result. On the other hand, linearization at  $v_{\text{lin},2}$  cannot describe the frictional behavior properly: Near zero relative speed, high changes of the coefficient of friction can be expected. Therefore, stick-slip oscillations are not possible in the case of a linearized mechanical system.

### 2.5.2 Step 2: Linear Static Analysis

Subsequent to the first step, the geometric and gyroscopic matrices are generated in the linear static analysis of the 2<sup>nd</sup> step. A simplified contact status is already used here. Moreover, effects caused by a non-rotationally symmetric brake disk are typically neglected – these would lead to periodically changing stiffness, mass and

damping matrices.

By applying inertia forces, a stationary stress state and the resulting geometric stiffness matrix  $\mathbf{K}_G$  can be computed. What is more, speed vectors change within one element for a rotating structure such as the brake disk. This influence is taken into account by calculating and implementing the convective stiffness matrix  $\mathbf{K}_C$ . Both additional stiffness matrices depend on the rotational speed  $\Omega$  in a quadratic manner, thus their importance increases significantly with higher rotational speeds.

Gyroscopic influences, depending linearly on rotational speed  $\Omega$ , are included by the calculation of the anti-metric gyroscopic matrix  $\mathbf{D}_G$ . Its build-up is performed by varying the rotational inertia forces with respect to both speed deviation  $\Delta\dot{\vec{x}}$  and displacement deviation  $\Delta\vec{x}$ . Gyroscopic effects can essentially affect the stability behavior, as brake squeal investigations within [34] have shown.

### 2.5.3 Step 3: Real Eigenvalue Analysis

As computation time is critical for industrial applications, a reduction of the problem size is desirable. Typically, this goal is reached by a modal condensation based on real modes.

In the 3<sup>rd</sup> step these real modes are calculated. Starting from the complete dynamic equilibrium equation in eq. 2.26, all system matrices except for the mass matrix  $\mathbf{M}$  and the elastic stiffness matrix  $\mathbf{K}_{el}$  are neglected therefore.

$$\begin{aligned} \vec{0} = & \mathbf{M} \cdot \Delta\ddot{\vec{x}}(t) + \\ & [\mathbf{D}_V + \mathbf{D}_{Ct}(\Omega) + \mathbf{D}_G(\Omega)] \cdot \Delta\dot{\vec{x}}(t) + \\ & [\mathbf{K}_{el} + \mathbf{K}_{Ct} + \mathbf{K}_G(\Omega) + \mathbf{K}_C(\Omega) + \mathbf{iH}] \cdot \Delta\vec{x}(t) \end{aligned} \quad (2.26)$$

For the solution of this second-order ODE, a classical exponential approach – see eq. 2.27 and the corresponding deviations in eq. 2.28 and eq. 2.29 – is taken.

$$\Delta\vec{x}(t) = \vec{\phi} \cdot e^{i\omega t} \quad (2.27)$$

$$\Delta\dot{\vec{x}}(t) = i\omega \vec{\phi} \cdot e^{i\omega t} \quad (2.28)$$

$$\Delta\ddot{\vec{x}}(t) = -\omega^2 \vec{\phi} \cdot e^{i\omega t} \quad (2.29)$$

Substitution of these terms in the simplified, time-dependent ODE results in eq. 2.30. In order to find the non-trivial solution ( $\vec{\phi} \neq \vec{0}$ ), the bracketed terms need to become  $\vec{0}$ . Therefore, eq. 2.31 has to be solved.

$$[\mathbf{K}_{el} - \omega^2 \mathbf{M}] \cdot \vec{\phi} = \vec{0} \quad (2.30)$$

$$\mathbf{K}_{\text{el}} - \omega^2 \mathbf{M} = \vec{0} \quad (2.31)$$

Due to the orthogonality of the computed eigenvectors  $\vec{\phi}$ , a new basis can be built by concatenating them to the modal matrix, see eq. 2.32.

$$\Phi = [\vec{\phi}_1, \vec{\phi}_2, \dots, \vec{\phi}_n] \quad (2.32)$$

In the following, these real eigenmodes can be utilized for the reduction of the complete dynamic equation in eq. 2.26, which includes all damping and stiffness effects. The introduction of modal coordinates  $\vec{q}(t)$  according to eq. 2.33 and a left multiplication with the transposed modal matrix  $\Phi^T$  leads to this desired modal condensation of the full system, see eq. 2.34.

$$\vec{x}(t) = \Phi \cdot \vec{q}(t) \quad (2.33)$$

$$\underbrace{[\Phi^T \mathbf{M} \Phi]}_{\tilde{M}} \cdot \ddot{\vec{q}} + \underbrace{[\Phi^T \Sigma \mathbf{D}_i \Phi]}_{\tilde{D}} \cdot \dot{\vec{q}} + \underbrace{[\Phi^T \Sigma \mathbf{K}_i \Phi]}_{\tilde{K}} \cdot \vec{q} = \vec{0} \quad (2.34)$$

This procedure reduces the large-scale system into a smaller-scale subspace, defined by the modal matrix  $\Phi$ . On the one hand, this brings the desired advantage of a smaller system, which can be computed in less time. On the other hand, the system's displacement possibilities are reduced by this measure due to two reasons:

1. In contrast to the complex eigenvectors explained in the next chapter, real eigenvectors are purely real. Thus, every single part of the system reaches its peak amplitude at the same time: Everything is in phase within one real eigenvector. See also fig. 2.22 (a).
2. Only a *finite amount of real modes* is calculated. By consideration of the Nyquist-Shannon sampling theorem, real modes have to be computed up to a frequency at least twice the frequency of interest. The influence of eigenmodes with higher frequency is neglected.

In addition to these findings, condensation based on real modes can alter a system's stability behavior significantly, even if an upper frequency limit presumably large enough was used. In order to improve the accuracy of CEA stability analyses, enhanced Proper Orthogonal Decomposition<sup>17</sup> approaches can be seen in [29] and [53].

Nevertheless, modal condensation is widely established in FE packages for CEA, also because of another benefit: The modal matrix  $\Phi$  does not change for differing rotational velocities, as real modes do not depend on this parameter. This enables fast sampling for different operational parameters, see e.g. [14].

---

<sup>17</sup>POD

### 2.5.4 Step 4: Complex Eigenvalue Analysis

The actual CEA itself is carried out in the last step of this procedure. Before, the structural damping matrix is replaced by an *equivalent viscous damping matrix* – see eq. 2.35. This PERMAS-specific action is necessary in order to supply completely real system matrices. Small errors result in case of frequencies differing from the reference frequency  $f_{H,\text{ref}}$ .

$$\tilde{\mathbf{D}}_{\text{eqv}} = \frac{1}{2\pi f_{H,\text{ref}}} \tilde{\mathbf{H}} \quad (2.35)$$

Similar to the real eigenvalue analysis, an exponential approach is taken for the modal displacement  $\vec{q}$ . However, complex numbers within eigenvalues and -vectors are possible here, see eq. 2.36.

$$\begin{aligned} \vec{q} &= \vec{\phi}_c \cdot e^{(\delta+i\omega)t} \\ &= \vec{\phi}_c \cdot e^{\delta t} \cdot (\cos(\omega t) + i \sin(\omega t)) \end{aligned} \quad (2.36)$$

In detail, this approach provokes the separation of displacement and time information in complex eigenvector and complex eigenmodes. As complex eigenvectors can contain an imaginary part, different phases within one eigenvector are possible. If only purely modal damping is implemented, all modes reach their peaks at the same time but differently phased to a real mode – compare fig. 2.22 (a) and (b). For local, nodal damping e.g. by discrete viscous elements or by additional damping terms due to contact linearization, different nodes can reach their peaks at different times within one complex mode, see eq. 2.37 and fig. 2.22 (c).

Furthermore, real modes are used as a new basis in this case. Therefore, each complex eigenvector can be thought as a superposition of differently-phased parts of real eigenmodes.

$$\vec{\phi}_{c,i} = \Re\{\vec{\phi}_{c,i}\} + i \Im\{\vec{\phi}_{c,i}\} \quad (2.37)$$

Substitution of the modal coordinate  $\vec{q}$  from eq. 2.36 with its time-deviations within the condensed equation of motion leads to eq. 2.38. Eventually, a transformation of this ODE into state space is the last step before the numerical solution for complex eigenvalues can be performed.

$$\begin{aligned} \vec{0} &= \tilde{\mathbf{M}} \cdot \ddot{\vec{q}} + \\ &\quad \left[ \tilde{\mathbf{D}}_V + \tilde{\mathbf{D}}_{\text{Ct}}(\Omega) + \tilde{\mathbf{D}}_G(\Omega) + \tilde{\mathbf{D}}_{\text{eqv}} \right] \cdot \dot{\vec{q}} + \\ &\quad \left[ \tilde{\mathbf{K}}_{\text{el}} + \tilde{\mathbf{K}}_{\text{Ct}} + \tilde{\mathbf{K}}_G(\Omega) + \tilde{\mathbf{K}}_C(\Omega) \right] \cdot \vec{q} \end{aligned} \quad (2.38)$$

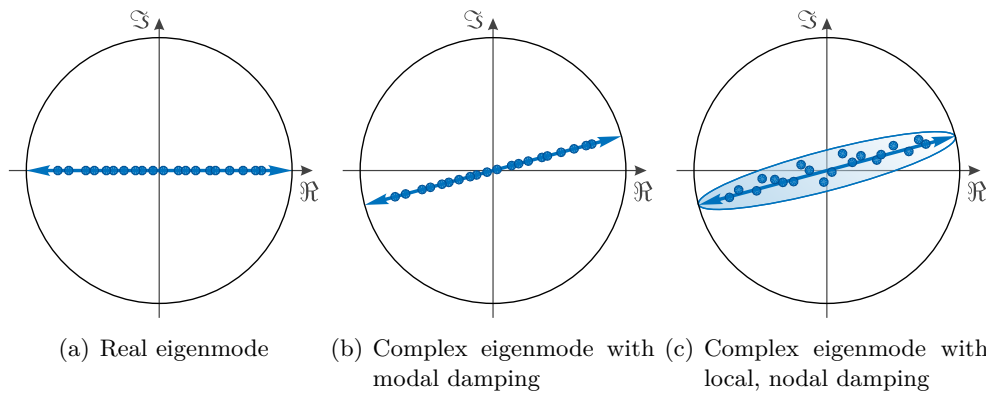


Figure 2.22: Influence of different damping models on real and imaginary part of nodal displacement amplitudes within one mode, adapted from [23]

In terms of stability behavior, resulting complex eigenvalues need to be investigated. Therefore, the equivalent viscous damping ratio is examined. According to eq. 2.39, this parameter informs about the complex eigenvalue's real part: For a negative equivalent viscous damping ratio  $\xi_i$ , the real part is positive. This relates to negative damping behavior enabling exponential growth of oscillation amplitudes, see also eq. 2.36. The respective complex eigenmode is considered unstable.

$$\xi_i = \frac{-\delta_i}{\delta_i^2 + \omega_i^2} \quad (2.39)$$

Typically, CEA results are found over-critical when compared to real life squeal occurrence in industrial applications. This is a result of the tools' incapability of a calculation of limit cycle amplitudes, which would relate to sound and vibration intensity - see also chapter 2.3.4. Nevertheless, enhanced criteria are currently under research, see e.g. [11].

### 2.5.5 Application Limits of CEA

In the author's work [38], limits of CEA application for the low-frequency disk brake NVH phenomena creep groan and moan were treated. The following simplifications were considered critical:

- linearization of Coulomb friction forces
- linearization of bushing stiffnesses

Whereas the linearization of bushing stiffnesses was considered important but nevertheless manageable, linearization of friction forces was considered to be a hard limit due to their high non-linearities near zero relative speed, [38]. Especially for

creep groan, this is crucial, as stick-slip oscillations are stated to be the cause of this phenomenon – see chapter 2.4.1.1. Therefore, the following applicability limit can be found:

A Complex Eigenvalue Analysis regarding brake noise phenomena can only lead to meaningful results, if the friction forces between brake pads and disk can be approximately linearized. For Coulomb friction, this is exclusively the case, if the direction of tangential relative velocity does not change within one oscillation or repetition cycle and global stick phases never occur. [38, p. 5]

In this context, CEA can only simulate the behavior during creep groans' slip phases. Here, a linearization according to section 2.5.1 is meaningful for the occurring damped natural oscillations. Certainly, investigation of the basic stick-slip frequency is not possible by this linearized approach. By contrast, CEA simulations for moan were claimed to be overall meaningful. Together with the shown importance of elastomer bushing stiffnesses, this knowledge was included for the simulative work presented in chapter 3.

---

## 3 Methodology

This chapter describes the approach towards the examination of CEA application regarding low-frequency brake NVH on a full vehicle front corner. At first, performed model variations based on a standard brake squeal FE-model are explained in chapter 3.1. In the following, further details about models and the used system matrices within PERMAS are investigated in section 3.2.

### 3.1 CEA Application on a Full-Scale Corner Model

For the simulative part of this work, an existing FE-model used for brake squeal analysis in an industrial application was basis for low-frequency CEA application on several different variants. Again, this work's close relation to [38] should be mentioned.

#### 3.1.1 Model Variants and Parameters

A passenger vehicle's front corner was under investigation. The original brake-squeal FE-model contained a fixed caliper brake system, the double wishbone axle including all steering arms, wheel carrier, stabilizer, the spring with damper assembly and the steering arm as well as spring and damper elements representing the rubber bushing's behavior.

In order to introduce the wheel's influence on creep groan and moan phenomena, a 3D-modeled rim and a simple tire representation were added. This tire model consisted of a 3D elastic spring element, connected on one node to the rim with a rigid MPC and connected to ground in the wheel contact point. Tire inertia was represented by nodal mass elements, separately connected to the rim via MPCs. High care was taken to model the tire's mass moment of inertia about the wheel axis correctly. A swing experiment and weighing of the inflated tire and rim delivered an accurate value, which was implemented by adapting the mass elements' radial distance.

For CEA, the stabilizer was removed from the model, as corresponding experimental tests for validation regarding creep groan and moan were performed without this component too. In fig. 3.1, components of the FE-model are depicted with a transparent rim for better visibility. ISO standard is used for this and all following

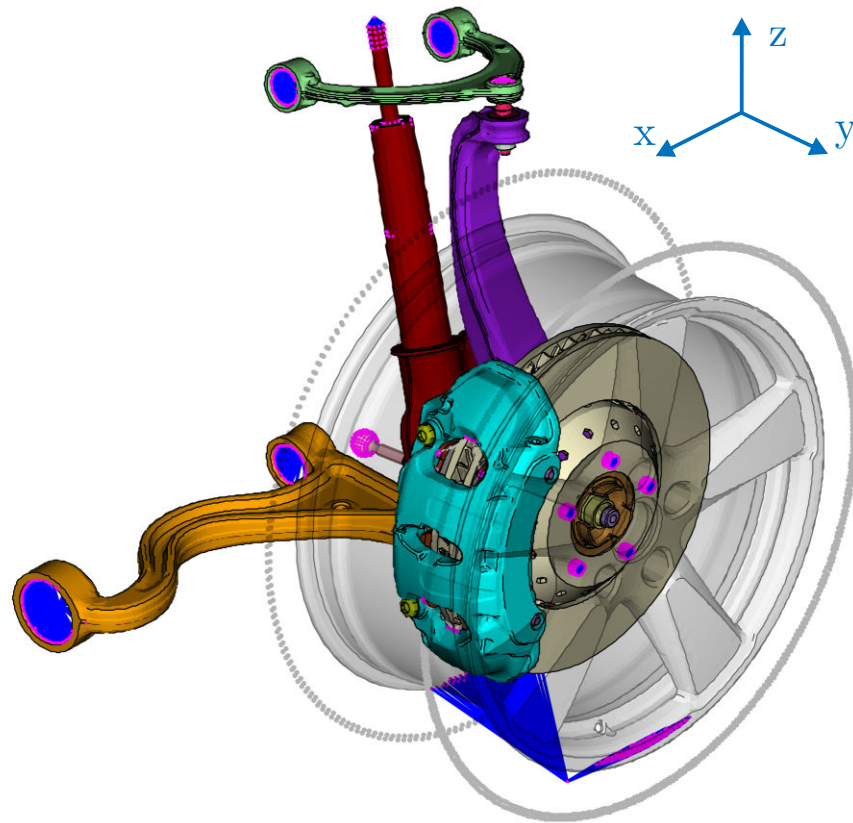


Figure 3.1: Adapted model for creep groan and moan CEA simulation with rim A

coordinate systems. For subsequently explained variants based on this model and rim design the overall number of nodes was about 690 000.

As for this current axle configuration a second rim was known to be prone for moan, one variant was simulated with this rim – rim B – instead of the standard rim A. In fig. 3.2 one can recognize the rather slim spoke design of rim B, which is identical to the moan-prone rim in the related work [38]. Due to a finer rim mesh, an overall number of approx. 1 000 000 DOFs were simulated with this model.

In both cases, model support was introduced in all DOFs at the rubber bushings of both lower and upper control arm as well as at the spring with damper assembly's upper connection point to the vehicle body. Additionally, the steering link was fixed translational and in one torsional/rotational DOF. The wheel contact point, connected to the tire's spring element, was constrained translational as well. See fig. 3.3 for a depiction.

For the evaluation of various parameter and component influences, eight different variants were simulated. The first six refer directly to the six variants in the author's work [38] whereas the last two were computed and evaluated exclusively for this

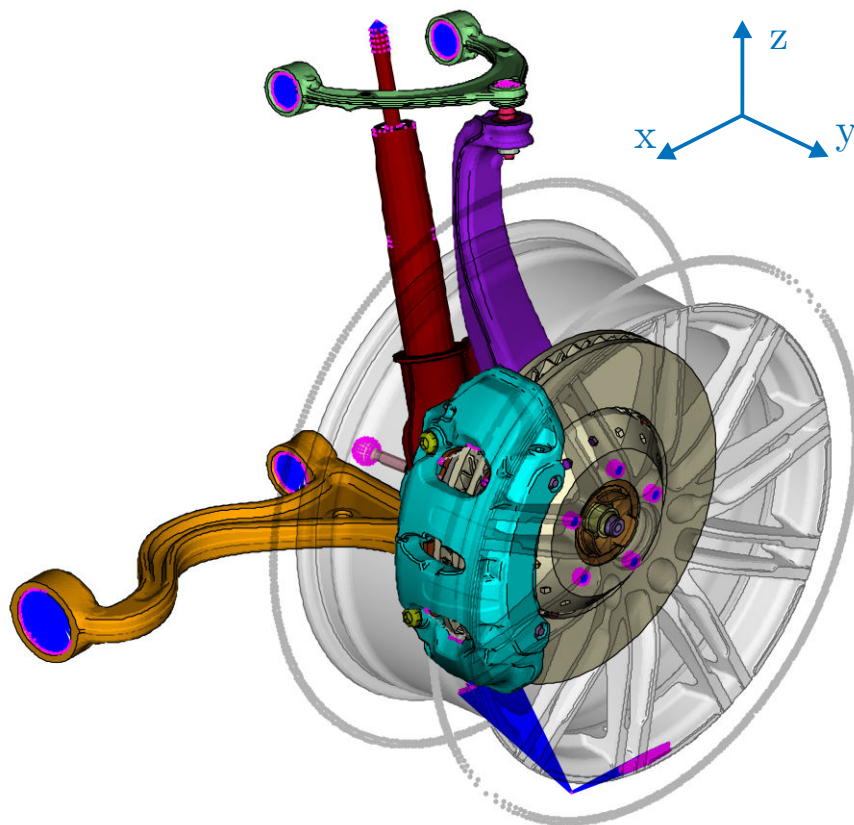


Figure 3.2: Adapted model for creep groan and moan CEA simulation with rim B

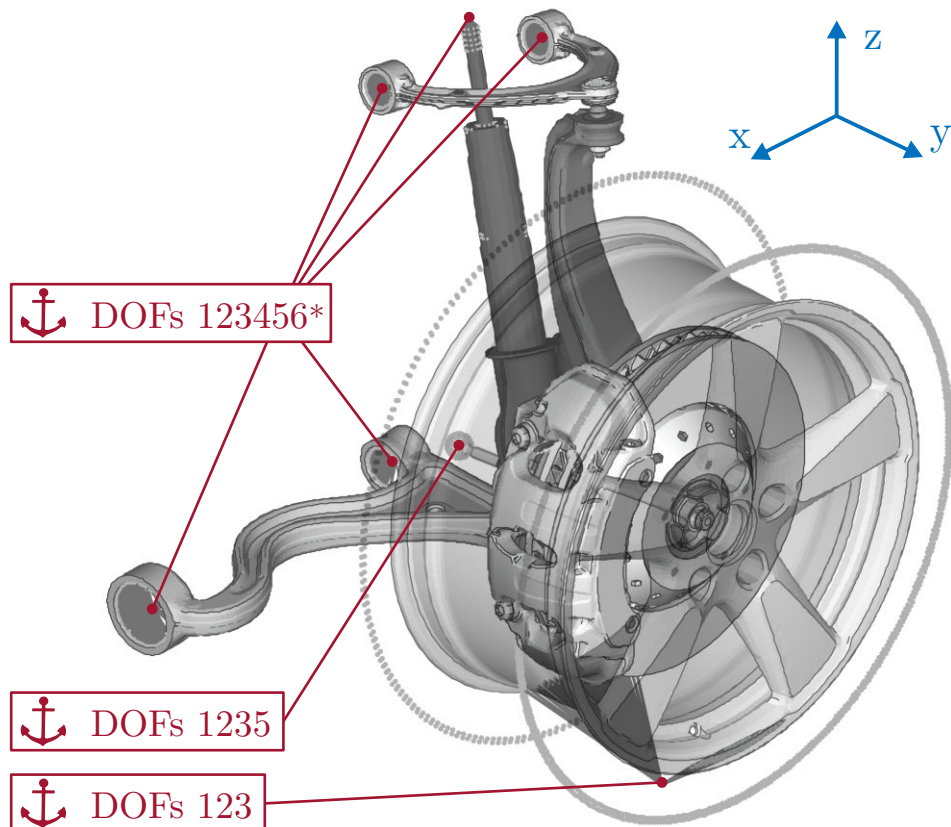
work. In table 3.1, a model variant overview is given.

*Variant 1 - Squeal-Model* represents the original industrial squeal model, complemented by the wheel model mentioned above.

At first, some components' geometry and material specifications had to be updated in accordance to the used test setup in [38]. This led to *variant 2 - Corrected Geometry*. Modified components were the brake disk, the lower control arm and the brake caliper with pistons. Additionally, elastomer bushing stiffnesses were updated assuming operation in the linear stiffness zone, which corresponds to rather low bushing forces.

Starting with *variant 3 - Non-linear Stiffness*, this linear assumption was dropped and (some) elastomer bushing stiffnesses were implemented parameter-dependent thereafter.

Subsequently, damping parameters were adapted according to chapter 3.1.2.2 for *variant 4 - Best-Model* and then reduced by a factor 100 for *variant 5 - Best-Model Low Damping*.



(\*): Boundaries are applied at the elastomer bushings' nodes on the vehicle's chassis side.

Figure 3.3: Applied boundary constraints for CEA simulation

Influences of the rotational terms within gyroscopic damping matrix, convective stiffness matrix and geometric stiffness matrix were examined in *variant 6 - Best-Model no Rotational Matrices*, where all three matrices were simply omitted.

Improved for moan experiments, *variant 7 - Best-Model Moan rim A* and the variant with different rim design *variant 8 - Best-Model Moan rim B* both feature reduced damping in the wheel contact point, smaller MPCs for the connection to the rim and a higher frequency limit for the computed basis of real modes.

Identical to the related work [38], operational parameters such as brake pressure, vehicle speed or coefficient of friction were chosen in a range relevant for creep groan, see table 3.2. Nevertheless, experimental tests of the investigated axle have revealed moan oscillations for similar parameter sets, therefore *variant 7 - Best-M. Moan-A* and *variant 8 - Best-M. Moan-B* were simulated for the same range of parameters. However, the higher brake pressure limit of  $p_B = 16$  bar was considered less relevant for real world creep groan, even though the corresponding experimental

Table 3.1: Low-frequency CEA model and parameter variant overview

<b>variant name</b>	<b>spring elements*</b>	<b>damping**</b>	<b>rim</b>
<b>variant 1 – Squeal-M.</b>	Squeal values	Squeal values x 0.01	A
<b>variant 2 – Corr. Geom.</b>	Test data, constant	Squeal values x 0.01	A
<b>variant 3 – Non-lin. Stiff.</b>	Test data, partly variable	Squeal values x 0.01	A
<b>variant 4 – Best-M.</b>	Test data, partly variable	Test data	A
<b>variant 5 – Best-M. LD</b>	Test data, partly variable	Test data x 0.01	A
<b>variant 6 – Best-M. no ROT</b>	Test data, partly variable	Test data x 0.01	A
<b>variant 7 – Best-M. Moan-A***</b>	Test data, partly variable	Test data x 0.01	A
<b>variant 8 – Best-M. Moan-B***</b>	Test data, partly variable	Test data x 0.01	B

(\*) all translational and rotational stiffnesses of elastomer bushings as well as the axial stiffness of the vehicle's coil spring according to table 3.4.

(\*\*) discrete viscous damping coefficients of elastomer bushings (see table 3.5) as well as structural damping coefficients

(\*\*\*) no damping in the wheel contact point, less slave nodes of MPC between wheel contact point and rim, increased limit frequency for real modes of 2500 Hz

tests described in [52] were performed up to even higher brake pressures of 40 bar. Summed up, 7 different coefficients of friction, 7 brake pressures and 91 different rotational speeds – calculated from realistic vehicle velocities and the dynamic tire radius – make up an overall amount of 4459 parameter combinations for each of the 8 variants.

### 3.1.2 Elastomer Bushing Behavior

The author and his co-authors already stated the importance of elastomer bushing behavior in [38]. Strong influences on CEA results were found in this work. Therefore, the used methods and calculations for stiffness and damping adaptations based on component test data are explained in this chapter.

Table 3.2: Parameters for CEA simulations

brake pressure $p_B$	4 – 16 bar ;	$\Delta = 2$ bar
vehicle speed $v_{veh}$	0.04 – 0.4 km/h ;	$\Delta = 0.004$ km/h
coefficient of sliding friction $\mu$	0.25 – 0.55 ;	$\Delta = 0.05$
reference vehicle speed $v_{ref}$	0.2 km/h	
frequency limit for real modes $f_{r,lim}$	1 kHz / 2.5 kHz*	

(\*) for variant 7 - Best-M. Moan-A and variant 8 - Best-M. Moan-B

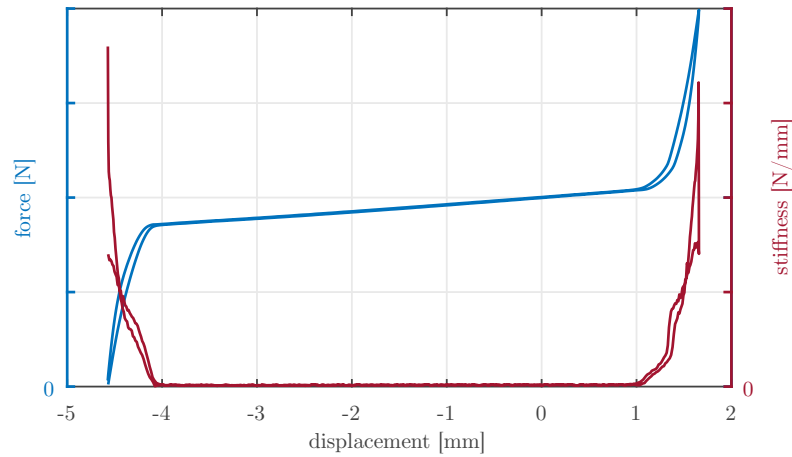
### 3.1.2.1 Elastomer Bushing Stiffness Modeling

At the beginning of the modeling process, elastomer bushing component test data provided by the OEM was analyzed. The examined measurement data included results from both static and dynamic experiments: For the static tests, the bushing specimen was loaded with a certain displacement in a defined direction, e.g. axial or radial to the bushing's main axis. The load was induced with a certain speed in the range of 3 – 30 mm/s, therefore quasi-static behavior can be assumed. By measuring the applied displacement and the corresponding force, the static stiffness parameter in the respective direction was evaluated.

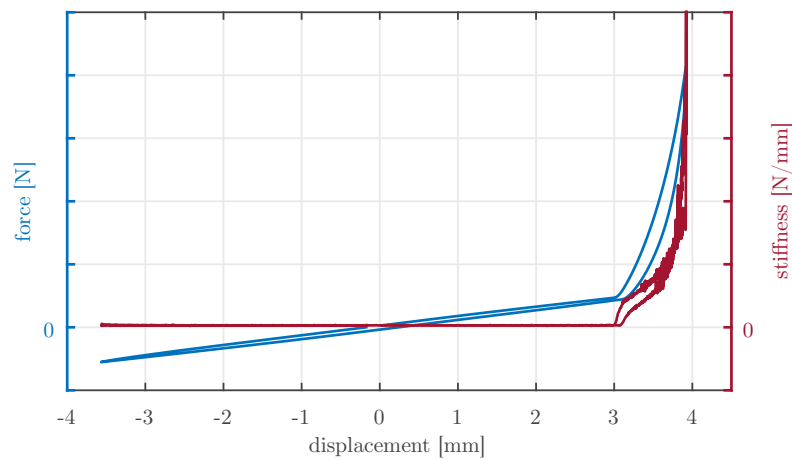
Resulting example stiffness characteristics can be found in fig. 3.4 (a) and (b). As one can see, the investigated bushing clearly shows two different zones of static stiffness: For rather low displacements, an almost constant, rather low static stiffness is provided for good comfort – see chapter 2.2 for details on the requirements for elastomer bushings. For higher displacements, a strong static stiffness increase can be recognized. Here, the bushing is operated in a range where its limit is gradually reached. Furthermore, the non-linear zone is reached at different displacements for positive or negative loading respectively.

Due to typically low brake forces during creep groan or moan, the bushings were assumed to be operated within their linear zone at first. Constant stiffness values, invariant of brake pressure and coefficient of friction, were implemented in the model variant 2 - Corr. Geom. according to the absolute stiffness data in table 3.3. Here,  $c_1$  corresponds to the static translational stiffness value of the spring element in the 1-direction of the local element coordinate system, which is aligned in the axial direction of the respective bushing. Logically,  $c_2$  and  $c_3$  relate to the radial translational stiffnesses whereas  $c_4$ ,  $c_5$  and  $c_6$  represent the rotational stiffnesses about the three local element coordinate axes.

In order to compare these values to the previously used data of squeal investigation, table 3.4 gives the relative stiffness of the bushings within variant 2 - Corr. Geom. when compared to variant 1 - Squeal-M. A glance at the table's values reveals the stiffnesses of variant 2 - Corr. Geom. to be significantly smaller than those of the



(a) Lower control arm: radial, horizontal direction



(b) Upper control arm: axial direction

Figure 3.4: Measured static stiffness characteristics of a control arm's hydraulic elastomer bushing

variant 1 - Squeal-M. Bushing stiffnesses were reduced up to a maximum of 85 % for the radial, horizontal direction of lower control arm's front bushing. Due to their reduced impact on the more 'local' – i.e. concentrated on disk, caliper and wheel carrier – squeal problem, the higher stiffnesses of variant 1 - Squeal-M. were probably appropriate for brake squeal analysis, nevertheless.

In order to verify the assumption about the elastomer bushings' linear static stiffness behavior, a linear static calculation of the support reactions based on axle geometry and kinematics for rigid components was used to verify the occurring bushing forces at first. However, the evaluation of subsequently measured forces for the corresponding vehicle's front corner on the test bench – explained within [52]

Table 3.3: Absolute stiffness values of elastomer bushings and the coil spring within variant 2 - Corr. Geom. in local element coordinates

bushing location	$c_1$	$c_2$	$c_3$	$c_4$	$c_5$	$c_6$
	[N/mm]			[Nm/rad]		
upper control arm - f./r.	150	2 500	2 500	26.4	100.0	100.0
lower control arm - front*	210	400	2 300	83.0	500.0	500.0
lower control arm - rear	1 500	8 500	8 500	100.0	680.0	680.0
lower control arm - strut	480	28 000	28 000	123.0	1 490.0	1 490.0
strut - suspension turret*	1 200	1 400	3 500	100.0	50.2	50.2
coil spring	55	-	-	-	-	-

Note: Local 1-direction corresponds to each bushing's axial direction  
 (\*) 2-direction approx. in vehicle y-direction

Table 3.4: Relative stiffness of variant 2 - Corr. Geom. compared to variant 1 - Squeal-M. in local element coordinates

bushing location	$c_1$	$c_2$	$c_3$	$c_4$	$c_5$	$c_6$
upper control arm - f./r.	38 %	35 %	35 %	46 %	46 %	46 %
lower control arm - front*	35 %	15 %	88 %	48 %	44 %	44 %
lower control arm - rear	63 %	33 %	33 %	38 %	38 %	38 %
lower control arm - strut	60 %	42 %	42 %	60 %	35 %	35 %
strut - suspension turret*	63 %	57 %	57 %	100 %	100 %	100 %
coil spring	73 %	-	-	-	-	-

Note: Local 1-direction corresponds to each bushing's axial direction  
 (\*) 2-direction approx. in vehicle y-direction

– showed significant deviations of up to a factor 10 to the linear static calculation. This could be due to elasto-kinematics and the non-linear behavior of bushings – a check regarding the assumption of linear operation of the bushings seemed necessary.

Therefore, a comparison of the test bench forces with the mentioned static displacement/force/stiffness data provided by the OEM was performed. Meaningful averaging methods were applied in order to retrieve useful results, as many different measuring points combined with hysteresis effects were present in the data sets given.

As a result, it was observed that depending on brake pressure  $p_B$  and coefficient

of friction  $\mu$ , certain elastomer bushings operated clearly within their non-linear stiffness range. In the author's opinion, this could be a reason for the occurrence of non-linear effects such as the super-harmonic peaks especially in creep groan frequency plots, see fig. 2.16 and chapter 2.3.1.

Based on the parameters in table 3.2, the following elastomer bushing stiffnesses showed non-linear behavior of high influence:

- ① lower control arm – front bushing – axial direction
- ② lower control arm – front bushing – radial, horizontal direction
- ③ lower control arm – rear bushing – axial direction
- ④ upper control arm – front bushing – axial direction
- ⑤ upper control arm – rear bushing – axial direction

In fig. 3.5, the position of the non-linear elastomer bushings in the 3D FE model is shown. Numbers correspond to the list above.

Naturally, the inclusion of this nonlinear effect was aspired for all of the five relevant stiffnesses. However, in some cases it was unclear which direction of the component test data was positive or negative in the global vehicle coordinate system. E.g. within fig. 3.4 (a), positive and negative displacements clearly lead to different stiffness behavior. Therefore, only bushing stiffnesses of ②, ④ and ⑤ were implemented parameter dependent for variant 3 - Non-lin. Stiff. and all following variants. Further improvement of the model would be possible with the inclusion of parameter-dependent longitudinal stiffnesses in ① and ③.

Another problem evolved for bushing stiffnesses ④ and ⑤. Here, the same bushing type was mounted two times in opposite direction. The component measurements were taken up to the limit stop for positive displacements only. Hence, no information about the limit stop was available for the negative direction, see fig. 3.4 (b). For a symmetrical bushing mount, axial displacement of the upper control arm would finally lead to a limit stop of one bushing whereas the other bushing was assumed to still operate in its linear range. As no mounting direction was provided by the OEM, axial stiffnesses of front and rear bushing ④ and ⑤ were set equal and computed by an averaging of the non-linear branch and the linear branch according to eq. 3.1.

$$\bar{c}_{\textcircled{4},\textcircled{5}}(p_B, \mu) = \bar{c}_{\text{lin},\textcircled{4},\textcircled{5}} + \bar{c}_{\text{nonlin},\textcircled{4},\textcircled{5}}(p_B, \mu) \quad (3.1)$$

As the stiffnesses were assumed to correspond directly to the brake force, the parameters brake pressure  $p_B$  and coefficient of friction  $\mu$  were used for the definition. Naturally, the coefficient of friction could not be altered during the experimental tests, therefore a linear extrapolation was performed for  $\mu$ -values differing from the estimated real value.

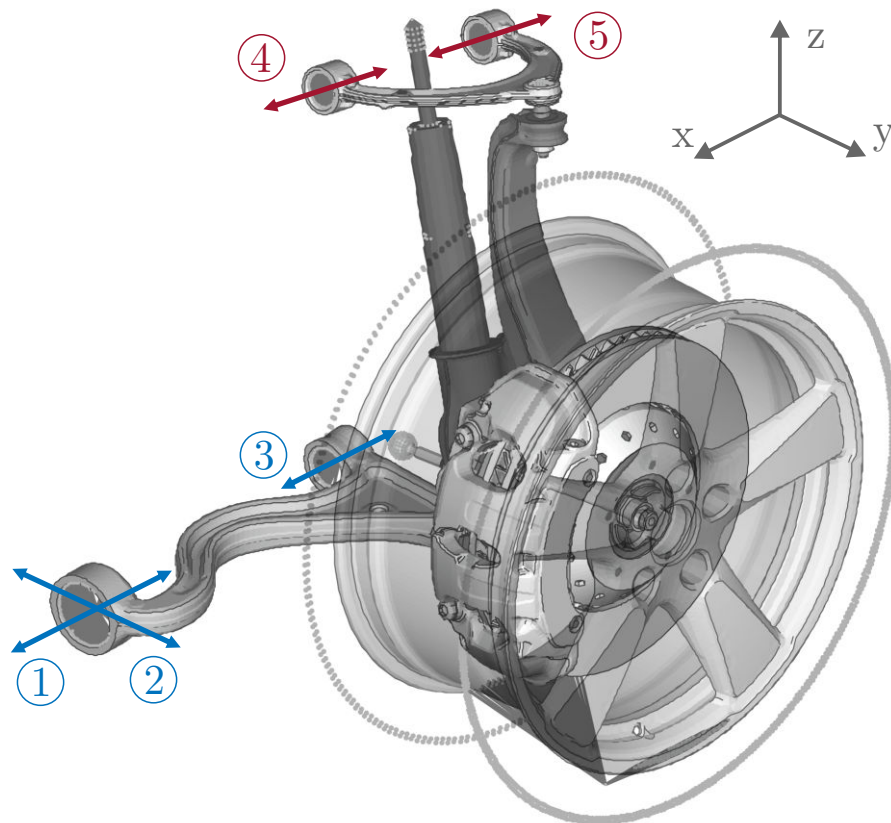


Figure 3.5: Elastomer bushing stiffnesses with significant non-linear behavior in the relevant simulative parameter range

For an assumed real-life coefficient of friction  $\mu = 0.4$ , parameter-dependent stiffnesses can be found in fig. 3.6. One can clearly see a limit-stop with increasing stiffness for higher brake pressures and therefore higher brake forces, beginning at 9.5/10.5 bar. With the stated  $\mu = 0.4$ , these brake pressures would be necessary to hold the corresponding vehicle in standstill on a 16 – 17% slope.

Dynamic effects describing relations between stiffness, excitation amplitude and frequency were neglected in this first approach. Consideration of these remarks could further improve the quality of model and results. However, sophisticated and well-documented component measurements are necessary for such measures.

### 3.1.2.2 Elastomer Bushing Damping Modeling

The component test data provided by the OEM contained no direct information about equivalent viscous damping factors. It was assumed that the tests were realized by exciting the specimen with a harmonic oscillation of certain amplitude

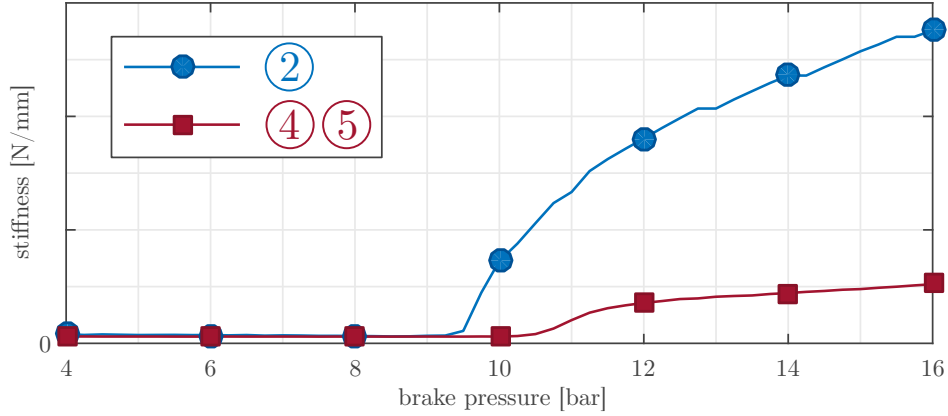


Figure 3.6: Bushing stiffness over brake pressure for parameter-dependent implemented bushings and a coefficient of friction  $\mu = 0.4$ , based on [38]. Marked data points were used within simulation.

and frequency. Measured quantities were loss angle  $\gamma$  and a dynamic or complex stiffness  $c_{\text{dyn}}$ .

Based on this, necessary viscous damping values were calculated according to [1], [24] and [26]. Starting point is the differential equation of a force-excited, damped, single mass harmonic oscillator, which is given in eq. 3.2.

$$m\ddot{x}(t) + d\dot{x}(t) + cx(t) = p(t) \quad (3.2)$$

In the following, a cosine/sine excitation  $p(t)$  like in eq. 3.3 and, therefore, an approach for  $x(t)$  according to eq. 3.4 are assumed. Together with the relation given in eq. 3.5, showing the effect of the loss angle as an additional phase shift between excitation and resulting displacement, the differential equation forms to eq. 3.6. [26]

$$p(t) = |p| \cos(\Omega t - \beta) \quad (3.3)$$

$$x(t) = |x| \cos(\Omega t - \Psi) \quad (3.4)$$

$$\Psi = \beta + \gamma \quad (3.5)$$

$$|x| \cdot [\cos(\Omega t - \Psi) \cdot (c - \Omega^2 m) + \sin(\Omega t - \Psi) \cdot (-d\Omega)] = |p| \cos(\Omega t - \beta) \quad (3.6)$$

Via substitution of sinus and cosinus functions within eq. 3.6 by means of the Euler's formula (eq. 3.7) and its rearranged versions stated in eq. 3.8, the according complex terms in eq. 3.9 appear. [26]

$$e^{i\Omega t} = \cos \Omega t + i \sin \Omega t \quad (3.7)$$

$$\cos \Omega t = \frac{1}{2} (e^{i\Omega t} + e^{-i\Omega t}) \quad , \quad \sin \Omega t = \frac{1}{2i} (e^{i\Omega t} - e^{-i\Omega t}) \quad (3.8)$$

Eq. 3.9 describes oppositely rotating vectors within the complex area: Whereas  $x^+ \cdot \frac{1}{F^+}$  and  $p^+$  rotate with  $\Omega$ ,  $x^- \cdot \frac{1}{F^-}$  and  $p^-$  rotate with the inverse rotational speed  $-\Omega$ . Together, both imaginary parts of these conjugate-complex vectors result to zero – only the real parts are of interest. [26]

$$\begin{aligned} \underbrace{\frac{|x|}{2} e^{-i\psi}}_{x^+} \cdot \underbrace{(-\Omega^2 m + id\Omega + c)}_{1/F^+} \cdot e^{i\Omega t} + \underbrace{\frac{|x|}{2} e^{i\psi}}_{x^-} \cdot \underbrace{(-\Omega^2 m - id\Omega + c)}_{1/F^-} \cdot e^{-i\Omega t} = \\ = \underbrace{\frac{|p|}{2} e^{-i\beta}}_{p^+} \cdot e^{i\Omega t} + \underbrace{\frac{|p|}{2} e^{i\beta}}_{p^-} \cdot e^{-i\Omega t} \end{aligned} \quad (3.9)$$

Therefore, simply the positive amplitude equation in eq. 3.10 is considered in most cases. The other resulting amplitude equation, eq. 3.11, is irrelevant subsequently.

$$x^+ = F^+ \cdot p^+ \quad (3.10)$$

$$x^- = F^- \cdot p^- \quad (3.11)$$

With this in mind, the force-excited displacement oscillation  $x$  can be written based on the complex domain according to eq. 3.12. [26]

$$x = 2 \cdot \Re\{x^+ \cdot e^{i\Omega t}\} = 2 \cdot \Re\{F^+ p^+ \cdot e^{i\Omega t}\} \quad (3.12)$$

Similarly, the occurring forces can be computed as in eq. 3.13. Additional phase angles of  $\pi$  or  $\frac{\pi}{2}$  in mass and damping force terms compensate for negative amplitude and  $90^\circ$  phase shifts respectively. In fig. 3.7, these relations between the different forces and their phase behavior are depicted in the complex area. As one can see, the rotating vector of the excitation force can be summed up by the three parts of the component's forces: mass force, viscous damping force and elastic spring force. Details can be found within [26].

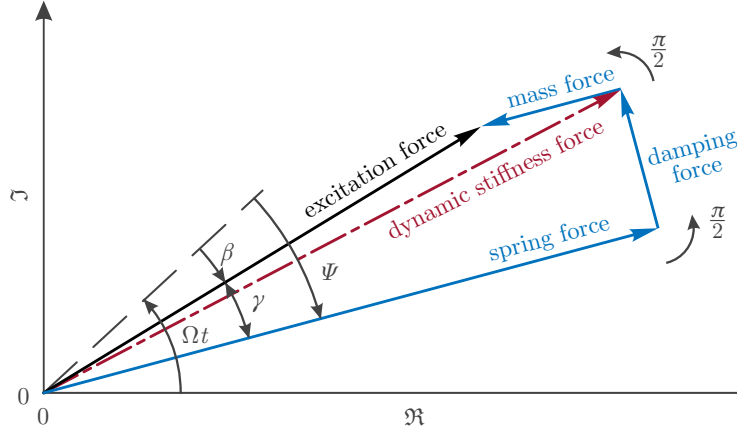


Figure 3.7: Phase relationships of forces on a force-excited single mass oscillator depicted as vectors in the complex plane, adapted from [26]

$$\begin{aligned}
 & \underbrace{|x| \cdot m\Omega^2 \cdot \Re \left\{ e^{i(\Omega t + \pi - \Psi)} \right\}}_{\text{mass force}} + \underbrace{|x| \cdot d\Omega \cdot \Re \left\{ e^{i(\Omega t + \pi/2 - \Psi)} \right\}}_{\text{damping force}} + \\
 & \underbrace{|x| \cdot c \cdot \Re \left\{ e^{i(\Omega t - \Psi)} \right\}}_{\text{spring force}} = \underbrace{|p| \cdot \Re \left\{ e^{i(\Omega t - \beta)} \right\}}_{\text{excitation force}}
 \end{aligned} \tag{3.13}$$

At this point, the term of the *dynamic stiffness* or also *complex stiffness* needs to be introduced: According to eq. 3.14, the dynamic stiffness is computed by the quotient of maximum transient force change  $\Delta F$  and maximum transient displacement change  $\Delta x$ . As stated in eq. 3.14, dynamic or complex stiffness can also be computed as the magnitude of the vector sum of viscous damping and elastic stiffness. [1], [13], [24]

$$c_{\text{dyn}} = \frac{\Delta F}{\Delta x} = \sqrt{c^2 + (\Omega d)^2} \tag{3.14}$$

This value is especially important for the testing of elastomer materials, as one can see in fig. 3.8: The dynamic excitation of a typical elastomer bushing material leads to an increase of stiffness compared to the static stiffness behavior. Causation is the dynamic hardening effect and the introduction of damping. With increasing loss angle, the dynamic stiffness increases too. Furthermore, because mass forces are typically rather small during dynamic measurements of elastomer bushings, excitation forces are approximately equal to the dynamic stiffness force, see fig. 3.7. [1], [13], [24]

Hence, the loss angle  $\gamma$  of the resulting oscillation, see again fig. 3.7, is shown by the terms in eq. 3.15. This relation demonstrates that the loss angle is defined by the

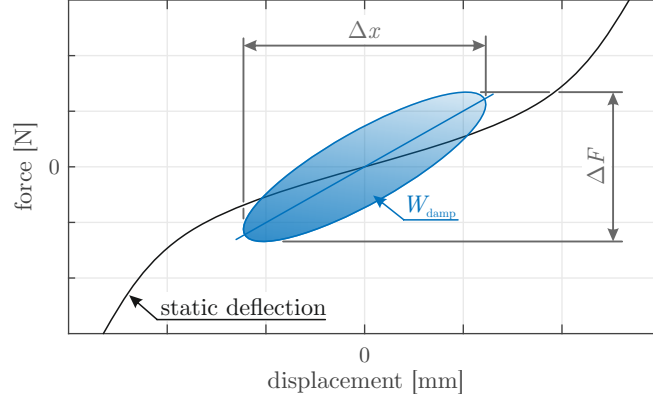


Figure 3.8: Dynamic force-displacement behavior in the presence of hysteresis effects, based on [32]

fraction between the imaginary part  $\Omega d$  and the real part  $c - \Omega^2 m$  of the complex amplitude characteristic  $F^+$ , if the oscillation is considered as a complex function. Neglecting mass forces finally leads to the practical relation for calculation of the necessary viscous damping values as in 3.16. [1], [26]

$$\gamma = \arctan \left( -\frac{\Im\{F^+\}}{\Re\{F^+\}} \right) = \arctan \frac{\Omega d}{c - \Omega^2 m} \approx \arcsin \frac{\Omega d}{c_{\text{dyn}}} \quad (3.15)$$

$$\Rightarrow d \approx \frac{\sin \gamma}{\Omega} \cdot c_{\text{dyn}} \quad (3.16)$$

Within some of the OEM's component tests, the dissipated energy per oscillation cycle or also the damping work  $W_{\text{damp}}$  was measured. As depicted in fig. 3.8, this parameter corresponds to the area encircled by the force-displacement curve. In eq. 3.17 the computation of this quantity via integration of the incremental damping work is shown. Here,  $x(t)$  is a cosine oscillation without phase delay and with an amplitude of  $\frac{\Delta x}{2}$ , similar to fig. 3.8. [32]

$$\begin{aligned} W_{\text{damp}} &= \int_0^{x_{\text{cycle}}} F_{\text{damp}}(t) dx \\ &= \int_0^T \underbrace{\left[ -d \cdot \frac{\Delta x}{2} \Omega \sin(\Omega t) \right]}_{F_{\text{damp}}(t)} \cdot \underbrace{\left[ -\frac{\Delta x}{2} \Omega \sin(\Omega t) \right]}_{dx} dt \\ &= d \left( \frac{\Delta x}{2} \right)^2 \Omega^2 \cdot \int_0^{\frac{2\pi}{\Omega}} \sin^2(\Omega t) dt \\ &= d \left( \frac{\Delta x}{2} \right)^2 \Omega \pi \end{aligned} \quad (3.17)$$

The relation to the loss angle  $\gamma$  is found via equating the two different approaches towards computation of the viscous damping value  $d$ , see eq. 3.18. Eq. 3.19 clearly shows the damping work's relation to the encircled area of the force-displacement characteristic: It is computed by reducing an ellipsoidal area – with the semi-major axis  $\frac{\Delta F}{2}$  and the semi-minor axis  $\frac{\Delta x}{2}$  – by a factor  $\sin \gamma$ , which explains the ratio of viscous loss stiffness compared to the elastic stiffness. [24]

$$d = \frac{W_{\text{damp}}}{\pi \left(\frac{\Delta x}{2}\right)^2} = \frac{\sin \gamma}{\Omega} \cdot c_{\text{dyn}} \quad (3.18)$$

$$\Rightarrow W_{\text{damp}} = \underbrace{\frac{\pi}{4} \Delta F \Delta x}_{\text{ellipsoidal area}} \sin \gamma \quad (3.19)$$

For the practical determination of viscous damping values, the frequency-dependency of the bushing's damping behavior was neglected. Instead, the measurements were simply evaluated at a reference frequency  $f_{d,\text{ref}} = 50$  Hz. This was assumed a good approximation, as the reference was positioned in the middle of the usual bandwidth of creep groan up to 100 Hz and measurements of the corresponding axle system have shown dominant frequencies between approx. 20 – 95 Hz, see chapter 2.4.1.1 and [38], [52].

A comparison of elastomer bushing damping values between the existing squeal model and the component test data for the stated reference frequency of  $f_{d,\text{ref}} = 50$  Hz can be seen within table 3.5. Here, the necessary multiplication factors from squeal model to actually measured values are given. As one can see, all values are  $\geq 1$ , meaning that the squeal model featured generally lower damping than measured in component tests. The highest relative increases were found at the lower control arm's rear bushing in local 1-direction (axially) with a factor of 64.2 and at both upper control arm's bushings in axial direction with a factor of 26.3.

As already stated, all viscous and structural damping influences were reduced within most of the variants by a factor of 100 in order to obtain unstable eigenvalues as shown within the variant overview in table 3.1. Only exception was variant 4 - Best-M., which featured parameters set to the best of the author's knowledge. This absolute damping data can be found in table 3.6. Especially the relatively high values found in the radial direction of the lower control arm's rear bushing and in the bushing between lower control arm and strut attract attention. Certainly, damping relations between the different damping elements themselves stayed identical for all following variants.

Table 3.5: Relative changing factor of elastomer bushing viscous damping values from variant 1 - Squeal-M. to variant 4 - Best-M. in local element coordinates

bushing location	$d_1$	$d_2$	$d_3$
	[-]		
upper control arm - front / rear	26.3	14.1	14.1
lower control arm - front*	7.7	13.2	15.7
lower control arm - rear	64.2	18.1	18.1
lower control arm - strut	19.0	6.9	6.9
strut - suspension turret*	15.6	1.0	1.0

Note: Local 1-direction corresponds to each bushing's axial direction  
 (\*) 2-direction approx. in vehicle y-direction

Table 3.6: Absolute viscous damping values of elastomer bushings and the suspension damper within variant 4 - Best-M. in local element coordinates

bushing location	$d_1$	$d_2$	$d_3$
	[Ns/mm]		
upper control arm - front / rear	0.105	0.945	0.945
lower control arm - front*	0.046	0.316	0.376
lower control arm - rear	1.413	4.375	4.375
lower control arm - strut	0.133	4.221	4.221
strut - suspension turret*	0.057	0.023	0.280
suspension damper	5.720	-	-

Note: Local 1-direction corresponds to each bushing's axial direction  
 (\*) 2-direction approx. in vehicle y-direction

### 3.1.3 Simulation Procedure

The classical brake squeal procedure consisting of

- Step 1: Static, Non-linear Contact Analysis
- Step 2: Linear Static Analysis
- Step 3: Real Eigenvalue Analysis
- Step 4: Complex Eigenvalue Analysis

according to chapter 2.5 was performed with the FE-solver PERMAS for all eight different variants in table 3.1. With the respective parameters, see table 3.2, the

following process was done:

At first, the contact state was evaluated in step 1 for one brake pressure  $p_B$  and the first coefficient of friction  $\mu$  between brake disk and pads. In addition to the load introduced by the brake pressure, inertia forces due to the rotation of the wheel were implemented according to the reference vehicle speed  $v_{\text{ref}}$ .

In step 2, the rotational stiffness matrices and the gyroscopic matrix were computed based on the locked contact state of step 1. Again, inertia forces due to the rotating wheel were applied.

After the computation of real modes in step 3 and a modal reduction, complex eigenvalues were calculated in step 4 based on the full system in eq. 2.38. In the end, sampling was performed: The resulting complex eigenvalues were computed for all different rotational speeds.

These four steps were repeated for the other coefficients of friction. In the end, this procedure was performed for every brake pressure  $p_B$ .

A computation time of approx. 23 h 30 min resulted for the complete simulation of the whole parameter range of one of the full-size variants according to table 3.1. Here, eight processor cores and 97.66 GiB of main memory were used on a workstation with an Intel Xeon E5-2620 processor.

## 3.2 Investigation of the CEA System Matrices

For better understanding and evaluation of certain parameter's importance, this chapter shows an evaluation of system matrices. Matrices of full-scale FE-model variant 5 - Best-M. LD according to table 3.1 were output from PERMAS. With the software tool MATLAB, simple depictions of the system matrices were created.

In this case, parameters were set to a hydraulic brake pressure of  $p_B = 10$  bar and a coefficient of friction of  $\mu = 0.4$ . The vehicle reference speed was set to  $v_{\text{ref}} = 0.2 \frac{\text{km}}{\text{h}}$ . Results of this analysis are shown in the figures 3.9 and 3.10. Both figures show depictions of the system's condensed matrices. As 70 real modes were calculated as a new basis, each matrix consists of 70 rows and columns. Every single matrix entry is represented by a filled square with red color for positive entries and blue for negative entries. The square's area corresponds to the magnitude of the value, all squares are normalized with respect to the biggest occurring absolute value within each single matrix.

In the following, each PERMAS data object and the corresponding modal matrix in eq. 2.38 is explained in detail:

Fig. 3.9 (a): Data object BMMLL.

The modal mass matrix  $\widetilde{\mathbf{M}}$  is a diagonal matrix with real modes  $\frac{1}{\omega_{\text{real}}^2}$  in the diagonal. This is a result of the default stiffness-normalization in PERMAS.

Fig. 3.9 (b): Data object BKMLL.

The modal elastic stiffness matrix  $\widetilde{\mathbf{K}}_{\text{el}}$  is a diagonal matrix with only ones in the diagonal due to the stiffness normalization performed in PERMAS.

Fig. 3.9 (c): Data object BKQMLL.

The modal asymmetric stiffness matrix due to contact friction terms  $\widetilde{\mathbf{K}}_{\text{Ct}}$  contains non-symmetric parts of stiffness based on the frictional contact. As stated in chapter 2, this asymmetry can lead to unstable complex eigenvalues. When compared to the modal elastic stiffness matrix  $\widetilde{\mathbf{K}}_{\text{el}}$ , one can see that this matrix contains maximum values approx. one decimal power smaller. Furthermore, this matrix has no influence on structural damping, which is referred to the elastic, symmetric stiffness matrix.

Fig. 3.9 (d): Data object BWMLL.

The symmetric rotational stiffness matrix contains elements of modal geometric stiffness matrix  $\widetilde{\mathbf{K}}_{\text{G}}$  as well as of modal convective stiffness matrix  $\widetilde{\mathbf{K}}_{\text{C}}$  for deviations to the reference rotational speed. A factor  $\left(\frac{\Omega_i}{\Omega_{\text{ref}}}\right)^2 - 1$  is applied to these matrices, for reference rotational speed  $\Omega_{\text{ref}}$  the influence of the rotational stiffness matrix becomes zero. If the current sampling speed  $\Omega_i$  is higher, this matrix is multiplied with a positive factor and added to the sum of stiffness matrices. On the contrary, a negative factor is applied for rotational speeds lower than the reference. As this matrix refers to the rotating structures, high values are reached only for eigenmodes with high movement of disk and other rotating parts. With maximum values in the range of  $10^{-8}$ , they only play a minor role when compared to the modal elastic stiffness matrix  $\widetilde{\mathbf{K}}_{\text{el}}$ . Especially the chosen groan-relevant reference speed in table 3.2 has big influence on this matrix.

Fig. 3.10 (a): Data object BDMRLL.

This matrix contains the modal viscous damping matrix  $\widetilde{\mathbf{D}}_{\text{V}}$  as well as the modal damping matrix due to Coulomb friction  $\widetilde{\mathbf{D}}_{\text{Ct}}$  for the reference rotational speed  $\Omega_{\text{ref}}$ . With these terms, this matrix is a general symmetric matrix. Here, only positive terms were found in the diagonal.

Fig. 3.10 (b): Data object BHMRL.

Modal structural damping matrix  $\widetilde{\mathbf{H}}$  is a symmetric matrix corresponding to the modal elastic stiffness matrix  $\widetilde{\mathbf{K}}_{\text{el}}$ . If the model consists only of volume elements and each material has an assigned structural damping, modal structural damping matrix would be a diagonal matrix with the structural damping coefficient times the elastic stiffness values  $g_{\text{damp}} \cdot \widetilde{\mathbf{K}}_{\text{el}}$  on the diagonal. However, generally this is not the case and the modal structural damping matrix can be a symmetric matrix, containing positive as well as negative values with all its diagonal terms being positive. A conversion according to eq. 2.35 leads to an equivalent viscous damping matrix,  $\widetilde{\mathbf{D}}_{\text{eqv}}$ . Even for the lowest used reference frequency of  $f_{\text{H,ref}} = 100$  Hz, maximum values of this matrix are more than one decimal power smaller than the biggest viscous and frictional damping terms.

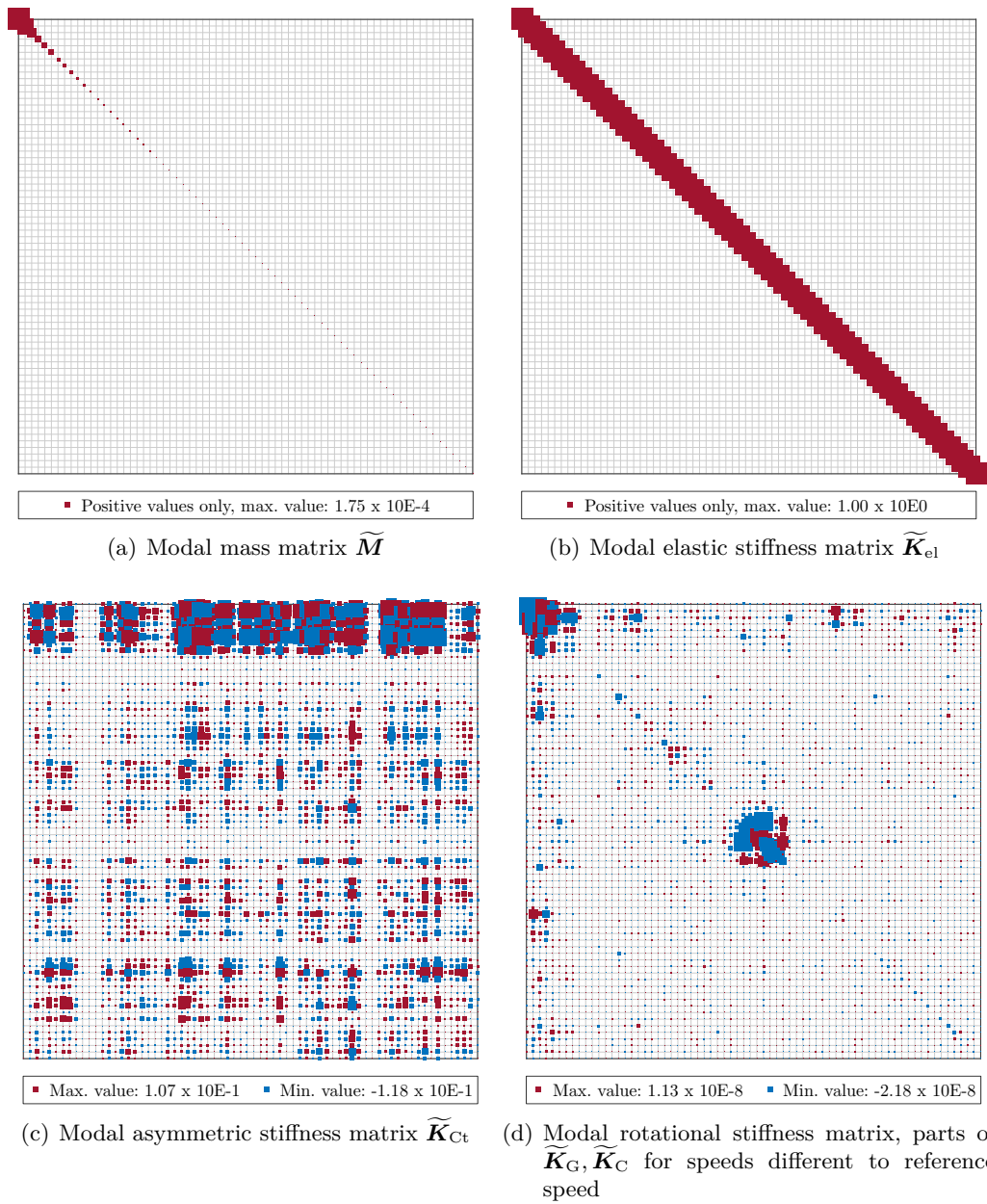


Figure 3.9: Modal mass and stiffness matrices for the full-scale model of variant 5 - Best-M. LD according to table 3.1

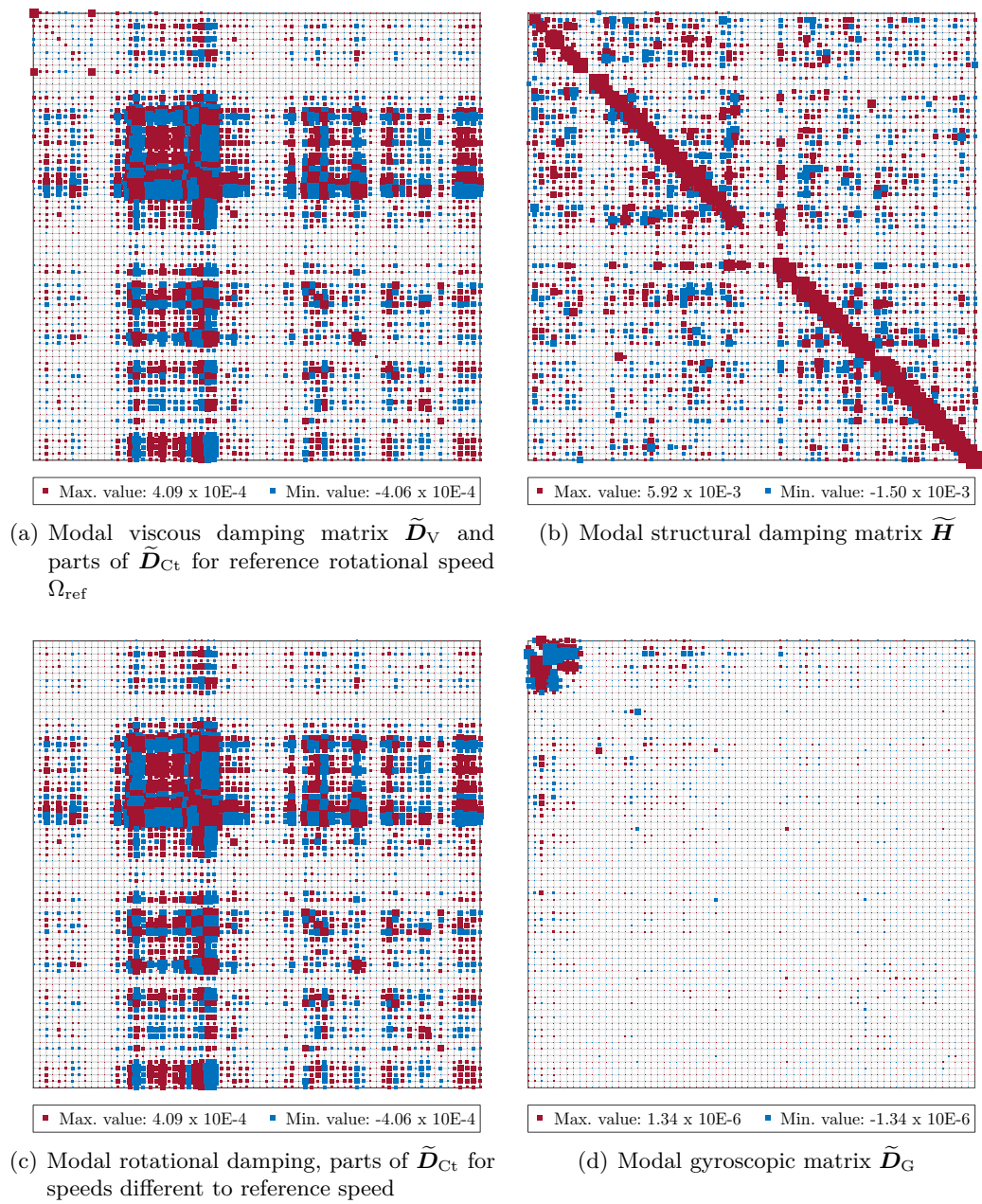


Figure 3.10: Modal speed-dependent and damping matrices for the full-scale model of variant 5 - Best-M. LD according to table 3.1

Fig. 3.10 (c): Data object BDIWMLL.

Modal rotational damping matrix is a symmetric matrix containing speed-dependent damping deviations of the modal damping matrix due to Coulomb friction  $\tilde{\mathbf{D}}_{\text{Ct}}$ . Here, a factor  $\frac{\Omega_{\text{ref}}}{\Omega_i} - 1$  is applied. Again,  $\Omega_i$  refers to the current sampling rotational speed. This means, damping is reduced for higher speeds than the reference speed and vice versa. When compared to fig. 3.10 (a), it can be seen that this matrix is the major part of the modal viscous damping matrix  $\tilde{\mathbf{D}}_{\text{V}}$  for reference speed. All its diagonal terms are positive.

Fig. 3.10 (d): Data object BYMLL.

Modal gyroscopic matrix  $\tilde{\mathbf{D}}_{\text{G}}$  is a skew-symmetric (or anti-metric  $\tilde{\mathbf{D}}_{\text{G}}^{\text{T}} = -\tilde{\mathbf{D}}_{\text{G}}$ ) matrix containing terms due to gyroscopic effects. This matrix is only generated if explicitly requested and is multiplied with the factor  $\frac{\Omega_i}{\Omega_{\text{ref}}}$  in regard of its speed-dependence. Similar to the rotational stiffness terms, tight relation to the rotor modes can be found. Furthermore, it can be recognized that all diagonal elements are zero and only factors for the first nine modes show significant values, see the upper left corner of fig. 3.10 (d). Gyroscopic effects with maximum terms of approx.  $10^{-6}$  were found about two decimal powers smaller than the viscous damping terms in this example with very low rotational speeds. Hence, they play only a minor role. Nevertheless, gyroscopic terms are known to influence stability behavior in significant manner even if magnitudes are low, see e.g. [34].



---

## 4 Results

In this chapter, results gained by CEA model and parameter variations are presented. Due to their high informative value, displacements of relevant unstable and stable modes are presented at first. In the following, frequency and stability results for the eight different variants are shown.

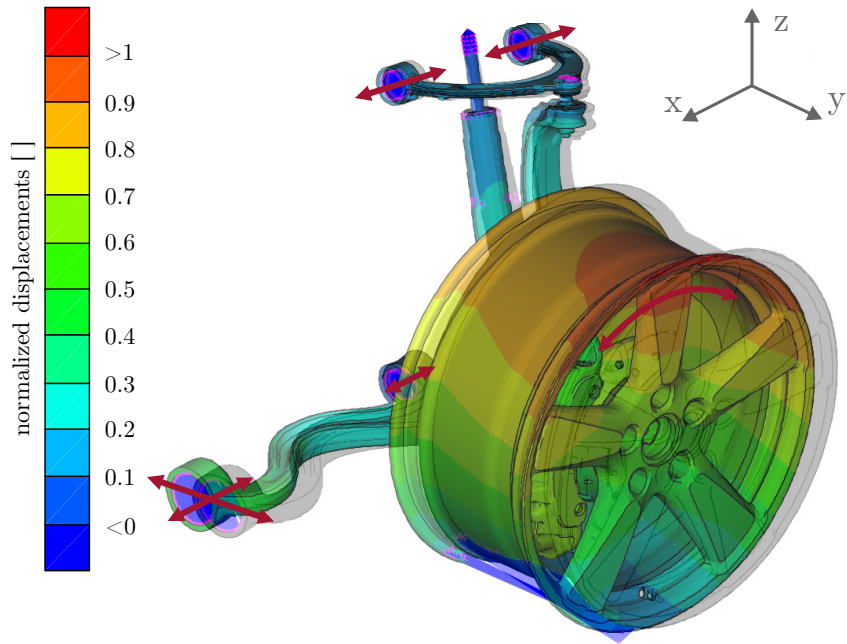
### 4.1 Displacement Results

An overview about all unstable mode forms found in the relevant parameter range, as stated in table 3.2, can be found in table 4.1. Due to different variants with changing values for spring and damper elements as well as different operational parameters, certain ranges can be found for the calculated eigenfrequencies. Unstable modes #1 - #5 relate to the unstable modes already presented in the related work [38] whereas unstable mode #6 was found for a moan-optimized simulation. Moreover, one fully stable mode, relevant mode #7 is included in this table because a relation to brake moan seemed likely.

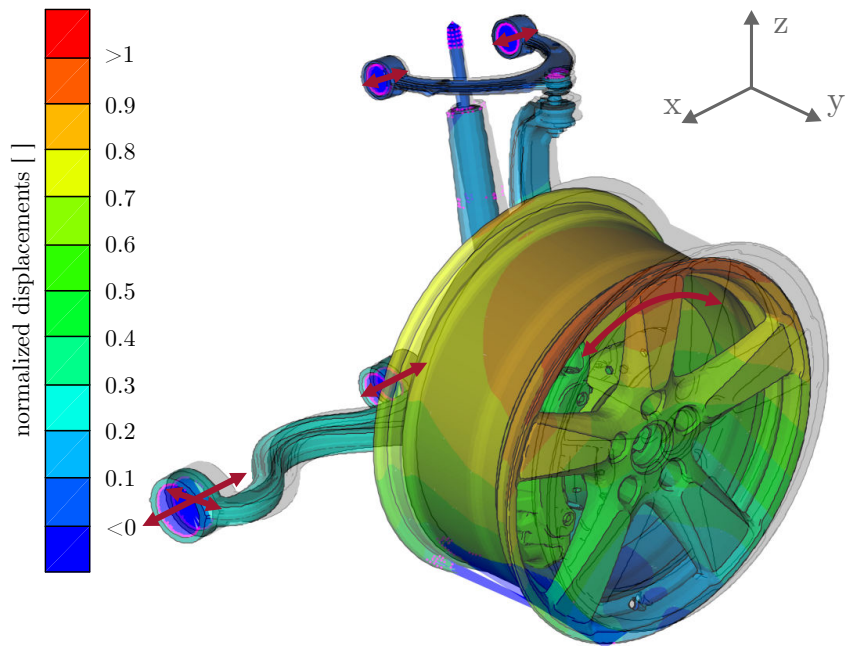
#### 4.1.1 Unstable Mode #1

The displacement range of unstable mode #1 is shown in fig. 4.1 (a). Based on variant 3 - Non-lin. Stiff. and the parameters coefficient of friction  $\mu = 0.4$  and brake pressure  $p_B = 4$  bar, a forward/backward rolling movement of the wheel about the contact point to the road surface can be seen clearly. Moreover, upper as well as lower control arm displace in longitudinal direction within their elastomer bushings. Additionally, high movement can be seen in the lower control arm's front bushing in radial, horizontal direction.

A comparison with fig. 4.1 (b) already gives a first impression of effects caused by non-linearly parameter-dependent bushing stiffnesses: Here, the same model variant is shown for identical  $\mu$  but a higher brake pressure  $p_B = 16$  bar. Less longitudinal movement in the upper control arm's elastomer bushings can be seen. At the lower control arm's front bushing, less radial movement and higher axial movements in both front and rear bushing occur. These effects relate to the increase of static bushing stiffness with brake force/brake pressure. Effects already start at lower brake pressures of approx. 9.5/10.5 bar, see fig. 3.6.



(a) Brake pressure  $p_B = 4$  bar



(b) Brake pressure  $p_B = 16$  bar

Figure 4.1: Normalized displacements of unstable mode #1 for variant 3 – Non-lin. Stiff. (table 3.1) with coefficient of friction  $\mu = 0.4$  at vehicle reference speed  $v_{\text{ref}}$

Table 4.1: Unstable modes and other relevant modes found by CEA variant analysis and resulting eigenfrequency minima & maxima over all eight variants according to table 3.1

no.	displacement of unstable mode	eigenfrequency
#1	rotation of wheel back and forth, upper control arm moves axially, lower control arm moves axially/transversally	10.9 – 18.4 Hz
#2	wheel rotates about steering axis	26.5 – 31.0 Hz
#3	upper control arm oscillates axially, caliper/pads rotate in phase about wheel axis	48.4 – 93.5 Hz
#4	spring/damper assembly bends and oscillates in longitudinal direction	66.0 – 82.4 Hz
#5	spring/damper assembly oscillates transversally	78.9 Hz
#6	1 <sup>st</sup> torsional mode rim A; bending modes of control arms and spring/damper assembly	562.5 – 563.4 Hz
#7*	1 <sup>st</sup> torsional mode rim B	358.7 Hz

(\*) This complex mode did not occur unstable. However, due to its high importance it is stated here and evaluated as well in the following.

#### 4.1.2 Unstable Mode #2

Peak displacements of unstable mode #2 for variant 3 - Non-lin. Stiff. with a coefficient of friction  $\mu = 0.4$  and a brake pressure  $p_B = 16$  bar are shown in fig. 4.2. Basically, rotational movement of the wheel about the nearly vertical steering axis can be found. Because neither rotational stiffness nor rotational damping were implemented in the model's wheel contact point, this unstable mode is considered irrelevant: Both parameters are estimated rather high in real world application due to the tire material's behavior in the contact patch. Hence, this mode will not be treated further.

#### 4.1.3 Unstable Mode #3

Fig. 4.3 (a) shows the displacement range of unstable mode #3 for variant 3 - Non-lin. Stiff. with parameters  $\mu = 0.4$  and  $p_B = 4$  bar. To have a better view on relevant parts, rim and tire are hidden in this depiction. Here, a forward/backward displacement of the upper control arm within its elastomer bushings is essential. Related to this, a rotation of brake caliper and wheel carrier about the wheel axis occurs. Moreover, the lower control arm displaces in its front bushing's radial horizontal direction. Its connection to the spring with damper assembly initiates

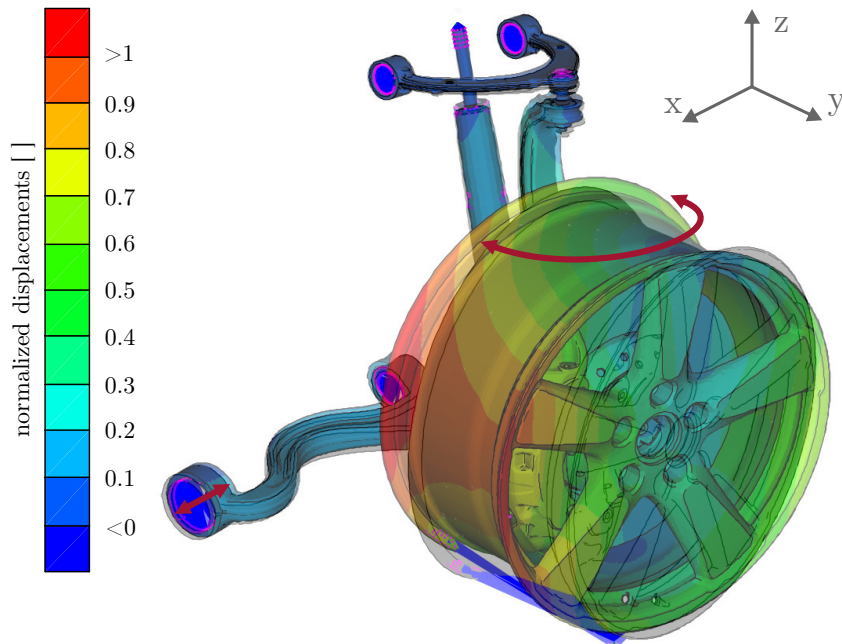


Figure 4.2: Normalized displacements of unstable mode #2 for variant 3 – Non-lin. Stiff. (table 3.1) with parameters  $\mu = 0.4$  and  $p_B = 16$  bar at vehicle reference speed  $v_{\text{ref}}$

oscillations similar to unstable mode #4, see therefore fig. 4.4 (a). For unstable mode #3 at this rather low brake pressure, displacements of lower control arm and spring with damper assembly are actually in phase. However, due to the axle's kinematics, the spring with damper assembly's oscillation seems to be in opposite phase to the upper control arm.

With the brake pressure increased to  $p_B = 16$  bar in fig. 4.3 (b), different displacements can be found due to stiffening of non-linear static bushing stiffnesses. In this case, the upper control arm does not move axially in its elastomer bushings but exhibits rotational oscillations about a vertical axis. Moreover, the lower control arm displaces mainly forward/backward due to the stiffening of the front bushing in its radial horizontal direction. In addition, a change of phase between spring with damper assembly and lower control arm can be seen. This can be related to the changing eigenfrequencies. Like for unstable mode #1, these effects already occur for lower brake pressures at 9.5/10.5 bar.

#### 4.1.4 Unstable Mode #4

Displacement peaks of unstable mode #4 can be seen in fig. 4.4 (a). Again, results for a low brake pressure of 4 bar and a coefficient of friction  $\mu = 0.4$  of variant 3 -

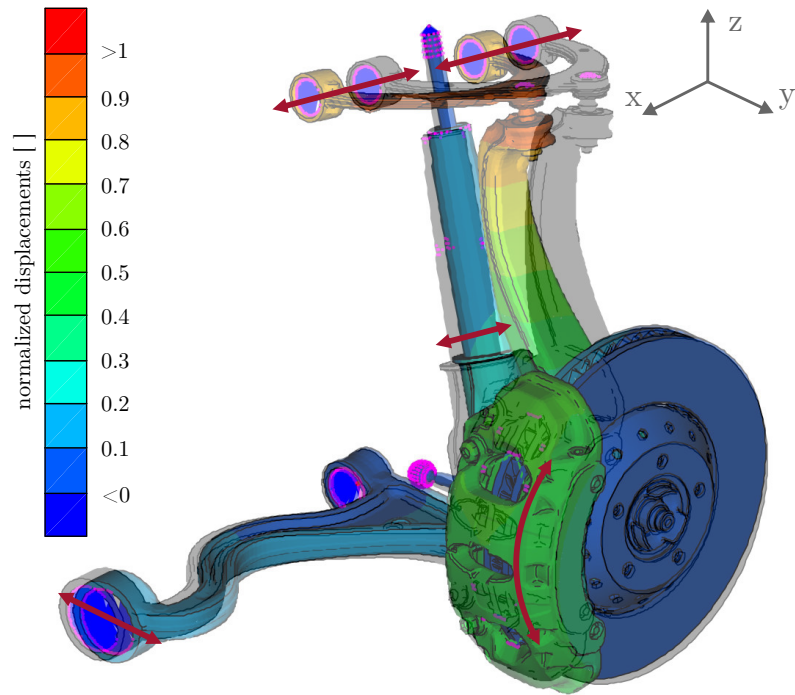
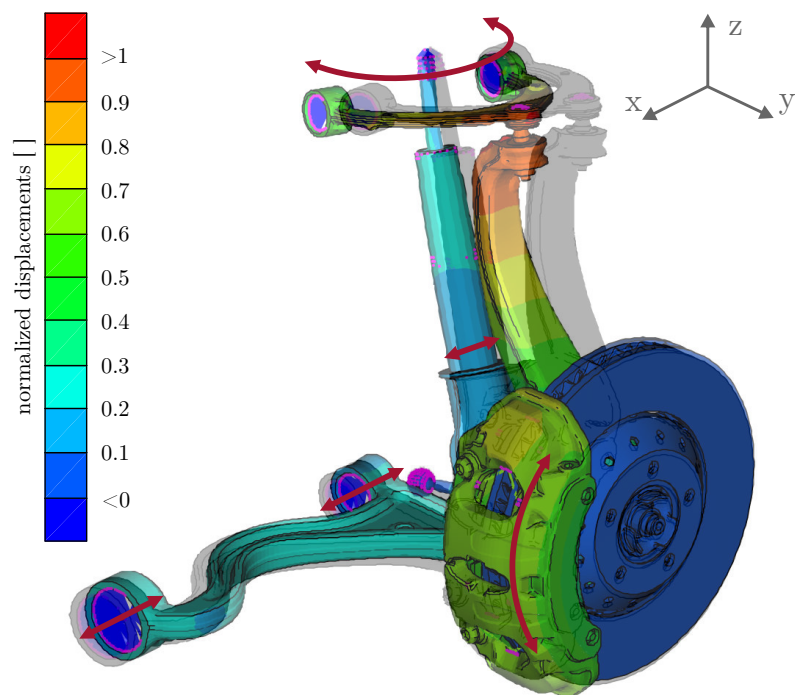
(a) Brake pressure  $p_B = 4$  bar(b) Brake pressure  $p_B = 16$  bar

Figure 4.3: Normalized displacements of unstable mode #3 for variant 3 – Non-lin. Stiff. (table 3.1) with coefficient of friction  $\mu = 0.4$  at vehicle reference speed  $v_{\text{ref}}$

Non-lin. Stiff. are examined. In this case, a forward/backward bending oscillation of the spring with damper assembly is dominant. Moreover, the already mentioned forward/backward movement of the upper control arm and a radial, horizontal displacement in the lower control arm's front elastomer bushing similar to unstable mode #3 can be noted, which indicates modal coupling. Strut with damper assembly's 1<sup>st</sup> bending mode is opposite phased to the lower control arm's displacement, therefore it seems to be in phase with the wheel carrier and the upper control arm.

For a higher brake pressure of 16 bar, displacements of unstable mode #4 can be seen in fig. 4.4 (b). Similarly, the mentioned reduced displacement in the stiffening bushings can be observed. Additionally, a phase shift between spring with damper assembly and the upper control arm can be seen when compared with fig. 4.4 (a).

### 4.1.5 Unstable Mode #5

Unstable mode #5, depicted in fig. 4.5 for variant 3 - Non-lin. Stiff., became unstable only for the shown parameter combination of  $\mu = 0.45$  and  $p_B = 10$  bar. Main movement is the 1<sup>st</sup> transverse bending mode of the spring with damper assembly. Additionally, the brake caliper rotates about the wheel axis, leading to forward/backward displacements of the wheel carrier's upper end and a horizontal rotation of the upper control arm. In comparison to other displacements at other parameter sets, qualitative changes were found. Because of this and its very rare unstable occurrence, this complex mode is not examined further.

### 4.1.6 Unstable Mode #6

Regarding moan relevant modes, unstable mode #6 is shown for variant 7 - Best-M. Moan-A and the parameters  $\mu = 0.55$ ,  $p_B = 10$  bar in fig. 4.6. A characteristic torsional mode of the rim can be seen. Furthermore, bending modes of the control arms with high rotation in upper control arm's bushings and strong displacement in the lower control arm front bushing's radial, horizontal direction occur. A 3<sup>rd</sup> order bending mode of the strut with damper assembly can be noted.

### 4.1.7 Relevant Mode #7

For rim B, the relevant mode #7 is depicted in fig. 4.7. Shown for variant 8 - Best-M. Moan-B, coefficient of friction  $\mu = 0.4$  and brake pressure  $p_B = 16$  bar, a 1<sup>st</sup> order torsional rim oscillation is characteristic. In contrast to the other complex modes shown before, relevant mode #7 contains almost no displacements of other sub-components of this suspension and brake system.

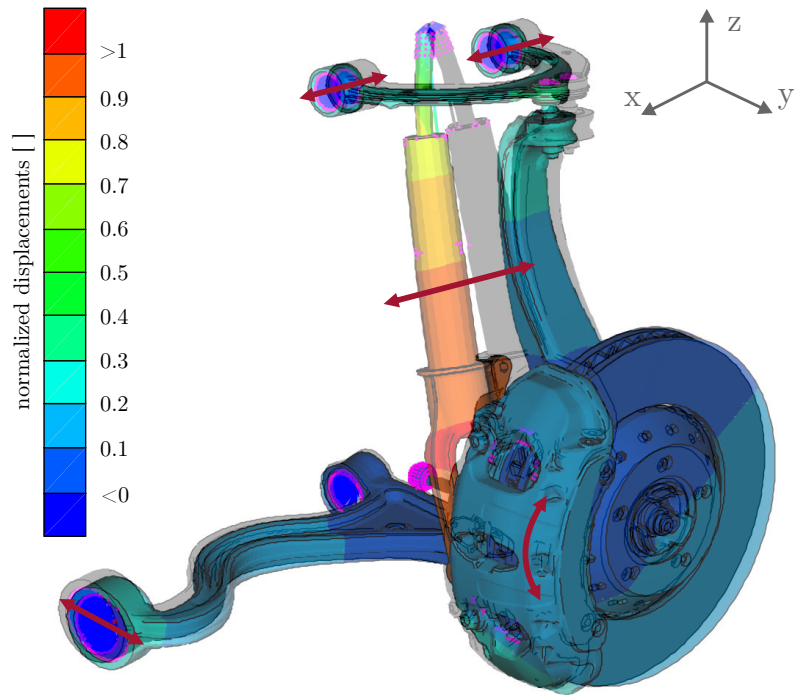
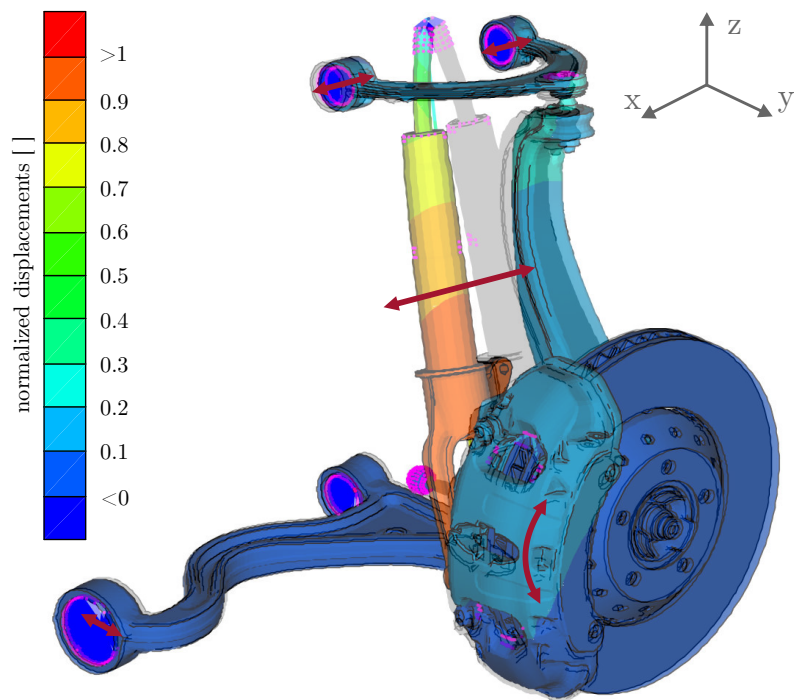
(a) Brake pressure  $p_B = 4$  bar(b) Brake pressure  $p_B = 16$  bar

Figure 4.4: Normalized displacements of unstable mode #4 for variant 3 – Non-lin. Stiff. (table 3.1) with coefficient of friction  $\mu = 0.4$  at vehicle reference speed  $v_{\text{ref}}$

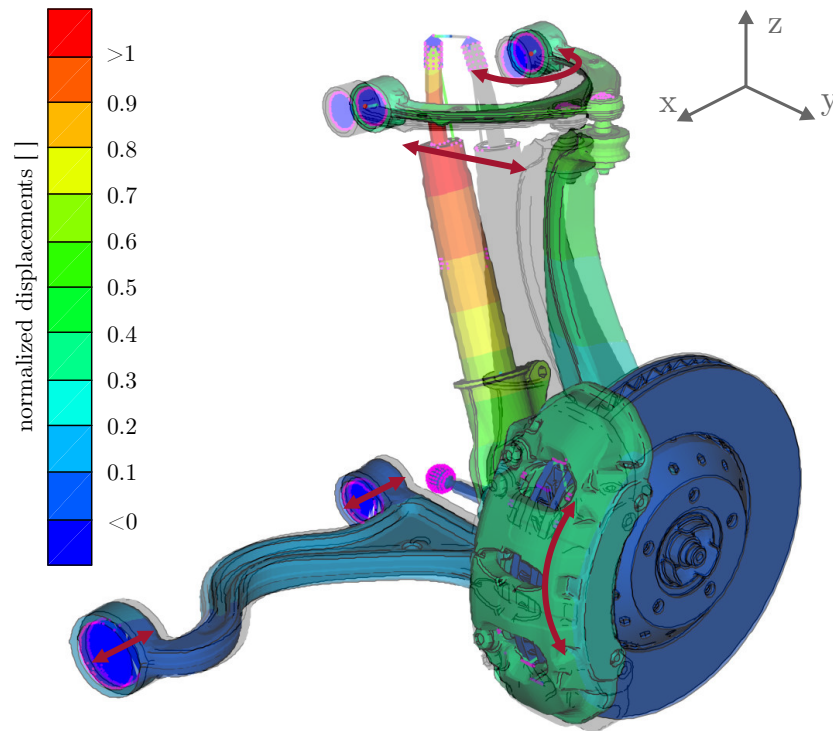


Figure 4.5: Normalized displacements of unstable mode #5 for variant 3 – Non-lin. Stiff. (table 3.1) with parameters  $\mu = 0.45$  and  $p_B = 10$  bar at vehicle reference speed  $v_{\text{ref}}$

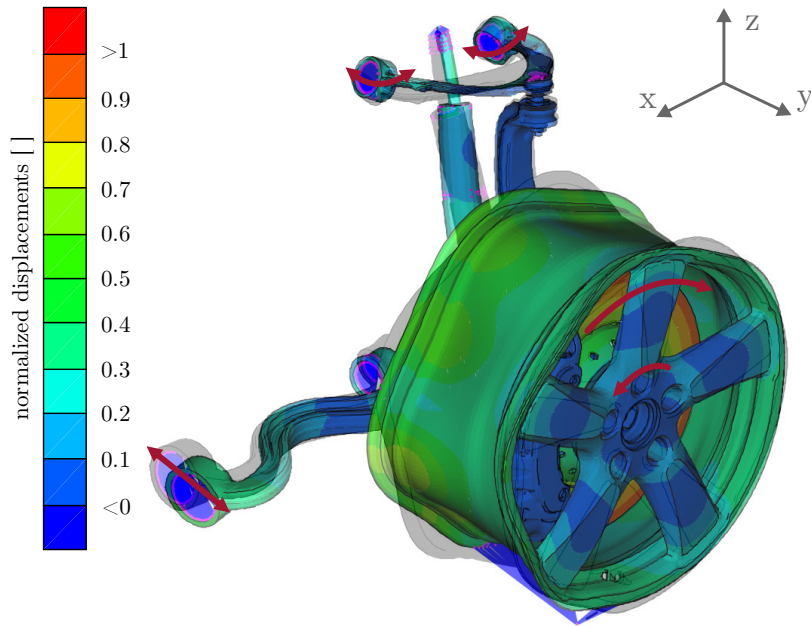


Figure 4.6: Normalized displacements of unstable mode #6 for variant 7 - Best-M. Moan-A (table 3.1) with parameters  $\mu = 0.55$  and  $p_B = 10$  bar at vehicle reference speed  $v_{\text{ref}}$

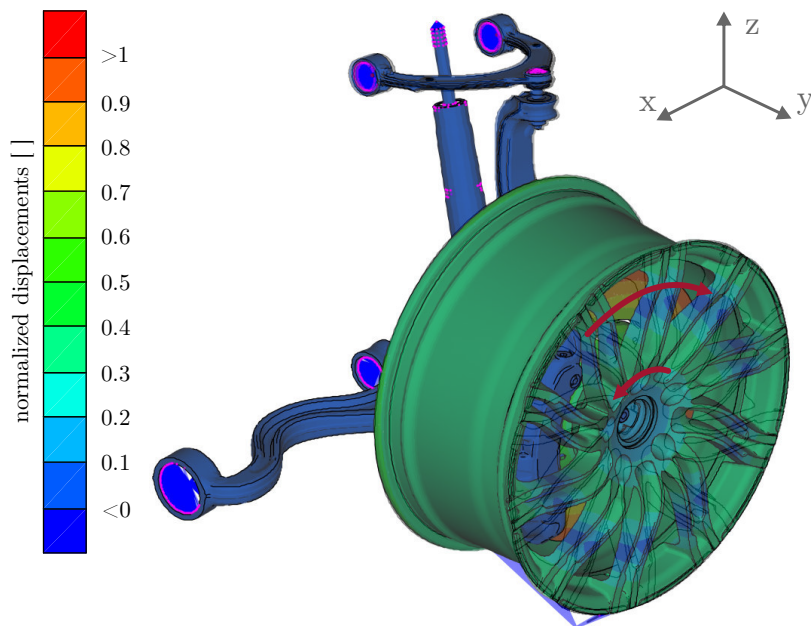


Figure 4.7: Normalized displacements of relevant mode #7 for variant 8 - Best-M. Moan-B (table 3.1) with parameters  $\mu = 0.4$  and  $p_B = 16$  bar at vehicle reference speed  $v_{\text{ref}}$

## 4.2 Stability and Eigenfrequency Results

All relevant and unstable modes and their respective eigenfrequency ranges for the different variants are listed in table 4.2. If a complex mode occurs stable in the whole parameter range, eigenfrequency is written in green, italic letters. Beginning with variant 3 - Non-lin. Stiff, significantly bigger eigenfrequency ranges occur. This behavior is again related to the implemented non-linear parameter dependent bushing stiffnesses.

Table 4.2: Eigenfrequency ranges of relevant and unstable modes, values given in [Hz]

variant \ mode	#1	#3	#4	#6	#7
variant 1 – Squeal-M.	18.2	70.7 – 71.2	<i>82.1</i> – <i>82.4</i>	n/a	n/a
variant 2 – Corr. Geom.	11.7	48.8 – 49.1	<i>69.4</i> – <i>69.6</i>	n/a	n/a
variant 3 – Non-lin. Stiff.	10.9 – 18.3	48.4 – 93.0	66.0 – 72.3	n/a	n/a
variant 4 – Best-M.	<i>10.9</i> – <i>18.4</i>	<i>48.5</i> – <i>93.5</i>	<i>66.1</i> – <i>72.3</i>	n/a	n/a
variant 5 – Best-M. LD	<i>10.9</i> – <i>18.3</i>	48.4 – 93.0	66.0 – 72.3	n/a	n/a
variant 6 – Best-M. no ROT	<i>10.9</i> – <i>18.3</i>	48.4 – 93.0	66.0 – 72.3	n/a	n/a
variant 7 – Best-M. Moan-A	10.9 – 18.3	<i>48.4</i> – <i>93.1</i>	<i>66.0</i> – <i>72.2</i>	562.5 – 563.4	n/a
variant 8 – Best-M. Moan-B	10.9 – 18.3	<i>48.4</i> – <i>93.1</i>	<i>65.8</i> – <i>72.1</i>	n/a	<i>358.7</i>

In the following, multi-dimensional stability diagrams - introduced in [38] - are used to convey further information about frequency and stability of these relevant modes. In this diagram type, the eigenfrequency is printed as a vertical coordinate over the parameter plane of brake pressures and vehicle speeds: A 3D surface is created for each coefficient of friction. Similar to a classical stability map, surfaces are colored according to a stability parameter, here the resulting equivalent viscous damping ratio according to eq. 2.39. Blue areas correspond to an unstable, white areas to a stable working point. Results for zones between the computed parameter points were linearly interpolated.

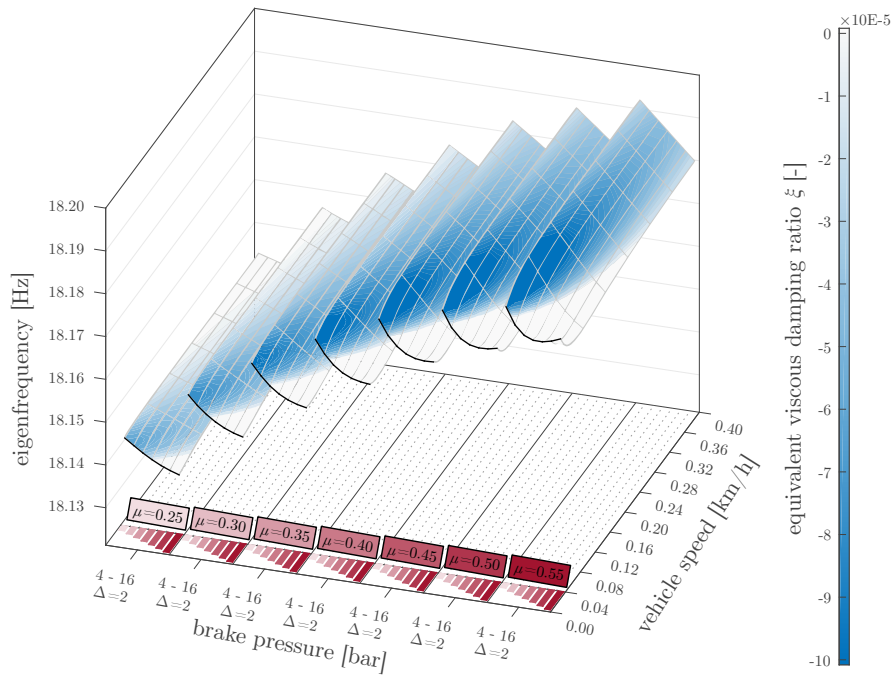


Figure 4.8: Multi-dimensional stability diagram of unstable mode #1 for variant 1 – Squeal-M. (table 3.1)

#### 4.2.1 Unstable Mode #1

Fig. 4.8 shows the eigenfrequency and stability behavior of unstable mode #1 for variant 1 - Squeal-M. In this case, one can observe only minor changes in eigenfrequency. Regarding stability, large parameter areas with unstable (blue) behavior exist. The higher the brake pressure, the more vehicle speed is necessary for the occurrence of an instability.

In fig. 4.9, the multi-dimensional stability diagram for unstable mode #1 of variant 2 - Corr. Geom. is shown. Again, eigenfrequencies show only minor changes. However, when compared to the situation for variant 1 - Squeal-M. in fig. 4.8, one can see that eigenfrequencies of unstable mode #1 decrease essentially. This effect relates to the reduction of bushing stiffnesses, which have high impact on the displacements. In addition, unstable areas shrank significantly from variant 1 to variant 2. This is even more interesting because damping parameters were kept constant: Apparently, bushing stiffness influences both – the resulting eigenfrequency as well as the solution’s stability.

The implementation of non-linear parameter-dependent bushing stiffnesses, beginning with variant 3 - Non-lin. Stiff., brings additional effects. In fig. 4.10, a jump between two different eigenfrequency niveaus of approx. 11.5 Hz to approx. 18.2 Hz can be seen clearly. Actually relating to the brake force, this step starts at lower



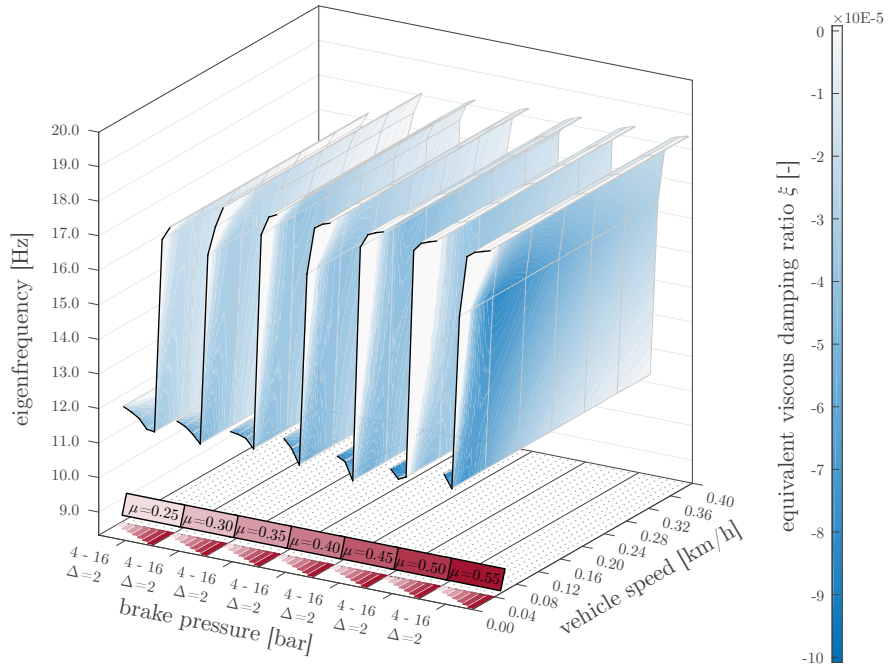


Figure 4.10: Multi-dimensional stability diagram of unstable mode #1 for variant 3 – Non-lin. Stiff. (table 3.1)

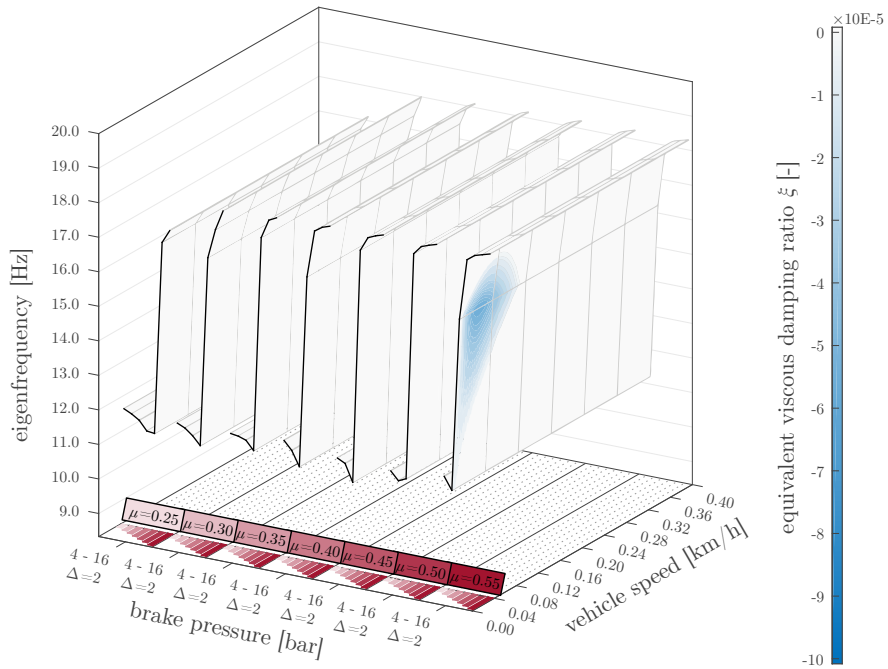


Figure 4.11: Multi-dimensional stability diagram of unstable mode #1 for variant 8 - Best-M. Moan-B (table 3.1)

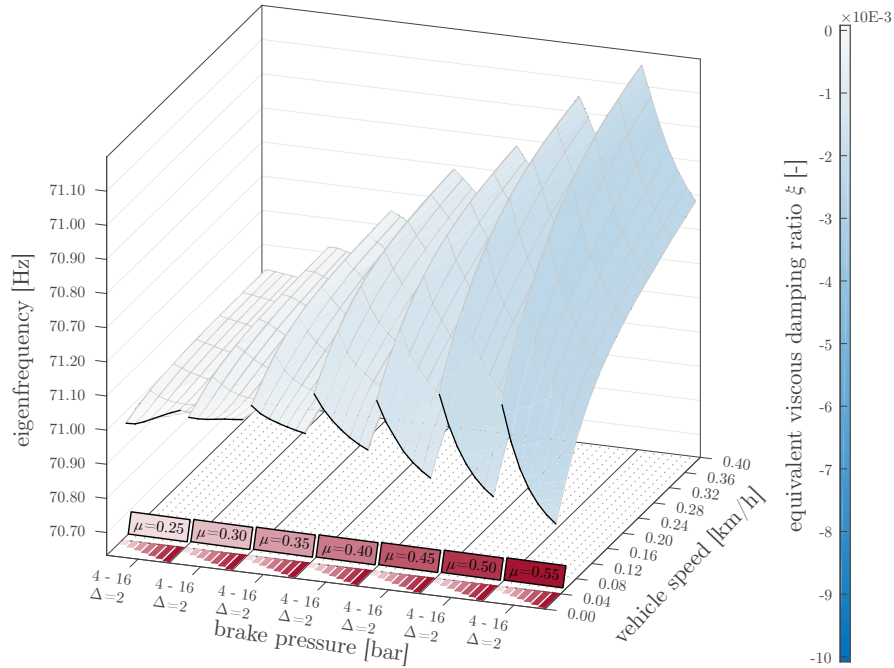


Figure 4.12: Multi-dimensional stability diagram of unstable mode #3 for variant 1 – Squeal-M. (table 3.1)

### 4.2.2 Unstable Mode #3

The multi-dimensional stability diagram for unstable mode #3 and variant 1 - Squeal-M. can be found in fig. 4.12. Similar to unstable mode #1, eigenfrequency is more or less constant. Moreover, areas with negative equivalent viscous damping ratios  $\xi$  can be seen. With higher  $\mu$ , more negative values occur, however, the other parameters provoke only minor changes.

With the lower bushing stiffnesses of variant 2 - Corr. Geom., lower eigenfrequencies result in the multi-dimensional stability diagram of fig. 4.13. Again, unstable areas changed without a change of damping parameters: For high brake pressures, high coefficient of friction  $\mu$  as well as low speeds, unstable behavior is more likely.

The inclusion of non-linear parameter dependent bushing stiffnesses leads to the depiction for variant 3 - Non-lin. Stiff. within fig. 4.14. Analogously to fig. 4.10, a step in eigenfrequencies can be observed. For higher brake pressures, reduced increase of eigenfrequency occurs. What is more, unstable areas arise in zones of high eigenfrequency change.

In the following, unstable mode #3 was stable for all parameter combinations of variant 4, 7 and 8. Similar to unstable mode #1, rim B did not show significant influence on the eigenfrequency behavior.

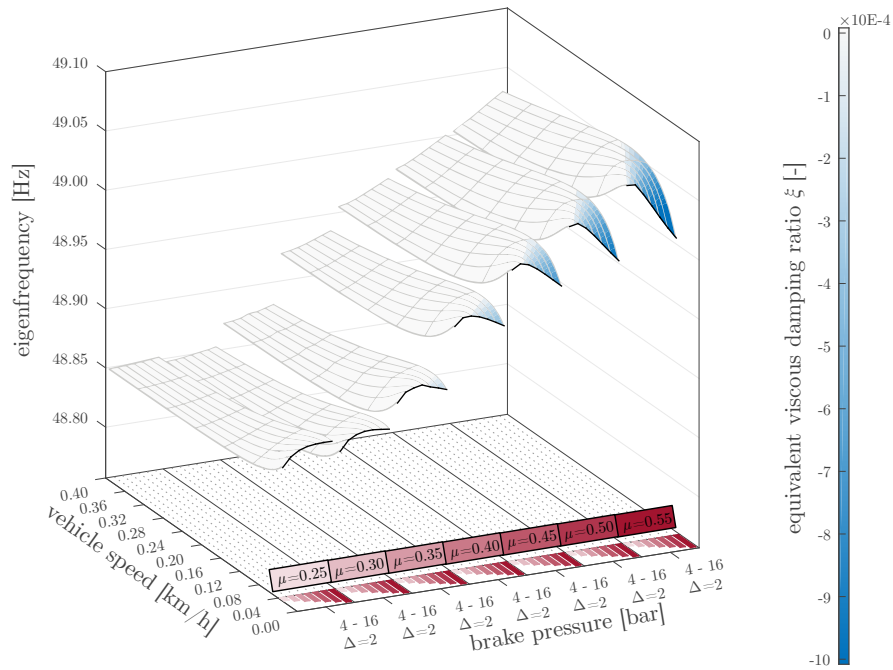


Figure 4.13: Multi-dimensional stability diagram of unstable mode #3 for variant 2 – Corr. Geom. (table 3.1)

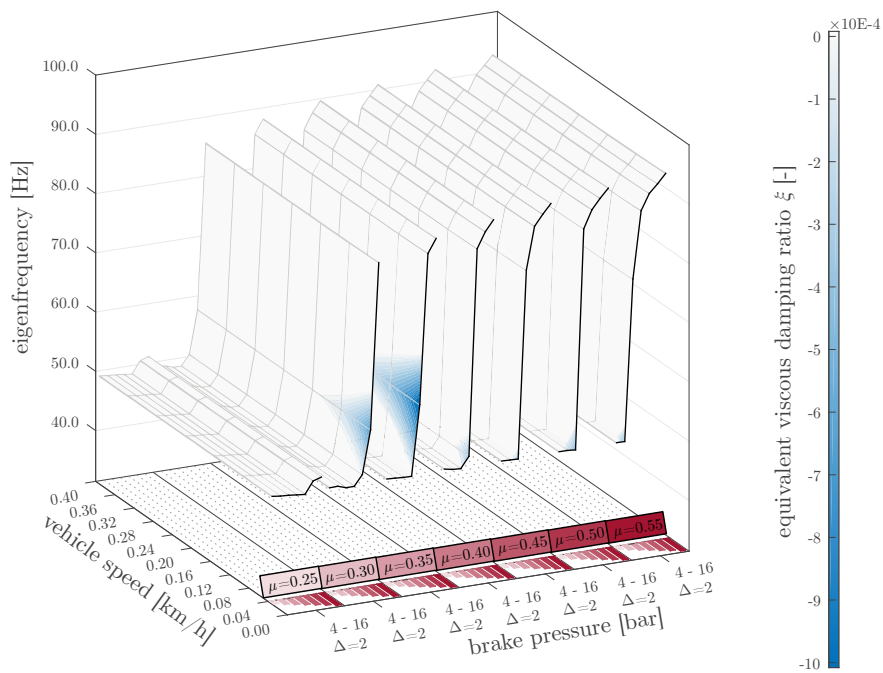


Figure 4.14: Multi-dimensional stability diagram of unstable mode #3 for variant 3 - Non-lin. Stiff. (table 3.1)

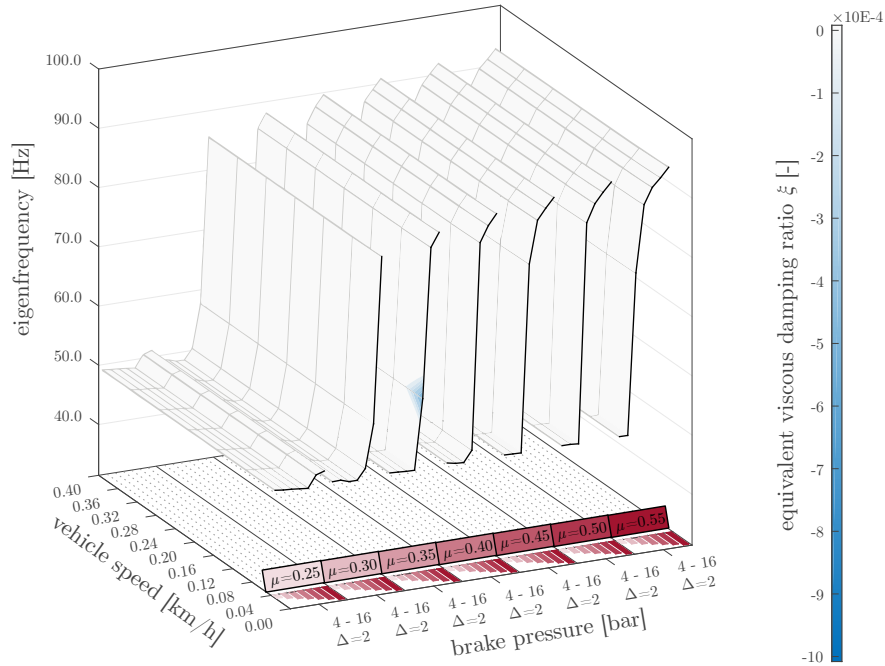


Figure 4.15: Multi-dimensional stability diagram of unstable mode #3 for variant 5 – Best-M. LD (table 3.1)

Finally, the multi-dimensional stability diagram for unstable mode #3 and variant 5 - Best-M. LD is given in fig. 4.15. Compared to variant 3 - Non-lin. Stiff. in fig. 4.14, only minor stability changes can be seen, caused by small changes in elastomer bushing damping. Furthermore, variant 6 - Best-M. no ROT delivered almost identical results for unstable mode #3 in terms of eigenfrequency as well as stability.

### 4.2.3 Unstable Mode #4

Starting again with variant 1 - Squeal-M., the stability diagram in fig. 4.16 shows frequencies of approx. 82 Hz. For low vehicle speeds, the eigenfrequency is slightly increased. Unstable areas do not occur in this case.

For variant 2 - Corr. Geom., the eigenfrequency and stability behavior of unstable mode #4 is given in fig. 4.17. Similar to unstable mode #1 or unstable mode #3, the natural frequencies of this mode are reduced significantly from variant 1 to variant 2 to approx. 69.5 Hz. For very low speeds and high brake forces, small changes of frequency can be seen. Like for variant 1 - Squeal-M., no unstable areas occur here.

Effects of the implementation of non-linear parameter dependent bushing stiffnesses with variant 3 - Non-lin. Stiff. can be seen in fig. 4.18. When the stiffness kink

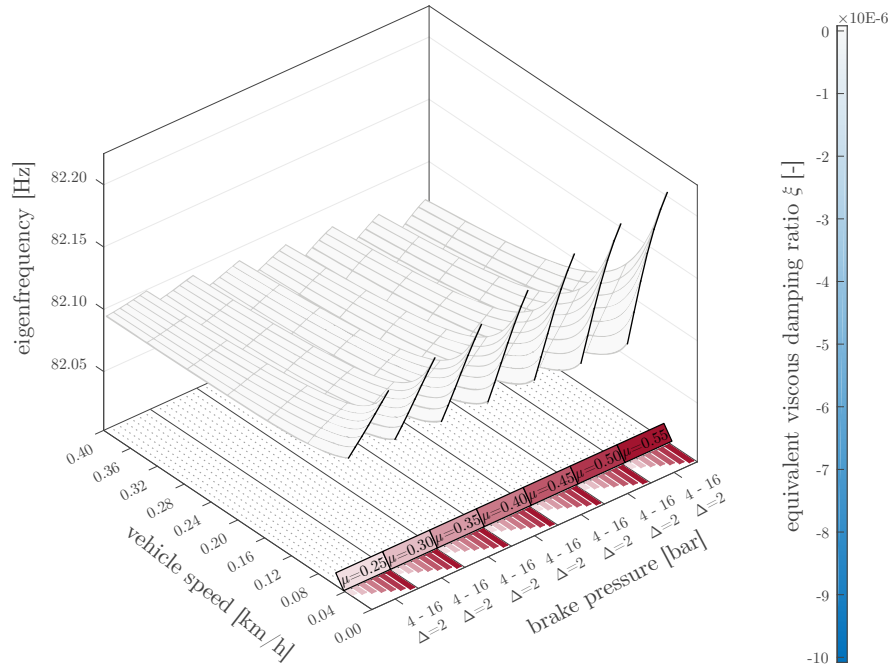


Figure 4.16: Multi-dimensional stability diagram of unstable mode #4 for variant 1 – Squeal-M. (table 3.1)

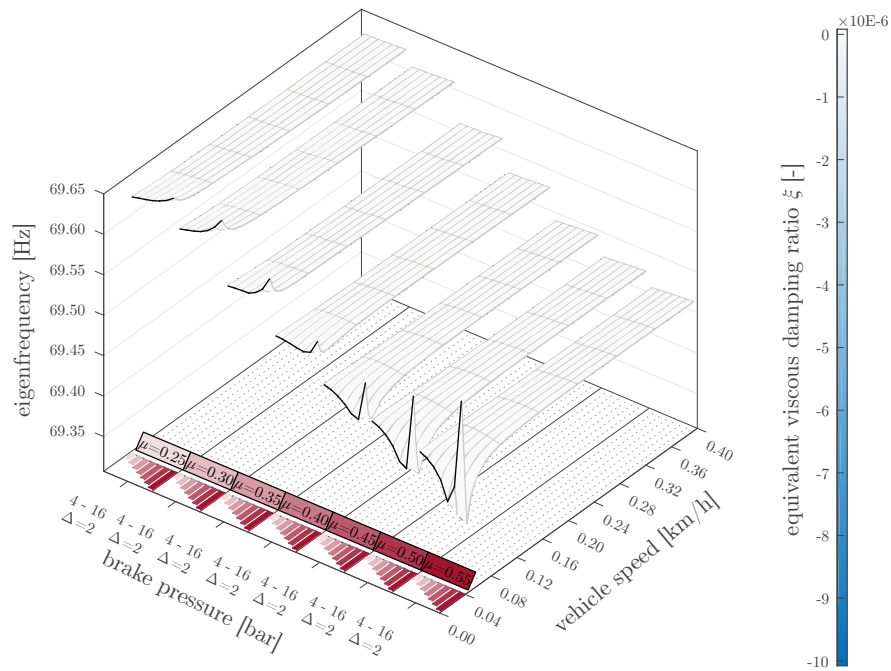


Figure 4.17: Multi-dimensional stability diagram of unstable mode #4 for variant 2 - Corr. Geom. (table 3.1)

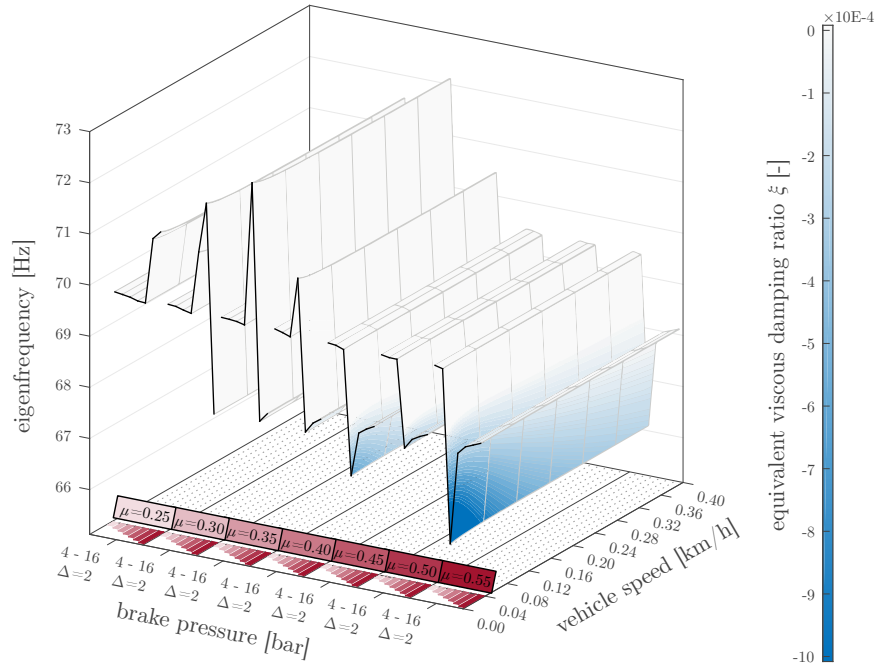


Figure 4.18: Multi-dimensional stability diagram of unstable mode #4 for variant 3 - Non-lin. Stiff. (table 3.1)

appears (see stiffness characteristics in fig. 3.6), eigenfrequency increases at first. With slightly higher brake pressures, a strong decline of frequency in combination with evolving unstable areas can be observed. For even higher brake pressures, the eigenfrequency rises again. Especially the first increase of natural frequency is not found for all coefficients of friction  $\mu$ . However, this possibly occurred due to the rather big brake pressure steps of  $\Delta p_B = 2$  bar.

Because again no unstable areas were found for variant 4 - Best-M., probably due to higher damping, fig. 4.19 shows a resulting multi-dimensional diagram of variant 5 - Best-M. LD. Basically, frequency development is identical to the situation with variant 3 - Non-lin. Stiff. Only minor changes regarding the equivalent viscous damping ratio can be found, caused by changes of damping parameters.

For variants 6, 7 and 8, calculated eigenfrequencies were again almost identical. However, both variant 7 - Best-M. Moan-A and variant 8 - Best-M. Moan-B with their higher number of computed real modes, did not find unstable parameter sets.

Further aspects can be observed by a comparison of unstable mode #3 and unstable mode #4: Whereas unstable mode #3 in fig. 4.15 shows a significant increase and reaches a certain eigenfrequency plateau before and after the stiffness kink, unstable mode #4's eigenfrequency in fig. 4.19 features smaller, more varying changes. This can be explained by the smaller influence of both non-linear parameter dependent

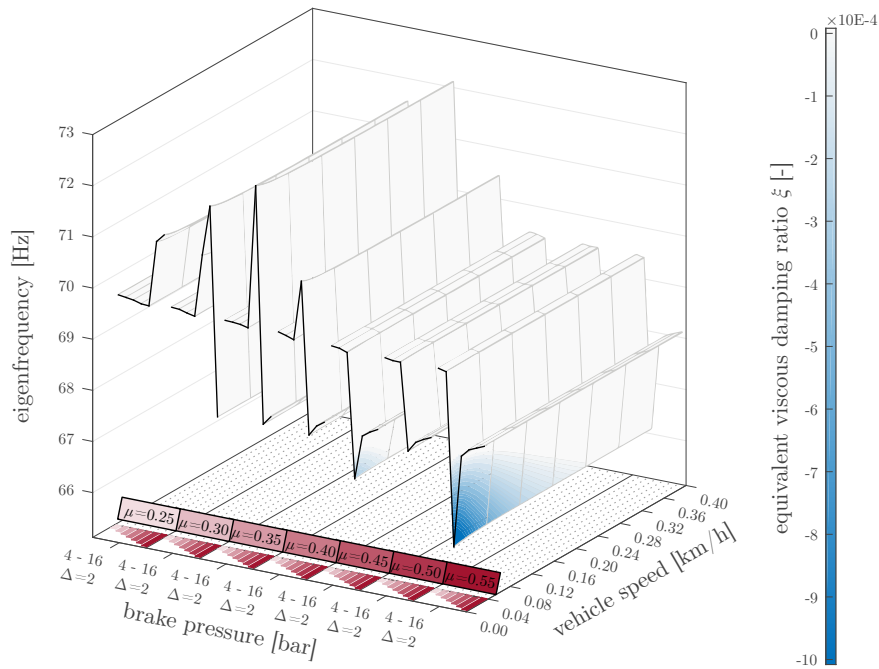


Figure 4.19: Multi-dimensional stability diagram of unstable mode #4 for variant 5 – Best-M. LD (table 3.1)

bushing stiffnesses: E.g. the upper control arm's bushings displace significantly less within unstable mode #4 in fig. 4.4 (a) than within unstable mode #3 in fig. 4.3 (a).

What is more, unstable areas were identified mainly in zones of changing eigenfrequency. Here, both modes relate to similar eigenfrequencies, indicating towards modal coupling behavior.

#### 4.2.4 Unstable Mode #6

The moan-related unstable mode #6 and its frequency and stability behavior can be found in fig. 4.20. It can be observed that frequency changes are of minor scale: Values vary about a mean of approx. 563.2 Hz. Only exception are two sets of  $\mu$  and  $p_B$  with a slightly lower eigenfrequency between 562.5 and 562.9 Hz. One of these sets,  $\mu = 0.55$  and  $p_B = 10$  bar, is also the only parameter combination for which a negative equivalent viscous damping occurred.



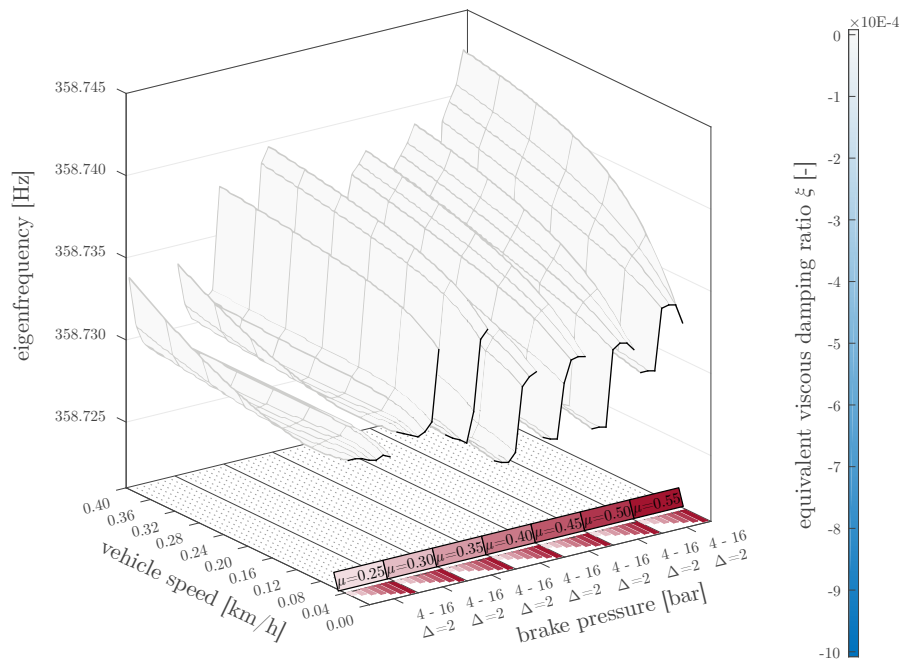


Figure 4.21: Multi-dimensional stability diagram of relevant mode #7 for variant 8 – Best-M. Moan-B (table 3.1)



---

## 5 Validation and Discussion

### 5.1 Phenomenological Validation

In this section, unstable and other relevant mode forms presented and described in chapter 4 are compared to simulative and experimental results found in literature. Main criteria are measured and computed frequency content as well as ODS and displacement results.

The presented results within this work were developed as a part of a multi-year research project. In the course of this, findings from simulative and experimental parts are highly cross-linked. Therefore, validation based on in-house test results with the same axle setting such as in the related publications [38], [51] and [52] are of exceptionally high value.

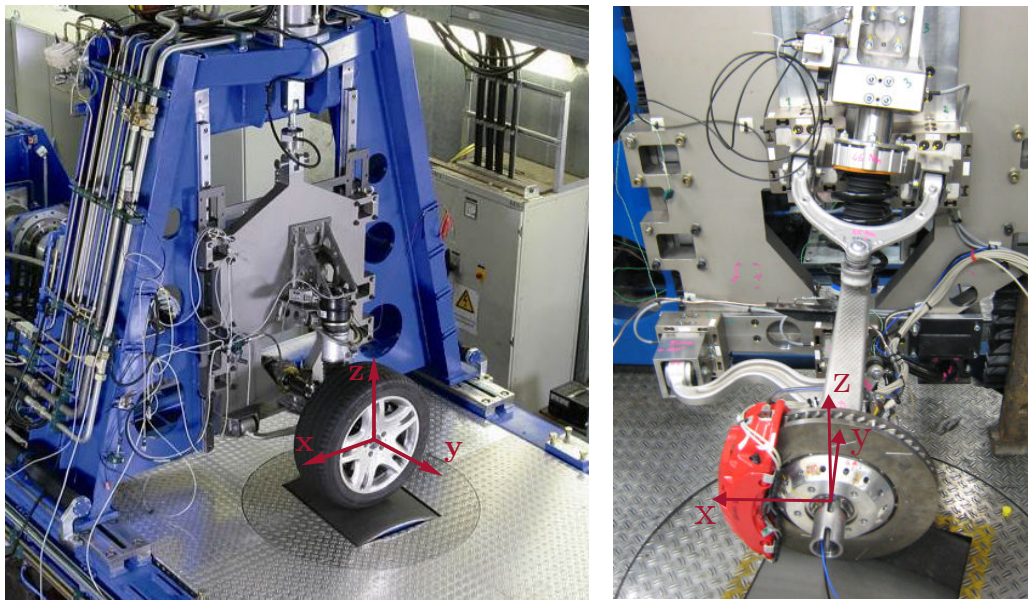
These experiments were performed on a drum-driven suspension and brake test rig, see its basic structure and an exemplary setup within fig. 5.1 (a). A depiction of the investigated double wishbone axle system and the fixed caliper brake is given in fig. 5.1 (b). For better visibility, the wheel was dismounted here.

Within the performed experiments, torque was applied via the speed-controlled drum. Vertical forces due to the vehicle's mass were applied by a hydraulic cylinder. With the corresponding brake pressure, correct pretension of elastomer bushings was ensured in this setting. In the following, the longitudinal acceleration (x-direction), measured at the upper end of the inner brake pad's backing plate and sampled with 10 kHz, is used for validation. A depiction of the sensor position can be found within fig. 5.2.

In addition to the in-house tests, [45] represents the work of a project partner. Again, almost identical components were tested here. Hence, validation based on this publication is of high relevance too.

#### 5.1.1 Creep Groan Related Unstable Modes

As stated within chapter 2, many experts agree on the stick-slip effect as the cause of creep groan phenomena. Due to difficulties regarding the linearization of frictional forces based on Coulomb's law, CEA is not able to give a definite prediction about the occurrence of 'unstable' creep groan oscillations for certain parameter sets. However, the behavior of occurring natural oscillations during slip phases, which



(a) Exemplary test setup, adapted from [38]

(b) Investigated suspension and brake system without wheel

Figure 5.1: Drum-driven suspension and brake test rig of the Institute of Automotive Engineering - Graz University of Technology.

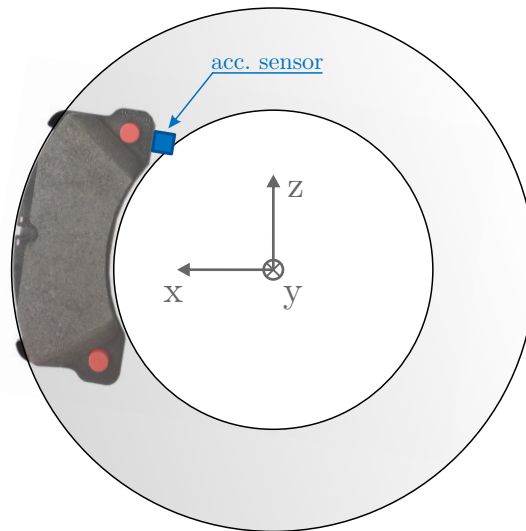


Figure 5.2: Position of the utilized acceleration sensor on the upper end of the inner brake pad's backing plate

are most likely of large influence on this low-frequency phenomenon, was computed and can now be compared to experimental and simulative results, as proposed in [38], a publication of the author's research group.

According to the classification of brake NVH phenomena in fig. 2.15, all relevant unstable modes in a creep groan-related frequency range are validated in the following.

#### 5.1.1.1 Unstable Mode #1

Regarding frequency, unstable mode #1 was the lowest relevant mode found during the simulative investigations with a range of 10.9 – 18.4 Hz. Characteristically, a forward/backward rolling of the wheel with movement in the control arm's elastomer bushings was found here.

With a fundamental frequency of 18 Hz, creep groan was found at the upper end of this frequency range for this axle setting within the related work [38], see also fig. 5.3. Additionally, 20 Hz creep groan could also be detected with this axle setting, see [52]. In both cases, no ODS measurements are published yet, however, objective and subjective investigations confirm a certain amount of longitudinal movement of the whole axle system.

Furthermore, [39] presents similar results: Here, fundamental frequencies of 18 Hz and 22 Hz were measured for stick-slip transition in vehicle dynamometer tests. Longitudinal suspension and axle system vibrations were found in an ODS measurement. Interestingly, changes of the chassis setup and rigidity led to a change in stick-slip frequency, which is similar to the simulated behavior of unstable mode #1: Here, changes of bushing stiffnesses have shown direct impact on the eigenfrequency of its longitudinal displacements. However, in contrast to the simulated double wishbone suspension system, [39] presents results of a MacPherson front axle.

Within [25], a double wishbone axle combined with a floating caliper brake was investigated. Here, a 25 Hz mode was found by a spectral ODS of a corner model without tire and rim. Higher frequencies compared to unstable mode #1 could be explained by the missing mass of the wheel. Similar to unstable mode #1, longitudinal movement of the axle components was stated for the performed experimental test as well as for a modal analysis of a Multi-Body model. With 31 Hz, the computed frequency within [25] is significantly higher than unstable mode #1's eigenfrequency.

#### 5.1.1.2 Unstable Mode #3

As unstable mode #2 was considered irrelevant, the unstable mode #3 with frequencies from 48.4 – 93.5 Hz is validated next.

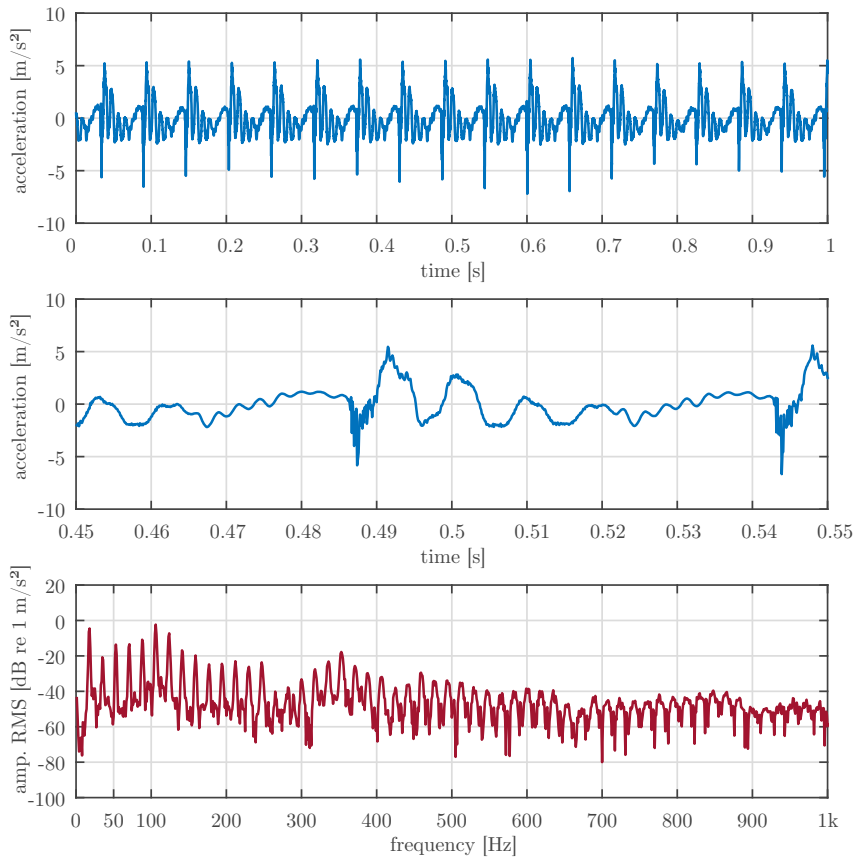


Figure 5.3: Time signal and frequency plot of measured pad accelerations in vehicle's x-direction during 18 Hz creep groan at  $p_B = 10$  bar and  $v_{\text{veh}} = 0.06$  km/h, adapted from [38]

Regarding experiments with according axle settings, creep groan events with frequencies of 63 Hz and 95 Hz were found within [38] and [52], see also fig. 5.4. These different frequencies are of very high interest as different upper control arms were used in both experimental tests. Because unstable mode #3 shows high displacements especially in the bushings of the upper control arm, the sensitivity of the test results regarding these parts clearly confirms simulation results.

Again, no ODS can be compared to the displacements found by simulation. However, high displacements of the upper control arm bushings in their longitudinal direction and of the lower control arm front bushing in its radial, horizontal direction were subjectively detected as explained within [38]. This further supports the computed displacement behavior of unstable mode #3, see fig. 4.3 (a) and (b).

[27] speaks of a characteristic rotation of the wheel carrier caused by the tangential stick-slip excitation. As this work investigated a MacPherson front axle, a bending

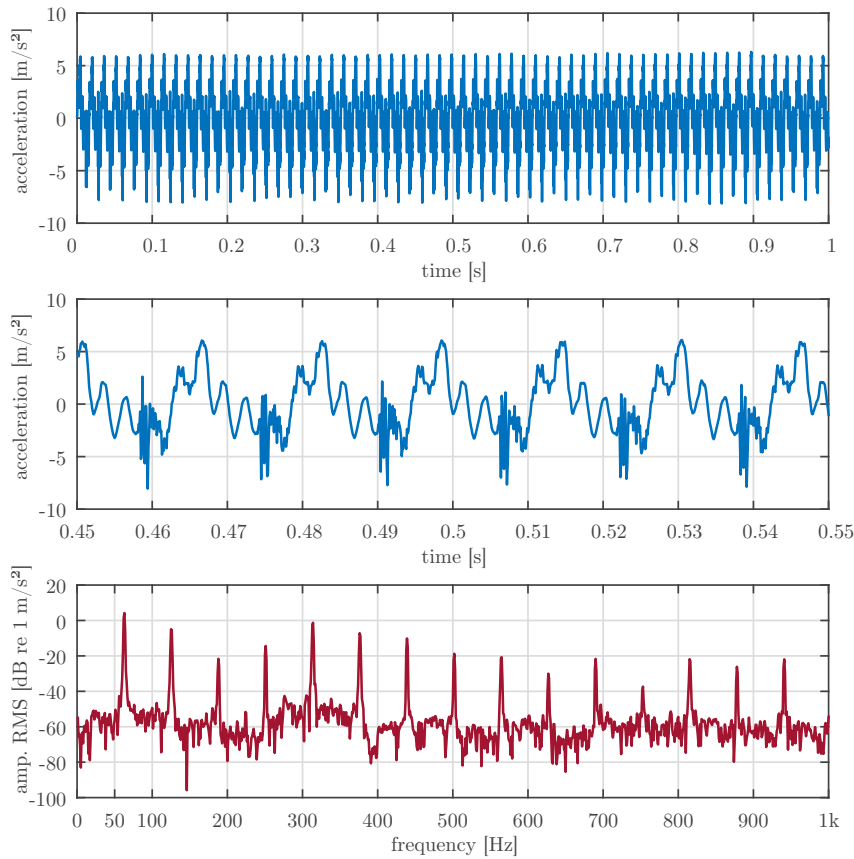


Figure 5.4: Time signal and frequency plot of measured pad accelerations in vehicle's x-direction during 63 Hz creep groan at  $p_B = 8$  bar and  $v_{\text{veh}} = 0.08$  km/h, adapted from [38]

mode of the strut was excited too. Nevertheless, this is comparable to the double wishbone suspension of the setting considered in this work: Within unstable mode #3, the rotation of brake caliper and wheel carrier caused by stick-slip transitions simply provokes the characteristic longitudinal displacement of the upper control arm instead of a bending of a MacPherson strut.

Another ODS analysis carried out with a MacPherson front axle on a dynamometer test rig can be found in [60]. With 96 Hz, again a first bending mode of the strut was found during creep groan. With respect to the stated graphical depiction of displacements, rotation of the caliper and wheel carrier similar to unstable mode #3 seems likely, as the lower control arm exhibits forward/backward oscillations in opposite phase to the strut's connection to the wheel carrier.

[39] did not explicitly state similarities to unstable mode #3. However, a strong peak at about 50 Hz can be seen within one frequency plot of the full vehicle dynamometer

creep groan tests. Again, a MacPherson axle was investigated in this case.

With a measured frequency of 41 Hz, [25] found a very similar mode with its corner tests of a double wishbone front axle without rim and tire. Rotation of caliper and wheel carrier and a resulting movement of the upper control arm can be seen clearly. Within its simulations, the same mode was found with an eigenfrequency of 49 Hz. Even though the frequencies are clearly different, simulated displacements fit well with unstable mode #3.

### 5.1.1.3 Unstable Mode #4

With frequencies from 66.0 – 82.4 Hz, unstable mode #4 featured a characteristic axial bending mode of the spring with damper assembly. Within the related studies [38] and [52], both creep groan frequencies already mentioned for unstable mode #3 were found. Similarities seem possible not only due to the similar frequency range, but also because computed mode displacements of both eigenmodes contained parts of the respective other complex mode. Again, axial movement of the spring with damper assembly was claimed to be subjectively of high amplitude in [38].

As the function of the strut within a MacPherson front axle is clearly different from the function of the spring with damper assembly in a double wishbone suspension, a comparison of unstable mode #4 with results of [27] or [60] is not meaningful. In addition, no deflections of the spring with damper assembly within the tests of a double wishbone axle in [25] were observed during ODS measurements. Therefore, a qualitative validation of unstable mode #4 was not possible, no references to an oscillation pattern similar to fig. 4.4 were found in literature.

## 5.1.2 Moan Related Unstable and Relevant Modes

According to chapter 2, moan has recently been stated as a brake NVH phenomenon related to dynamic instabilities and mode coupling. Therefore, computed results of variant 7 - Best-M. Moan-A and variant 8 - Best-M. Moan-B, both optimized for the corresponding frequency range, should deliver sufficient results. Again, only a few literature sources with relevant ODS measurements for this kind of suspension system were found. Nevertheless, the already mentioned investigations on almost exactly the same system within [38], [45] and [51] represent high value for validation.

### 5.1.2.1 Unstable Mode #6

As already shown in chapter 4, the unstable mode #6 with a frequency of approx. 563.2 Hz contains a torsional mode of the rim as well as bending modes of control arms and spring with damper assembly, see fig. 4.6. As stated in the related work [38], no moan phenomena were detected with this rim design – rim A – on the vehicle's corner test bench.



Figure 5.5: Laser-vibrometry measurements of rim deflections during brake moan, from [45]

However, personal correspondence with the main author of [45], who also performed experimental moan tests on the identical axle, confirmed the computed eigenfrequency to be almost identical with a moan frequency ‘enforced’ on test bench. Moreover, the torsional rim mode displacements were also claimed correct for this mode, which was found non-critical in the vehicle environment as well by the author of [45].

Differently than described in [6], the found unstable parameter range was very small – parameters had a very high influence on the occurrence of the instability. This stands in contrast with the theory of a dynamic instability.

#### 5.1.2.2 Relevant Mode #7

Similar to unstable mode #6, a torsional rim mode with an eigenfrequency of approx. 358.7 Hz was found with the differently designed rim B. Within [45], laser vibrometry measurements of an almost identical axle system revealed a torsional rim mode as the critical displacement during brake moan action, see the depiction in fig. 5.5. A comparison with fig. 4.7 reveals high similarity. However, the dominant frequency was found with 512 Hz as a different rim was used.

With the actual rim B, brake moan was found with 386 Hz during corner tests within [38]. See also the time and frequency plot in fig. 5.6.

Unfortunately, CEA did not find unstable parameter combinations of relevant mode #7: Even for an increased parameter range of coefficients of friction up to  $\mu = 0.8$ , all computed equivalent damping ratios were positive.

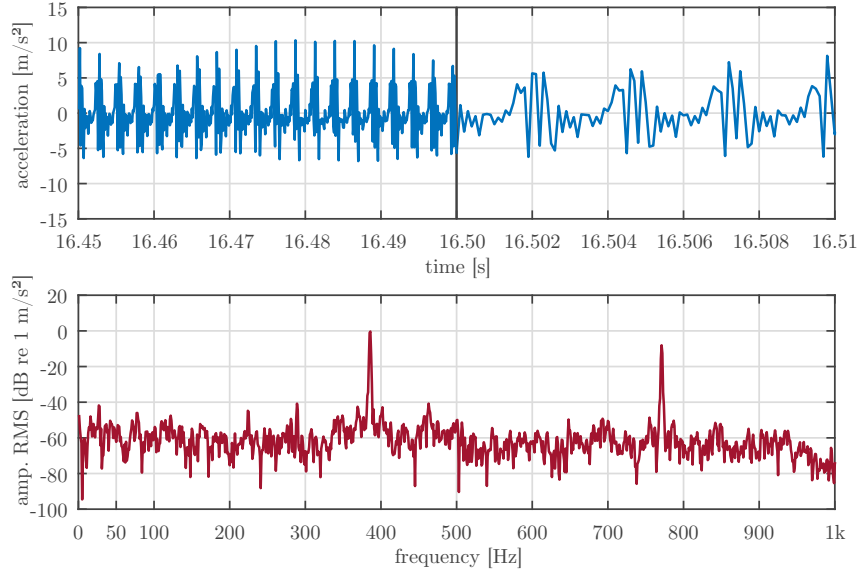


Figure 5.6: Time signal and frequency plot of measured pad accelerations in vehicle's x-direction during 386 Hz moan at  $p_B = 13.15$  bar and  $v_{\text{veh}} = 0.08$  km/h, adapted from [38]

## 5.2 Discussion of the Results

In this section, final results and the validation of simulative findings shall be discussed separately for creep groan and moan related eigenmodes

### 5.2.1 Creep Groan Related Unstable Modes

Because of the strong simplifications made during friction linearization, CEA was already stated to be incapable of completely predicting creep groan behavior within section 2.5.5 and the related work [38]. Nevertheless, the simulation of frequency content during slip phases should be possible, this is therefore discussed subsequently.

In general, computed displacements and frequencies of the relevant unstable modes #1 and #3 are in good correspondence with experiments and simulations found in literature and in related in-house tests accompanying this work. Behavior similar to unstable mode #4 was not explicitly stated in literature.

Based on the validation within the previous section, creep groan oscillations could be distinguished further into two different phenomena: A lower frequency phenomenon at approx. 10 – 30 Hz and a higher frequency phenomenon at approx. 40 – 100 Hz. Bearing in mind the procedure of pretension (stick phases) and damped natural oscillation (slip phases) stated in chapter 2.4.1.1, the found and evaluated eigenmodes could play an important role here.

For the *lower frequency creep groan* phenomenon at approx. 10 – 30 Hz, forward-backward movement and frequency of unstable mode #1 could directly relate to the stick-slip transition. High consistence with test bench results and literature statements is given here. Additionally, a close look into [52] reveals the occurrence of this phenomenon especially for higher brake pressures. In terms of real-world creep groan during disengagement of the brake in standstill on an inclined road, this would relate to situations with rather steep tracks.

For the *higher frequency creep groan* phenomenon at approx. 40 – 100 Hz, a different effect is revealed by literature and complex mode simulation: Whereas MacPherson axles show high 1<sup>st</sup> order bending of the strut, double wishbone axles perform longitudinal oscillations of upper control arm and spring with damper assembly excited by the stick-transitions and the therefore rotating caliper and wheel carrier. Unstable mode #3 and unstable mode #4 could make up for high shares of the resulting oscillation. Comparison with the according test bench results in [52] connects this higher frequency creep groan with lower brake pressures and very small speeds.

All three creep groan-relevant unstable modes #1, #3 and #4 contained mainly rigid body displacements of the single components, with the exception of the spring with damper assembly. These components deformed mainly within their elastomer bushings, which also explains the bushings' significant influence.

Eigenfrequency as well as computed stability behavior were affected largely by the elastomer bushings' stiffness. Especially the implementation of non-linear parameter-dependent stiffnesses for the lower control arm's front bushing in horizontal direction and for both upper control arm bushings in axial direction – spring elements ②, ④ and ⑤ in fig. 3.5 and fig. 3.6 – has shown strong impact. Frequency steps in unstable mode #1 and #3 and changes of the equivalent viscous damping ratio resulted.

The elastomer bushing's damping parameters affected mainly the occurrence of unstable parameter combinations, as a comparison of the results for variant 4 - Best-M. and variant 5 - Best-M. LD has shown. Resulting eigenfrequencies, however, were less influenced by damping. Implementation of damping according to the best of the author's knowledge made relevant modes appear stable, see also table 4.2. Hence, further efforts should be taken to correctly depict the damping behavior of elastomer bushings. As the analysis of component test data in chapter 3.1.2.2 has shown, parameters such as vibration amplitude or frequency can have essential influence on the amount of dissipated energy in the rubber material. Therefore, a strong coupling between component tests, vehicle tests and simulative investigations could be crucial.

What is more, a review of the resulting eigenfrequency ranges within table 4.2 reveals a strong influence of the computed modal basis on the occurrence of unstable modes. With the higher frequency limit for real modes  $f_{r,lim} = 2.5$  kHz, moan-relevant simulations of variant 7 - Best-M. Moan-A and variant 8 - Best-M. Moan-B computed unstable parameter combinations for unstable mode #1 but not

for #3 and #4. This stands in contrast with the results for variant 5 - Best-M. LD, where unstable mode #1 occurs always stable and unstable modes #3 and #4 both become unstable for some parameter combinations. Here, a frequency limit for real modes  $f_{r,\text{lim}} = 1$  kHz was applied. However, frequency content showed almost no changes. These results contradict CEA's ability of creep groan prediction.

Additionally, influences of the rim design on creep groan relevant mode forms were rather low. A frequency comparison of unstable modes #1, #3 and #4 in table 4.2 reveals only minor eigenfrequency changes between variant 7 - Best-M. Moan-A and variant 8 - Best M. Moan-B. Nevertheless, conclusions about the whole wheel's influence cannot be drawn as the tires were modeled with respect to identical overall mass moment of inertia about the wheel axis for both rim designs.

Displacement, eigenfrequency and stability results changed only very little from variant 5 - Best-M. LD to variant 6 - Best-M. no ROT, see also table 4.2. This supports the conclusion of the system matrices' analysis in chapter 3.2: The influences of modal geometric stiffness matrix  $\widetilde{\mathbf{K}}_G$ , modal convective stiffness matrix  $\widetilde{\mathbf{K}}_C$  and modal gyroscopic matrix  $\widetilde{\mathbf{D}}_G$  are very small for the creep groan- and moan-relevant low vehicle speeds  $v_{\text{veh}}$  due to their linear or quadratic dependence on the respective rotational speeds. In contrast to [34], the anti-metric gyroscopic terms did not alter the stability behavior essentially. Moreover, computation time was reduced by about 16 % by this measure.

Finally, it can be noted that all three relevant unstable creep groan-related complex modes featured high relative tangential displacement between brake disk and pads. Therefore, a tangential stick-slip transition disk and pads would be able to excite these modes directly. Vice-versa, modes without this characteristic displacement probably cannot be excited to high amplitudes by a change from stick to slip.

### 5.2.2 Moan Related Unstable and Relevant Modes

Within chapter 2.5.5 and the related work [38], moan as a dynamic instability was considered to be predictable by means of CEA.

In terms of the computed torsional rim modes of moan oscillations for both rim A and rim B, this assumption has been partly true: The phenomenological validation of moan in chapter 5.1.2 has confirmed high influences of these rim modes in real life, frequencies were found different but comparable too.

However, the method was not able to predict stability correctly with the used model. Variant 7 - Best-M. Moan-A with the rim robust in real-life was computed unstable for one parameter set, whereas variant 8 - Best-M. Moan-B with the actually critical rim did not become unstable for any set of parameters.

It can be assumed that the simulated models do not depict the reality accurately enough. Especially the mass, stiffness and damping characteristics of the tire, probably also of high importance for the torsional rim mode, are modeled in a rather

simple manner. Therefore, improvement of the tire model – based on measured parameters, if possible – could be essential for moan prediction.

Nevertheless, both torsional modes of rim A and rim B featured eigenfrequencies very similar to the measured ones, which insinuates to be on the right path with this method.

### 5.3 Shortcomings and Further Potential of the Method

As discussed in the previous chapters, prediction of unstable behavior was not sufficient for both moan and creep groan.

However, important conclusions were still drawn from the CEA results and the phenomenological validation with literature results. Certainly, quality of the outcome of this linearized computation method is directly influenced by the model which is input. Therefore, further improvement for the prediction of moan-related instabilities and the simulation of modal components of creep groan oscillation could be reached by realizing the following issues:

- Implementation of additional non-linear parameter dependent stiffnesses, based on accurate and complete component test data.
- More sophisticated damping parameters: Due to their high influence on the occurrence of instabilities, adjustments and fine-tuning have to be made for a correct moan evaluation. This includes static as well as dynamic effects of elastomer bushings and other components. Again, strong cross linking with component test data is recommended. Therefore, detailed information about mass distribution, stiffness and damping behavior needs to be acquired.
- Improved tire model: Especially regarding moan phenomena, a more detailed and accurate tire model seems necessary as interaction with torsional rim modes could be possible.
- Influence of vehicle speed: A higher range regarding vehicle speeds  $v_{veh}$  could be necessary especially for moan evaluation, as this phenomenon could also occur at higher speeds.

Furthermore, CEA could still be used for creep groan issues in terms of an investigation of probably critical modal content. Because of the possible excitation by a stick-slip transition, complex modes could be considered critical based on the relative displacement between pad linings and disk. E.g., an averaged tangential relative displacement of all contact nodes could be compared to a critical, reasonably chosen threshold. In the following, only modes with higher relative displacement than this threshold would be relevant for further analysis, such as a transient analysis based on modal coordinates.

## 5.4 Recommendations for Transient Creep Groan Simulation

Even though results were not able to predict unstable behavior, prediction of moan is considered possible by means of CEA. Therefore, recommendations in terms of modeling quality are treated in chapter 5.3, *Shortcomings and Further Potential of the Method*, for this phenomenon.

By contrast, creep groan cannot be predicted sufficiently by CEA. Hence, development of according transient approaches could lead to the solution of this problem. Thus, recommendations are stated only for the transient simulation of creep groan here.

In this context, model size is essential for a transient simulation approach: Usually, a very high number of parameter sets needs to be computed in order to cover many different driving conditions (here: 4459). Therefore, it is important to reduce the number of DOFs to a very low number.

This implies that components of more influence should be modeled with higher detail than components of less influence on creep groan occurrence and severity. Many parts, such as e.g. wheel carrier, caliper or the rim, could sufficiently be modeled by rigid mass and rotatory inertia points. Other parts, such as e.g. the spring with damper assembly, showed lower order bending in the relevant unstable modes presented in chapter 4 and should therefore be modeled in a way which enables this kind of displacement. Simple beam models could already be able to depict the behavior of such components sufficiently. [56] uses a similar approach: With a Component Mode Synthesis<sup>1</sup> method based on the procedure introduced by Craig and Bampton, substructuring of the model is performed and suspension components can only fulfill displacements of the rigid body and its first eigenmodes defined by a chosen frequency limit.

Furthermore, the necessary number of contact nodes could be rather low, as typically a ‘global’ stick or slip occurs during creep groan: This means, almost the whole contact surface of the pad sticks or almost the whole contact surface slips at one moment. However, the author recommends to start with a rather fine resolution of contact nodes – further reductions for a more time efficient, economic computation should only follow if their influence is clearly found to be low.

Elastomer bushing stiffnesses and dampings have shown great influence on CEA results. Especially the non-linear stiffness behavior could lead to typical super-harmonic content within the transient oscillations. Thus, bushing parameters are of high importance for a transient model.

As it was found for the axle system investigated in this work, not all bushings operate in their non-linear stiffness zone during creep groan action. Therefore, the

---

<sup>1</sup>CMS

relevant bushings need to be identified at first. This can be done by evaluation of the occurring bushing forces and displacements during creep groan and a comparison with corresponding component test data. Certainly, a simple linear static calculation of the axle system's forces based on rigid parts would be less effort. However, in the author's opinion this could probably be not accurate enough and measured and verified forces generally deliver better results.

Unfortunately, these measurement values might not be available at early stages of the design process. Then, selection of non-linearly implemented bushing stiffnesses could be done based on experience.

As damping elements influence the oscillation amplitudes, these parameters should be implemented with high care too. Cross-reference to component test data could also turn out to be crucial here.

The inclusion of dynamic effects for damping and stiffness of elastomer bushings would be another step towards a sufficient model. Again, strong interaction between experimental tests and simulation is desirable.

For computation itself, implicit as well as explicit schemes are available. As the conditionally stable explicit schemes generally have advantages in terms of non-linearities such as contact solution and regarding convergence, the author would recommend to utilize one of these schemes. Furthermore, the implementation of predictor mechanisms for static deflections during the system's pretension could reduce the necessary computation duration of each loop.

Analysis and evaluation of the huge amount of time-domain results could further be enhanced similar to the frequency-based approach in [52], where the frequency plot is searched for creep groan characteristics automatically.



---

## 6 Conclusions

Within this work, usage of the Complex Eigenvalue Analysis was investigated for the low-frequency brake noise, vibration and harshness phenomena creep groan and moan. The main assumption, which was stated in a publication that originated from the work on this issue, was that a prediction of moan oscillations should be possible whereas real-life creep groan oscillations could not be foreseen by Complex Eigenvalue Analysis: Only for the basic oscillation content of damped natural oscillations during global slip-phases between linings and disk, meaningful results should be found.

The computation and careful evaluation of eight different variants of a vehicle's front corner with double wishbone suspension and fixed caliper brake in a Finite Element environment has revealed this main assumption as partly true. A validation based on related experimental tests and literature statements regarding Operating Deflection Shapes and frequency content acknowledged the method's fundamental incapability of creep groan prediction and presumptions concerning oscillations during slip phases. However, moan was not predicted correctly either: A variant known to be robust in real-life was computed to be critical and vice versa.

**Concerning creep groan**, three relevant unstable modes were found, with eigenfrequencies in the range of 10.9 – 18.4 Hz, 48.4 – 93.5 Hz and 65.8 – 82.4 Hz. Based on the experimental and simulative investigation, it is suggested that creep groan is further distinguished in low-frequency and high-frequency creep groan as different basic displacement patterns relating to the eigenmodes were found.

*Low-frequency creep groan*, approx. in the range of 10 – 30 Hz, mainly contains longitudinal displacements of the whole axle system within the elastomer bushings relating to a forward/backward rolling of the wheel. The stick-slip transition frequency is here related to the above mentioned very similar first unstable mode with 10.9 – 18.4 Hz.

*High-frequency creep groan*, approx. in the range of 40 – 100 Hz, shows oscillations excited by a rotation of wheel carrier, caliper and pads about the wheel axis, which are caused by the stick-slip transition. Depending on the axle setting, these further stimulate bending within the strut for a MacPherson axle system, or, as within the simulations of a double wishbone front axle of this work, they drive longitudinal oscillations of upper control arm within its bushings together with bending of the spring with damper assembly. Corresponding eigenmodes were simulated: A rotation of the wheel carrier combined with axial displacement of the upper control arm

was found in the second unstable mode with 48.4 – 93.5 Hz. For the third unstable mode within 65.8 – 82.4 Hz, 1<sup>st</sup> order bending of the spring with damper assembly was dominant.

In addition, an important conclusion concerns the influence of elastomer bushing stiffness and damping behavior: With many computed parameter sets consisting of brake pressure, coefficient of friction and vehicle speed, it was possible to show strong impact of non-linear parameter-dependent stiffness. Significant changes in eigenfrequency and stability behavior were found with changing brake force in the respective variants. Moreover, the elastomer bushing's damping parameters were found to directly affect the stability of the computed modes: For values according to available component test data, all modes remained stable. Hence, most variants were computed for damping reduced by a factor 100.

Therefore, two statements can be deduced: Firstly, depending on bushing location, operational parameters and component characteristics, it can be necessary to implement the elastomer bushings' stiffness behavior in a non-linear manner for correct eigenfrequency and displacement results. Secondly, if stability is still considered in future analyses of creep groan oscillation content, elastomer bushing damping characteristics show a high influence and need to be modelled with care too. In general, it is recommended to refer on sophisticated static and dynamic component test data concerning these aspects.

Due to the small vehicle speeds during creep groan, the effects of convective and geometric stiffness terms as well as of gyroscopic terms were estimated very small in the system matrix analysis. Stability and eigenfrequency results have confirmed this assumption, almost no changes were found when omitting these terms. Moreover, computation time was reduced for approx. 16 % by this measure. By contrast, the size of the modal basis, defined by the frequency limit for calculation of real modes, was found to be of significant influence on the stability of the resulting modes. Therefore, it can be concluded that simulation time should rather be saved at the additional rotational terms instead of the modal basis.

In addition, Complex Eigenvalue Analysis could further be meaningful for creep groan in terms of a different evaluation mechanism. Due to creep groan's stick-slip excitation mechanism, relative tangential displacements within the contact could be investigated in order to deliver a statement about the possible excitation of a mode by stick-slip transitions.

Furthermore, it is noted that all three relevant eigenmodes showed mainly rigid body movements. Especially for transient analysis, which seems beneficial for a further approach concerning the simulative prediction of creep groan, this fact can be important: Very strong simplifications of some parts of the model can be acceptable and decrease the computational effort of e.g. an explicit dynamic time integration simulation.

According to these creep groan-relevant results, a reduction of occurrence and ampli-

---

tudes of this phenomenon based on changes of the suspension system seems difficult. Stiffness characteristics of the elastomer bushings have shown strong influence on creep-groan relevant modes and could therefore offer potential for optimization and tuning. However, conflicting interests with demands on driving dynamics such as safety, comfort or sportive driveability allow only minor changes of the bushing's stiffness characteristics.

Hence, a possible course of action is and will be a reduction of the excitation by the stick-slip effect combined with increased damping in points of high displacements during creep groan oscillation. This includes modifications and optimization of the frictional contact between brake disk and pad by changing material parameters and reducing the difference of static and dynamic coefficient of friction. Additionally, further energy dissipation should be introduced in the system at neuralgic points such as the elastomer bushings between lower and upper control arm or at the connection between chassis and spring with damper assembly. Again, stiffnesses can be modified only in a minor manner due to the already mentioned demands on vehicle dynamics.

**Regarding moan**, two relevant modes were found for two different rim designs, one at 562.5 – 563.4 Hz, one at 358.7 Hz. Both featured a characteristic torsional mode of the rim, which was also found in related experimental tests and publications. However, unstable parameter combinations were not found in a correct manner - one variant was over-estimated, one was under-estimated.

Mainly due to brake moan's tonal characteristic, Complex Eigenvalue Analysis should still be applicable in terms of stability prediction. Hence, further improvements of the model seem necessary: Especially more accurate damping parameters and a more sophisticated tire model are part of the recommendation.



## List of Figures

2.1	Functional groups of a vacuum-boosted, hydraulically activated passenger vehicle brake system . . . . .	5
2.2	Schematic sketches of basic brake caliper designs . . . . .	8
2.3	Schematic depiction of brake torque blending . . . . .	11
2.4	Measured dynamic stiffness and loss angle characteristics of a control arm's elastomer bushing in radial direction over frequency for different excitation amplitudes $ y $ . . . . .	14
2.5	Displacement-excited single mass oscillator . . . . .	15
2.6	Examples for passive and active elastokinematic effects . . . . .	16
2.7	Desired changes of toe angles for optimal behavior under lateral load	18
2.8	Desired changes of toe angles for optimal behavior under $\mu$ -split braking	19
2.9	Examples for conventional elastomer bushing design . . . . .	20
2.10	Measured dynamic stiffness and loss angle characteristics over frequency of a control arm's hydraulic elastomer bushing in radial, horizontal direction for an excitation amplitude of $ y  = 0.5$ mm . . . . .	21
2.11	Schematic diagram of a force-excited single mass oscillator . . . . .	23
2.12	Explanatory diagrams of performed simulations of a non-linear force-excited single mass oscillator . . . . .	24
2.13	Phase diagram of the Van der Pol oscillator for $\varepsilon = 0.6$ . . . . .	25
2.14	Characteristic plots of a Hopf bifurcation . . . . .	27
2.15	Classification of different disk brake NVH phenomena . . . . .	30
2.16	Characteristic frequency plot of pad acceleration in vehicle's x-direction during 63 Hz creep groan measured on a drum-driven suspension and brake test rig . . . . .	31
2.17	Characteristic frequency plot of pad acceleration in vehicle's x-direction during 386 Hz moan measured on a drum-driven suspension and brake test rig . . . . .	32
2.18	1D mass-on-belt model for physical instabilities . . . . .	34
2.19	2D mass-on-belt model for dynamic instabilities . . . . .	35
2.20	CEA for disk brake squeal: procedure and essential simplifications .	36
2.21	Influence of relative speed on the quality of friction force linearization	39
2.22	Influence of different damping models on real and imaginary part of nodal displacement amplitudes within one mode . . . . .	43
3.1	Adapted model for creep groan and moan CEA simulation with rim A	46
3.2	Adapted model for creep groan and moan CEA simulation with rim B	47

3.3	Applied boundary constraints for CEA simulation . . . . .	48
3.4	Measured static stiffness characteristics of a control arm's hydraulic elastomer bushing . . . . .	51
3.5	Elastomer bushing stiffnesses with significant non-linear behavior in the relevant simulative parameter range . . . . .	54
3.6	Bushing stiffness over brake pressure for parameter-dependent implemented bushings and a coefficient of friction $\mu = 0.4$ . . . . .	55
3.7	Phase relationships of forces on a force-excited single mass oscillator depicted as vectors in the complex plane . . . . .	57
3.8	Dynamic force-displacement behavior in the presence of hysteresis effects . . . . .	58
3.9	Modal mass and stiffness matrices for the full-scale model of variant 5 - Best-M. LD . . . . .	63
3.10	Modal speed-dependent and damping matrices for the full-scale model of variant 5 - Best-M. LD . . . . .	64
4.1	Normalized displacements of unstable mode #1 for variant 3 - Non-lin. Stiff. with parameters $\mu = 0.4$ and $p_B = 4$ bar, $p_B = 16$ bar . . . . .	68
4.2	Normalized displacements of unstable mode #2 for variant 3 - Non-lin. Stiff. with parameters $\mu = 0.4$ and $p_B = 16$ bar . . . . .	70
4.3	Normalized displacements of unstable mode #3 for variant 3 - Non-lin. Stiff. with parameters $\mu = 0.4$ and $p_B = 4$ bar, $p_B = 16$ bar . . . . .	71
4.4	Normalized displacements of unstable mode #4 for variant 3 - Non-lin. Stiff. with parameters $\mu = 0.4$ and $p_B = 4$ bar, $p_B = 16$ bar . . . . .	73
4.5	Normalized displacements of unstable mode #5 for variant 3 - Non-lin. Stiff. with parameters $\mu = 0.45$ and $p_B = 10$ bar . . . . .	74
4.6	Normalized displacements of unstable mode #6 for variant 7 - Best-M. Moan-A with parameters $\mu = 0.55$ and $p_B = 10$ bar . . . . .	75
4.7	Normalized displacements of relevant mode #7 for variant 8 - Best-M. Moan-B with parameters $\mu = 0.4$ and $p_B = 16$ bar . . . . .	75
4.8	Multi-dimensional stability diagram of unstable mode #1 for variant 1 - Squeal-M. . . . .	77
4.9	Multi-dimensional stability diagram of unstable mode #1 for variant 2 - Corr. Geom. . . . .	78
4.10	Multi-dimensional stability diagram of unstable mode #1 for variant 3 - Non-lin. Stiff. . . . .	79
4.11	Multi-dimensional stability diagram of unstable mode #1 for variant 8 - Best-M. Moan-B . . . . .	79
4.12	Multi-dimensional stability diagram of unstable mode #3 for variant 1 - Squeal-M. . . . .	80
4.13	Multi-dimensional stability diagram of unstable mode #3 for variant 2 - Corr. Geom. . . . .	81
4.14	Multi-dimensional stability diagram of unstable mode #3 for variant 3 - Non-lin. Stiff. . . . .	81

4.15	Multi-dimensional stability diagram of unstable mode #3 for variant 5 – Best-M. LD . . . . .	82
4.16	Multi-dimensional stability diagram of unstable mode #4 for variant 1 – Squeal-M. . . . .	83
4.17	Multi-dimensional stability diagram of unstable mode #4 for variant 2 – Corr. Geom. . . . .	83
4.18	Multi-dimensional stability diagram of unstable mode #4 for variant 3 – Non-lin. Stiff. . . . .	84
4.19	Multi-dimensional stability diagram of unstable mode #4 for variant 5 – Best-M. LD . . . . .	85
4.20	Multi-dimensional stability diagram of unstable mode #6 for variant 7 – Best-M. Moan-A . . . . .	86
4.21	Multi-dimensional stability diagram of relevant mode #7 for variant 8 – Best-M. Moan-B . . . . .	87
5.1	Drum-driven suspension and brake test rig of the Institute of Automotive Engineering - Graz University of Technology. . . . .	90
5.2	Position of the utilized acceleration sensor on the upper end of the inner brake pad’s backing plate . . . . .	90
5.3	Time signal and frequency plot of measured pad accelerations in vehicle’s x-direction during 18 Hz creep groan at $p_B = 10$ bar and $v_{veh} = 0.06$ km/h . . . . .	92
5.4	Time signal and frequency plot of measured pad accelerations in vehicle’s x-direction during 63 Hz creep groan at $p_B = 8$ bar and $v_{veh} = 0.08$ km/h . . . . .	93
5.5	Laser-vibrometry measurements of rim deflections during brake moan	95
5.6	Time signal and frequency plot of measured pad accelerations in vehicle’s x-direction during 386 Hz moan at $p_B = 13.15$ bar and $v_{veh} = 0.08$ km/h . . . . .	96



## List of Tables

2.1	Toe-angle tendency for increasing vertical load . . . . .	17
2.2	Toe-angle tendency for increasing lateral load . . . . .	18
2.3	Toe-angle tendency for different longitudinal loads . . . . .	18
2.4	Sources of non-linear behavior and examples . . . . .	22
2.5	Parameters and initial conditions for super- and subharmonic oscillation simulations of a force-excited single mass oscillator . . . . .	24
3.1	Low-frequency CEA model and parameter variant overview . . . . .	49
3.2	Parameters for CEA simulations . . . . .	50
3.3	Absolute stiffness values of elastomer bushings and the coil spring within variant 2 - Corr. Geom. in local element coordinates . . . . .	52
3.4	Relative stiffness of variant 2 - Corr. Geom. compared to variant 1 - Squeal-M. in local element coordinates . . . . .	52
3.5	Relative changing factor of elastomer bushing viscous damping values from variant 1 - Squeal-M. to variant 4 - Best-M. in local element coordinates . . . . .	60
3.6	Absolute viscous damping values of elastomer bushings and the suspension damper within variant 4 - Best-M. in local coordinates . . . . .	60
4.1	Unstable modes and other relevant modes found by CEA variant analysis and resulting eigenfrequency minima & maxima over all eight variants . . . . .	69
4.2	Eigenfrequency ranges of relevant and unstable modes . . . . .	76



---

## Bibliography

- [1] D. Adamski, *Simulation in der Fahrwerktechnik: Einführung in die Erstellung von Komponenten- und Gesamtfahrzeugmodellen*. Wiesbaden, Germany: Springer Vieweg, 2014. DOI: 10.1007/978-3-658-06536-2.
- [2] A. Akay, O. Giannini, F. Massi, and A. Sestieri, “Disc brake squeal characterization through simplified test rigs”, *Mech. Syst. Signal Process.*, vol. 23, no. 8, pp. 2590–2607, Nov. 2009. DOI: 10.1016/j.ymssp.2009.03.017.
- [3] R. Allgaier, “Experimentelle und Numerische Untersuchungen zum Bremsenquietschen”, in *Fortschrittberichte VDI: Reihe 12*, vol. 481, Düsseldorf, Germany: VDI, 2002.
- [4] K. Augsburg, P. Hauschild, and S. Gramstat, “Fundamental tests of low-frequency noise phenomena especially creep groan, with a simplified test setup”, in *Conf. Proc. EuroBrake 2016*, Milan, Italy: FISITA, Jun. 13–15, 2016.
- [5] A. N. Backstrom, “Voice of the OEM – Panel Discussion”, in *SAE Brake Colloq. & Exhibition 35th Annu.*, Orlando, FL, USA, Sep. 24–27, 2017.
- [6] J. Bauer, M. Körner, and A. Pfaff, “Moan noise – the phenomenon and solution approaches”, in *Conf. Proc. EuroBrake 2017*, Dresden, Germany: FISITA, May 2–4, 2017.
- [7] C. Bittner, “Reduzierung des Bremsrubbels bei Kraftfahrzeugen durch Optimierung der Fahrwerkslagerung”, PhD thesis, Dept. Mech. Eng., Technical University of Munich, Munich, Germany, Feb. 2006. [Online]. Available: <https://d-nb.info/985158654/34> (visited on 04/20/2018).
- [8] “Brake friction material”, in *Revised Code of Washington (RCW)*, ch. 70.285. [Online]. Available: <http://apps.leg.wa.gov/RCW/default.aspx?cite=70.285> (visited on 04/19/2018).
- [9] J. Brecht, W. Hoffrichter, and A. Dohle, “Mechanisms of brake creep groan”, in *Annu. Brake Colloq. Eng. Display*, USA: SAE International, Oct. 1997. DOI: 10.4271/973026.
- [10] B. Breuer and K. H. Bill, Eds., *Bremsenhandbuch: Grundlagen, Komponenten, Systeme, Fahrdynamik*, 5th ed. Wiesbaden, Germany: Springer Vieweg, 2017. DOI: 10.1007/978-3-658-15489-9.

- [11] J. Brunetti, F. Massi, W. D'Ambrogio, and Y. Berthier, "A new instability index for unstable mode selection in squeal prediction by complex eigenvalue analysis", *J. Sound Vibration*, vol. 377, pp. 106–122, Sep. 2016. DOI: 10.1016/j.jsv.2016.05.002.
- [12] J. Brunetti, F. Massi, A. Saulot, M. Renouf, and W. D'Ambrogio, "System dynamic instabilities induced by sliding contact: A numerical analysis with experimental validation", *Mech. Syst. Signal Process.*, vol. 58-59, pp. 70–86, 2015. DOI: 10.1016/j.ymsp.2015.01.006.
- [13] R. M. Cardillo, "Dynamic testing of elastomer mountings", *J. Appl. Polymer Sci.*, vol. 8, no. 1, pp. 53–71, 1964. DOI: 10.1002/app.1964.070080104.
- [14] S. Carvajal, D. Wallner, R. Helfrich, and M. Klein, "Excellent brake NVH comfort by simulation - use of optimization methods to reduce squeal noise", *SAE Tech. Papers*, Jun. 2016. DOI: 10.4271/2016-01-1779.
- [15] Y. Dai and T. C. Lim, "Suppression of brake squeal noise applying finite element brake and pad model enhanced by spectral-based assurance criteria", *Appl. Acoust.*, vol. 69, no. 3, pp. 196–214, Mar. 2008. DOI: 10.1016/j.apacoust.2006.09.010.
- [16] S. Divakaruni and H. T. Chang, "Friction back plate design/manufacturing/quality - key attributes for better brake performance", *SAE Tech. Papers*, Sep. 2017. DOI: 10.4271/2017-01-2506.
- [17] M. Donley and D. Riesland, "Brake groan simulation for a McPherson strut type suspension", *SAE Tech. Papers*, May 2003. DOI: 10.4271/2003-01-1627.
- [18] H. Dresig and F. Holzweißig, *Maschinendynamik*, 12th ed. Berlin/Heidelberg, Germany: Springer, 2016.
- [19] C. Elbers and T. Schrüllkamp, "Automatisierte Abbildung von Kinematik und Elastokinematik aus Prüfstandsversuchen zur Fahrdynamiksimulation", in *SIMPACK - User Meeting*, (Nov. 13–14, 2001). [Online]. Available: [http://www.simpack.com/fileadmin/simpack/doc/usermeeting01/um01-ika\\_schrue11.pdf](http://www.simpack.com/fileadmin/simpack/doc/usermeeting01/um01-ika_schrue11.pdf) (visited on 04/19/2018).
- [20] K. Ellermann, *Nichtlineare Schwingungen - Skriptum zur Vorlesung*. Lecture Notes. Inst. of Mech., Graz University of Technology, 2016.
- [21] C. K. Evans, "Voice of the OEM – Panel Discussion", in *SAE Brake Colloq. & Exhibition 35th Annu.*, Orlando, FL, USA, Sep. 24–27, 2017.
- [22] A. Fidlin, *Nonlinear Oscillations in Mechanical Engineering*. Berlin/Heidelberg, Germany: Springer, 2006. DOI: 10.1007/3-540-28116-9.
- [23] P. Fischer, "Stochastic dynamics of finite element systems - an approach from low to high frequencies including nonclassical damping effects", PhD thesis, Graz University of Technology, Graz, Austria, 1998.

- 
- [24] R. C. Frampton, *The dynamic testing of elastomers*. [Online]. Available: <http://www.alphatestingsystems.com/RFdynamic-testingPaperWEB.pdf> (visited on 04/20/2018).
- [25] N. Fransson, “Development of multi-body model to simulate creep groan in ADAMS”, Master’s thesis, Dept. Civil Environmental Eng., Chalmers University of Technology, Gothenburg, Sweden, 2016. [Online]. Available: <http://publications.lib.chalmers.se/records/fulltext/238613/238613.pdf> (visited on 04/19/2018).
- [26] R. Gasch, K. Knothe, and R. Liebich, *Strukturodynamik: Diskrete Systeme und Kontinua*, 2nd ed. Berlin/Heidelberg, Germany: Springer, 2012. DOI: 10.1007/978-3-540-88977-9.
- [27] F. Gauterin, J. Grochowicz, M. Haverkamp, H. Marschner, J. Pankau, and M. Rostek, “Bremsenknarzen: Phänomenologie und Abhilfe”, *ATZ - Automobiltechnische Zeitschrift*, vol. 106, no. 7-8, pp. 652–659, 2004. DOI: 10.1007/BF03221642.
- [28] N. Gräbner, “Analyse und Verbesserung der Simulationsmethode des Bremsenquietschens”, PhD thesis, Technische Universität Berlin, Berlin, Germany, Oct. 2016. DOI: 10.14279/depositonce-5577.
- [29] N. Gräbner, S. Quraishi, C. Schröder, V. Mehrmann, and U. von Wagner, “New numerical methods for the complex eigenvalue analysis of disk brake squeal”, in *Conf. Proc. EuroBrake 2014*, Lille, France: FISITA, May 13–15, 2014.
- [30] J. Guckenheimer and P. Holmes, “Nonlinear oscillations, dynamical systems, and bifurcations of vector fields”, in *Appl. Math. Sciences*, vol. 42, New York, NY, USA: Springer, 2002. DOI: 10.1007/978-1-4612-1140-2.
- [31] T. J. Hall, “Voice of the OEM – Panel Discussion”, in *SAE Brake Colloq. & Exhibition 35th Annu.*, Orlando, FL, USA, Sep. 24–27, 2017.
- [32] B. Heißing, M. Ersoy, and S. Gies, *Fahrwerkhandbuch : Grundlagen · Fahrdynamik · Komponenten · Systeme · Mechatronik · Perspektiven*, 4th ed. Wiesbaden, Germany: Springer Vieweg, 2013. DOI: 10.1007/978-3-658-01992-1.
- [33] H. Hetzler, D. Schwarzer, and W. Seemann, “Analytical investigation of steady-state stability and hopf-bifurcations occurring in sliding friction oscillators with application to low-frequency disc brake noise”, *Commun. Nonlinear Sci. Numerical Simulation*, vol. 12, no. 1, pp. 83–99, Feb. 2007. DOI: 10.1016/j.cnsns.2006.01.007.
- [34] H. Hetzler, “Zur Stabilität von Systemen bewegter Kontinua mit Reibkontakten am Beispiel des Bremsenquietschens”, PhD thesis, Inst. Eng. Mech. (ITM), Dept. Mech. Eng., Karlsruhe Institute of Technology (KIT), Karlsruhe, Germany, 2008. DOI: 10.5445/KSP/100007815.

- [35] W. Hirschberg and H. Waser, *Vorlesungsskriptum Kraftfahrzeugtechnik*. Lecture Notes. Inst. of Automotive Eng., Graz University of Technology, 2012.
- [36] E. J. Holdorf, “Voice of the OEM – Panel Discussion”, in *SAE Brake Colloq. & Exhibition 35th Annu.*, Orlando, FL, USA, Sep. 24–27, 2017.
- [37] M. J. A. Holmes, H. P. Evans, T. G. Hughes, and R. W. Snidle, “Transient elastohydrodynamic point contact analysis using a new coupled differential deflection method part 1: Theory and validation”, *Proc. of the IMechE, Part J: J. Eng. Tribology*, vol. 217, no. 4, pp. 289–304, 2003. DOI: 10.1243/135065003768618641.
- [38] S. Huemer-Kals, M. Pürscher, and P. Fischer, “Application limits of the complex eigenvalue analysis for low-frequency vibrations of disk brake systems”, *SAE Tech. Papers*, Sep. 2017. DOI: 10.4271/2017-01-2494.
- [39] T. Jung and S. Chung, “Research for brake creep groan noise with dynamometer”, *SAE Int. J. Passenger Cars - Mech. Syst.*, vol. 5, no. 4, pp. 1224–1229, Sep. 2012. DOI: 10.4271/2012-01-1824.
- [40] Y.-D. Kim, U.-C. Jeong, J.-S. Kim, T.-S. Park, S.-H. Lee, J.-M. Yoon, J.-J. Roh, and J.-E. Oh, “Identification of moan-noise generation mechanisms by an experimental method and verification of the mechanism by finite element analysis”, *Proc. of the IMechE, Part D: J. Automobile Eng.*, vol. 229, no. 10, pp. 1392–1405, Sep. 2015. DOI: 10.1177/0954407014562618.
- [41] N. M. Kinkaid, O. M. O’Reilly, and P. Papadopoulos, “Automotive disc brake squeal”, *J. Sound Vibration*, vol. 267, no. 1, pp. 105–166, Oct. 2003. DOI: 10.1016/S0022-460X(02)01573-0.
- [42] A. K. C. Kléperon, R. D. A. Abreu, R. M. Bitencourt, and F. J. M. Almeida, “Brake moan noise study through experimental and operational modal analysis techniques in a passenger car”, *SAE Tech. Papers*, Nov. 2014. DOI: 10.4271/2014-36-0768.
- [43] R. I. Leine and D. H. van Campen, “Bifurcation phenomena in non-smooth dynamical systems”, *Eur. J. Mech. - A/Solids*, vol. 25, no. 4, pp. 595–616, Jul. 2006. DOI: 10.1016/j.euromechsol.2006.04.004.
- [44] H. Marschner, P. Leibolt, A. Pfaff, and C. Morschel, “Investigation of the interaction mechanisms of friction excited stick-slip-vibrations for the example of brake groaning and analogue vibration phenomena”, in *Proc. XXXV. International  $\mu$  Symposium, Fortschrittberichte VDI: Reihe 12*, vol. 800, Bad Neuenahr, Germany: VDI, Oct. 28–29, 2016.
- [45] D. Müller, D. Wallner, S. Carvajal, and F. Gauterin, “Simulation der Frequenzantwort des Rad-Bremse Verbundes auf gemessene Anregungssignale”, in *Proc. SIMVEC 2016, VDI-Berichte*, vol. 2279, Düsseldorf: VDI, Nov. 22–23, 2016, 491–508.

- 
- [46] M. Müller, M. Heidrich, and U. Bernhard, “Die Auslegung von Motorlagerungssystemen Benchmarking, Simulation und Versuch”, *ATZ - Automobiltechnische Zeitschrift*, vol. 99, no. 2, pp. 92–99, 1997.
- [47] A. H. Nayfeh and D. T. Mook, *Nonlinear Oscillations*. New York, NY, USA: John Wiley & Sons, 1995. DOI: 10.1002/9783527617586.
- [48] B. Neitzel, “Keynote: Autonomous driving, zero emission powertrains & big data - how will this effect brake system architecture and brake component specification for future high performance cars”, in *SAE Brake Colloq. & Exhibition 35th Annu.*, Orlando, FL, USA, Sep. 24–27, 2017.
- [49] “PERMAS-Workshop - Dynamik II Erweiterungen und spezielle Anwendungen”, Lecture Notes. INTES GmbH, Stuttgart, Germany, Oct. 2015.
- [50] S. Pischinger and U. Seiffert, Eds., *Vieweg Handbuch Kraftfahrzeugtechnik*, 8th ed. Wiesbaden, Germany: Springer Vieweg, 2016. DOI: 10.1007/978-3-658-09528-4.
- [51] M. Pürscher and P. Fischer, “Strain gauge application at pad backing plates to investigate friction force and NVH issues”, in *Conf. Proc. EuroBrake 2017*, Dresden, Germany: FISITA, May 2–4, 2017.
- [52] M. Pürscher and P. Fischer, “Systematic experimental creep groan characterization using a suspension and brake test rig”, *SAE Tech. Papers*, Sep. 2017. DOI: 10.4271/2017-01-2488.
- [53] S. Quraishi, C. Schröder, and V. Mehrmann, “Solution of large scale parametric eigenvalue problems arising from brake squeal modeling”, *Proc. Appl. Math. Mech.*, vol. 14, no. 1, pp. 891–892, 2014. DOI: 10.1002/pamm.201410426.
- [54] K. S. Rosselot, “Copper released from brake lining wear in the san francisco bay area”, Jan. 2006. [Online]. Available: [http://www.scvurppp-w2k.com/cu\\_control\\_measures/Brake%20Pads/BPP%20Docs/BrakeSourcesReportFinal01-30-06.pdf](http://www.scvurppp-w2k.com/cu_control_measures/Brake%20Pads/BPP%20Docs/BrakeSourcesReportFinal01-30-06.pdf) (visited on 04/20/2018).
- [55] A. Sattlecker, “Simulation niederfrequenter Instabilitäten in einer Scheibenbremsanlage”, Master’s thesis, Inst. of Automotive Eng., Graz University of Technology, Graz, Austria, Oct. 2016.
- [56] A. Shivaswamy, R. Nunes, and M. Könnig, “A time domain approach towards analysing creep groan noise in automobile brakes”, in *Conf. Proc. EuroBrake 2016*, Milan, Italy: FISITA, Jun. 13–15, 2016.
- [57] J.-J. Sinou and L. Jézéquel, “Mode coupling instability in friction-induced vibrations and its dependency on system parameters including damping”, *Eur. J. Mech. - A/Solids*, vol. 26, no. 1, pp. 106–122, Jan. 2007. DOI: 10.1016/j.euromechsol.2006.03.002.
- [58] D. Wallner, “Experimental and numerical investigations on brake squeal”, PhD thesis, Inst. of Automotive Eng., Graz University of Technology, Graz, Austria, 2012.

- [59] A. Wang, L. Zhang, N. Jaber, and J. Rieker, “On brake moan mechanism from the modeling perspective”, *SAE Tech. Papers*, Mar. 2003. DOI: 10.4271/2003-01-0681.
- [60] K. W. Yoon, J. C. Lee, and S. S. Cho, “The study of vehicle structural characteristics for creep groan noise”, *SAE Tech. Papers*, Sep. 2011. DOI: 10.4271/2011-01-2363.